

DESIGN, SIMULATION AND PERFORMANCE STUDY OF MEMS TECHNOLOGY BASED PRESSURE SENSORS

By
VINOD BELWANSHI
ENGG 01201304001

Bhabha Atomic Research Centre, Mumbai

A thesis submitted to the

Board of Studies in Engineering Sciences

In partial fulfillment of requirements

for the Degree of

DOCTOR OF PHILOSOPHY

of

HOMI BHABHA NATIONAL INSTITUTE

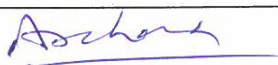
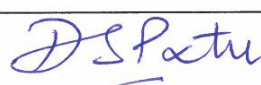
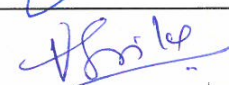
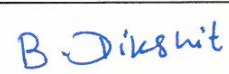
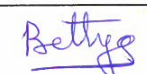


July, 2019

Homi Bhabha National Institute

Recommendations of the Viva Voce Committee

As members of the Viva Voce Committee, we certify that we have read the dissertation prepared by Mr. Vinod Belwanshi entitled “Design, simulation and performance study of MEMS technology based pressure sensors” and recommend that it may be accepted as fulfilling the thesis requirement for the award of Degree of Doctor of Philosophy.

Chairman – Dr. Archana Sharma		Date: 17/07/19
Guide / Convener – Dr. Anita Topkar		Date: 17/07/2019
Co-guide - Dr. D. S. Patil		Date: 17-07-2019
Examiner – Prof. Prasanna Gandhi		Date: 17/07/19
Member 1- Dr. Gopika Vinod		Date: 17/7/2019
Member 2- Dr. V. H. Patankar		Date: 17.07.2019
Member 3- Dr. B. Dikshit		Date: 17/7/19
Invitee – Dr. C.A. Betty		Date: 17/07/2019

Final approval and acceptance of this thesis is contingent upon the candidate's submission of the final copies of the thesis to HBNI.

We hereby certify that we have read this thesis prepared under our direction and recommend that it may be accepted as fulfilling the thesis requirement.

Date:
Place:

Guide

17/07/2019
Dr. Anita Topkar

Co-guide

17-07-2019
Dr. D. S. Patil

STATEMENT BY AUTHOR

This dissertation has been submitted in partial fulfilment of requirements for an advanced degree at Homi Bhabha National Institute (HBNI) and is deposited in the Library to be made available to borrowers under rules of the HBNI.

Brief quotations from this dissertation are allowable without special permission, provided that accurate acknowledgement of source is made. Requests for permission for extended quotation from or reproduction of this manuscript in whole or in part may be granted by the Competent Authority of HBNI when in his or her judgment the proposed use of the material is in the interests of scholarship. In all other instances, however, permission must be obtained from the author.

Date:

Vinod Belwanshi

DECLARATION

I, hereby declare that the investigation presented in the thesis has been carried out by me. The work is original and has not been submitted earlier as a whole or in part for a degree/diploma at this or any other Institution/University.

Date:

Vinod Belwanshi

LIST OF PUBLICATIONS ARISING FROM THE THESIS

Journals

(a) Published

1. Vinod Belwanshi, Sebin Philip and Anita Topkar “Gamma radiation induced effects on the performance of piezoresistive pressure sensors fabricated using different technologies”, IEEE Transaction on Nuclear Science (Accepted).
2. Vinod Belwanshi and Anita Topkar “Quantitative analysis of response of MEMS piezoresistive pressure sensors based on high bandgap materials”, IETE Journal of Research, 2019, Taylor & Francis, DOI: 10.1080/03772063.2019.1620641
3. Vinod Belwanshi, Sebin Philip and Anita Topkar “Experimental study of gamma radiation induced degradation of a piezoresistive pressure sensor”, Microsystem Technologies, Vol. 24, No 8, pp 3299–3305, 2018, Springer, DOI: 10.1007/s00542-018-3806-5.
4. Vinod Belwanshi and Anita Topkar “Quantitative analysis of temperature effect on SOI piezoresistive pressure sensors”, Microsystem Technologies Vol. 23, No. 7, pp. 2719-2725, 2017, Springer, DOI:10.1007/s00542-016-3102-1.

Conferences

(a) Conference proceeding

1. Vinod Belwanshi and Anita Topkar "Design optimization and simulation of a diamond based piezoresistive pressure sensor for high temperature application" Materials Today: Proceedings, Elsevier (In press).
2. Vinod Belwanshi and Anita Topkar “Optimization of design parameters for bulk micromachined silicon membranes for piezoresistive pressure sensing application”, DAE Solid State Physics Symposium 2015; AIP Conference Proceedings 1731, 080004, 2016, DOI:10.1063/1.4947882

(b) Conferences presentations

1. Vinod Belwanshi and Anita Topkar, “Comparative study of piezoresistive pressure sensor based on silicon and wide band gap materials: a quantitative analysis”, presented at The 13th Annual IEEE International Conference on Nano/Micro

- Engineered and Molecular Systems (IEEE-NEMS) 2018, at NUS and Grand Hyatt, Singapore, April 22-26, 2018.
2. Vinod Belwanshi and Anita Topkar, “Design optimization and simulation of a diamond based piezoresistive pressure sensor for high temperature application”, presented at International Conference on Nanotechnology: Ideas, Innovations & Initiatives (ICN:3I)-2017, IIT Roorkee, India, December 06-08, 2017.
 3. Vinod Belwanshi and Anita Topkar. "Optimization of design parameters for bulk micromachined silicon membranes for piezoresistive pressure sensing application". presented at 60th DAE Solid State Physics Symposium 2015, Amity University, Noida, Uttar Pradesh, India, December 21–25 2015,
 4. Vinod Belwanshi and Anita Topkar, “Design and simulation study of piezoresistive pressure sensors for nuclear reactor application”, presented at 2nd International Symposium on Physics and Technology of Sensors: ISPTS-2, Pune, Maharashtra, India, March 08-10, 2015.
 5. Vinod Belwanshi and Anita Topkar, “Design optimization of piezoresistive pressure sensors for nuclear reactor applications”, presented at International Conference on MEMS and Sensors 2014: ICMEMS-2014, IIT, Madras, Chennai, India, December 18-20, 2014.

Dedicated to my family

ACKNOWLEDGEMENT

First and foremost, I would like to express my profound gratitude to my main supervisor Dr. Anita Topkar for her valuable guidance, support and constant encouragement throughout my doctoral research work. She has provided me all the freedom to carry out my research work while ensuring that I do not deviate from the primary objectives. This thesis would not have been possible without her able guidance and constant motivation. I would like to express my sincere thanks to my co-supervisor Prof. D. S. Patil (Indian Institute of Technology Bombay, Mumbai, India) for his support and guidance during the research work.

I greatly acknowledge the contributions of my doctoral committee members Dr. Archana Sharma (Chairman), Dr. V. H. Patankar, Dr. Gopika Vinod and Dr. B. Dikshit for their valuable time for periodical critical evaluation of my research work. I am grateful to Dr. D. K. Maity (Associate Dean HBNI) for his support during the initial phase of doctoral work. I would also like to thank Dean HBNI, Academic Dean HBNI, Board of Studies (Engineering Sciences, HBNI) and administrative staff members for their constant support during my PhD.

I would like to thank Department of Atomic Energy (DAE), India for providing me the financial support in the form of a highly prestigious award of DAE Graduate Fellowship Scheme (DGFS) to pursue my PhD. I would like to thank Bhabha Atomic Research Centre (BARC), Mumbai for allowing me to use necessary resources required in my research work.

I express my gratitude to Dr. Arvind Singh, Amit Kumar, Mr. Somyajit Chakravarti, Mr. Sebin Philip, Mr. Arvind Kumar, Ms. Bharti, Dr. (Mrs.). K.G. Girija for their help during conducting experiments. I would like to express my sincere thanks to Dr. Jamil Akhtar, Mr. Devesh Barshilia, Md. Sakeel Ahmed, Mr. Sanjeev Kumar and Dr. Vibhor Kumar in CSIR-CEERI, Pilani, Rajasthan for their support in fabrication of the pressure sensor.

I am thankful to my friends Mr. Anuj Sharma, Mr. Ashish Shelke, Dr. Somenath Chatterjee, Dr. Ravi Dhawan, Dr. Vineet Vajpayee and Ms. Sonika Chauhan for the fruitful discussions and cheerful memories. A special thanks goes to my friends Dr.

Shankararao Chappa, Mr. Rahul Kumar, Mr. Abhishek Kaushik, Dr. Tribeni Roy for supporting me during thesis writing. I am also thankful to my roommates Dr. Vinay Rastogi, Mr. Suryakant Gautam, Dr. Nitendra Singh, Dr. Sunil Kumar and Dr. Naveen Kumar N for cheerful memories. A special thanks to my friends during M. Tech at Indian Institute of Technology, Kharagpur, WB, India- Wing Commander Mr. Vishnu Bajpai, Dr. Punit Rathore, Dr. Rangadhar Pradhan, Dr. Pijus Kundu, Mr. Srutarshi Banerjee, Mr. Vinod Kumar, Mr. Rahul Mishra, Mr. Abhishek Verma, Mr. Ramesh Rajan and Mr. G. Sai Nikhil for their support and encouragement. A special thanks to my childhood friends Mr. Ankur Jain, Mr. Kamal Bunkar, Mr. Sanjay Deharia and Mr. Varun Nagwanshi for their motivation and encouragement to pursue higher studies.

Last, but not the least, my family. Words would be few to describe my gratitude towards my family members my beloved parents Mrs. Sita & Mr. Amalsingh Belwanshi and my loving wife Dr. (Mrs.) Archana Mahaptara for their endless patience, support unconditional love, and encouragement. Whosoever I am today, it is only because of them. I would like to express my gratitude to parent-in-laws Late Mr. Hari Shankar Mahapatra and Mrs. Sujata Panda for their love and support. I would like to express my gratitude to sister & brother-in-law Mrs. Veena & Mr. Sateesh Chandrapuri, nephew Mr. Samarth, younger brother Mr. Manoj Belwanshi, for their support and motivation.

Above all, I bow down before the Almighty who has enabled me to complete the work successfully and made everything possible.

Vinod Belwanshi.

LIST OF CONTENTS

Statement by author	v
Declaration	vii
List of publications arising from the thesis	ix
Acknowledgement	xiii
List of contents	xv
List of figures	xix
List of tables	xxv
List of symbols and abbreviations	xxvii
Synopsis	xxix
Chapter 1. Introduction	1
1.1 Objective of the research work	2
1.2 Organisation of the thesis	2
Chapter 2. Literature survey	5
2.1 Introduction	5
2.2 Status of commercial MEMS devices	5
2.3 Advancement in micromachining and MEMS technology	6
2.4 MEMS manufacturing techniques	8
2.4.1 Conventional IC technology processes and materials	8
2.4.2 Additional processes and materials used in MEMS	9
2.5 Classification of MEMS fabrication and etching processes	9
2.5.1 Bulk micromachining	10
2.5.2 Surface micromachining	11
2.5.3 High aspect ratio micromachining	12
2.5.4 Substrate bonding	14
2.6 Advantages of silicon for MEMS fabrication	14
2.7 Fabrication processes for MEMS	15
2.8 MEMS piezoresistive pressure sensor: Introduction	16
2.9 Classification of pressure sensors	18
2.9.1 Classification based on transduction techniques	18
2.9.2 Classification of pressure sensors based on pressure measurement method	22
2.10 Reliability and use of MEMS in a harsh environment	24
2.10.1 Radiation-induced effects in MEMS	24

2.10.2	Radiation-induced degradation of silicon	26
2.10.3	Radiation-induced degradation in piezoresistive sensors	27
2.10.4	MEMS piezoresistive pressure sensors for high temperatures	28
2.13	Summary	29
Chapter 3.	Design and simulation study of piezoresistive pressure sensors	31
3.1	Introduction	31
3.2	Analytical modelling of pressure sensors	31
3.2.1	A simplified equation for maximum deflection and induced stress	31
3.2.2	Simplified equations for the change in resistance of piezoresistors	32
3.2.3	Effect of temperature on the change of piezoresistor resistance	33
3.2.4	Calculation of the sensitivity of a pressure sensor	34
3.2.5	Nonlinearity calculation	34
3.3	Methodology and material properties	35
3.3.1	Steps to build a 3D model	36
3.3.2	Effect of diaphragm shape on the mechanical response	37
3.3.3	Effect of diaphragm geometry on mechanical response	39
3.3.4	Identification of the location of piezoresistors for maximum sensitivity	44
3.3.5	Analysis of pressure sensor response and nonlinearity	45
3.3.6	Quantitative analysis of temperature dependence of pressure sensor response	47
3.4	Selection of design parameters for the piezoresistive pressure sensors	49
3.4.1	Selected parameters for diffused/ion implanted piezoresistor based pressure sensors	49
3.4.2	Selected parameters for SOI wafer based pressure sensors	50
3.5	Comparative study of pressure sensor based on wide bandgap materials	51
3.5.1	Use of silicon as a material for MEMS	51
3.5.2	Use of wide bandgap material as alternative piezoresistive materials	52
3.5.3	Materials and methodology used for simulation study	55
3.6	Results and discussion	57
3.6.1	Silicon diaphragm and piezoresistors of different materials	57
3.6.2	Diaphragm and piezoresistors of the same material	60
3.6.3	Improving sensitivity of diamond based pressure sensors	62
3.6.4	Nonlinearity of pressure sensor response	63
3.7	Summary	65
Chapter 4.	Mask design, fabrication of pressure sensors and design & development of a signal conditioning circuit	67

4.1	Introduction	67
4.2	Mask design of diffused and SOI technology based pressure sensors	67
4.3	Fabrication process development for piezoresistive pressure sensors	70
4.3.1	Fabrication process for diffused piezoresistor based pressure sensor	70
4.3.2	Fabrication process for SOI based pressure sensor	72
4.4	Details of pressure sensor package	74
4.5	Signal conditioning circuit	75
4.5.1	Analysis and modelling of Wheatstone bridge for offset voltage compensation	75
4.5.2	Design and testing of signal conditioning circuit	79
4.6	Summary	81
Chapter 5.	Performance investigation of piezoresistive pressure sensors	83
5.1	Introduction	83
5.2	Characterisation setup	83
5.3	Performance study of pressure sensors fabricated during process development	85
5.3.1	Pressure response with Offset	85
5.3.2	Sensitivity	86
5.3.3	Offset voltage	87
5.3.4	Offset voltage drift	88
5.3.5	Linearity	88
5.3.6	Hysteresis	89
5.3.7	Resistance vs temperature	89
5.4	Diffused and SOI technology based pressure sensor (production batch)	90
5.5	Comparesion of simulation and Experimental	90
5.6	Summary	92
Chapter 6.	Experimental investigation of gamma radiation-induced degradation of piezoresistive pressure sensors	93
6.1	Introduction	93
6.2	Schematic diagrams of packaged pressure sensors	94
6.3	Results and Discussion	95
6.3.1	Case I: Commercial packaged pressure sensor with silicone oil	95
6.3.2	Case II: Commercial pressure sensor without silicone oil	99
6.3.3	Case III: Irradiation of in-house designed and developed pressure sensors	

6.3.3	Case IV: Irradiation study of piezoresistors under ^{60}Co exposure	106
6.4	Summary	106
Chapter 7.	Conclusions	109
7.1	Summary of research work	109
7.2	Highlights of the research work	111
7.3	Future scope	112
Appendix A.	Mathematical modelling of pressure sensors	115
Appendix B.	Piezoresistive effect: an introduction	131
Appendix C.	Analysis of Wheatstone bridge configurations for piezoresistive pressure sensors	145
References		149

LIST OF FIGURES

Figure No.	Details	Page No.
Figure 2.1:	Bulk micromachining, (a) Anisotropic wet etching, (b) Deep reactive etching.	10
Figure 2.2:	Types of etching, (a) Anisotropic etching, (b) Isotropic etching.	11
Figure 2.3:	Illustration of the surface micromachining process.	12
Figure 2.4:	Schematic of the LIGA process [22].	13
Figure 2.5:	Schematic explanation of deposition, lithography and etching process with positive photoresist and negative photoresist [6].	16
Figure 2.6:	Photographs of the piezoresistive pressure sensor, (a) Top view of chip, (b) Chip mounted on TO header, (c) Wire connected with TO header, (d) Packaged pressure sensor with electrical connection [34].	17
Figure 2.7:	Schematic of pressure sensor with exploded view [34].	17
Figure 2.8:	Various types of commercial packaging of pressure sensor: (a) Sensor housing a single monolithic silicon pressure sensor die by Motorola MPX 2010 DP, (b) Miniature surface mount technology with DIP housings allow for PCB-mounting by FirstSensor, (c) (DIP for assembly on PCB by AMSYS, (d) Pressure sensor by Honeywell Inc. for heavy duty applications.	18
Figure 2.9:	(a) First diffused piezoresistive pressure sensor: silicon wafer bonded with glass/metal, (b) Diffused piezoresistive pressure sensor using DRIE etching, (c) Diffused piezoresistive pressure sensor by anisotropic wet etching.	20
Figure 2.10:	Schematic of a basic capacitive pressure sensor.	20
Figure 2.11:	Schematic representation of an absolute pressure sensor.	22
Figure 2.12:	Schematic representation of a gauge pressure sensor.	23
Figure 2.13:	Schematic representation of a differential pressure sensor.	23
Figure 2.14:	Symbols for the pressure transducer.	23
Figure 3.1:	Simulation to build solid model (a) material property selection, (b) Process definition, (c) 2D layout, ((d) Fixed boundary condition (e) 3D solid model, and (f) 3D meshed model.	37
Figure 3.2:	Simulations for i) Model of plate (a) solid model, (b) mesh model, ii) DRIE etched diaphragm (c) Solid model, (d) Mesh model, iii) Anisotropically etched diaphragm (e) Solid model (f) Mesh model;diaphragm size $2000\ \mu\text{m} \times 2000\ \mu\text{m} \times 150\ \mu\text{m}$. The yellow color regions are depicted as fixed boundary conditions.	38
Figure 3.3:	Mechanical response of diaphragms of different types as a function of applied pressure; (a) Deflection (b) von Mises stress, diaphragm size $2000\ \mu\text{m} \times 2000\ \mu\text{m} \times 150\ \mu\text{m}$.	39
Figure 3.4:	Contour plots for the diaphragm of size $1000\ \mu\text{m} \times 1000\ \mu\text{m} \times 200\ \mu\text{m}$ for applied pressure 40 MPa; (a) Deflection, (b) von Mises stress.	40
Figure 3.5:	Contour plots for the diaphragm of size $1000\ \mu\text{m} \times 1000\ \mu\text{m} \times 200\ \mu\text{m}$ for the applied pressure of 40 MPa; (a) Stress XX, and (b) Stress YY.	40
Figure 3.6:	(a) Maximum deflection vs thickness of diaphragm for varying edge lengths of the diaphragm under applied pressure 40 MPa, (b) Validation of deflection variation for diaphragm size of $1000\ \mu\text{m} \times 1000\ \mu\text{m}$, under applied pressure 40 MPa.	41
Figure 3.7:	(a) Maximum von Mises stress vs thickness of diaphragm for varying edge lengths of the diaphragm under applied pressure 40 MPa, (b)	41

	Validation of von Mises stress for diaphragm size of $1000\ \mu\text{m} \times 1000\ \mu\text{m}$, under applied pressure 40 MPa.	
Figure 3.8:	(a) Deflection vs applied pressure for varying diaphragm size and for a diaphragm of thickness of $150\ \mu\text{m}$, (b) von Mises stress vs applied pressure for varying diaphragm size and for a diaphragm thickness $150\ \mu\text{m}$.	42
Figure 3.9:	(a) Deflection profile, and (b) von Mises stress for diaphragm size of $1000\ \mu\text{m} \times 1000\ \mu\text{m}$ for different diaphragm thicknesses; applied pressure is 40 MPa.	43
Figure 3.10:	(a) Stress XX Profile, and (b) Stress YY profile along the centre of the diaphragm for diaphragm size of $1000\ \mu\text{m} \times 1000\ \mu\text{m}$ with different diaphragm thicknesses; applied pressure is 40 MPa.	44
Figure 3.11:	Resultant stress profile along the centre of the diaphragm for diaphragm size of $1000\ \mu\text{m} \times 1000\ \mu\text{m}$ with different diaphragm thicknesses; applied pressure is 40 MPa.	44
Figure 3.12:	Identifying the location of the maximum change in the resistance for the diaphragm size $1000\ \mu\text{m} \times 1000\ \mu\text{m} \times 150\ \mu\text{m}$.	45
Figure 3.13:	Placement of the piezoresistors on the top of the diaphragm.	45
Figure 3.14:	(a) Output voltage of the Wheatstone bridge for different diaphragm thicknesses, diaphragm size $1000\ \mu\text{m} \times 1000\ \mu\text{m}$, (b) Sensitivity vs thickness of diaphragm for pressure sensor (diaphragm: $1000\ \mu\text{m} \times 1000\ \mu\text{m} \times 200\ \mu\text{m}$, Piezoresistor concentration $1 \times 10^{19}\ \text{cm}^{-3}$).	46
Figure 3.15:	The % nonlinearity of pressure sensor using diaphragm size $1000\ \mu\text{m} \times 1000\ \mu\text{m}$ with varying thickness.	46
Figure 3.16:	(a) Voltage output of pressure sensor for various concentration of piezoresistors, diaphragm size $1000\ \mu\text{m} \times 1000\ \mu\text{m} \times 200\ \mu\text{m}$, (b) Sensitivity as a function of doping concentration.	47
Figure 3.17:	(a) The voltage output of pressure sensor with varying temperatures for diaphragm size of $1000\ \mu\text{m} \times 1000\ \mu\text{m} \times 200\ \mu\text{m}$, piezoresistor doping $1 \times 10^{19}\ \text{cm}^{-3}$, (b) Sensitivity of pressure sensor at different temperatures, diaphragm size $1000\ \mu\text{m} \times 1000\ \mu\text{m} \times 200\ \mu\text{m}$, piezoresistor doping $1 \times 10^{19}\ \text{cm}^{-3}$.	48
Figure 3.18:	Voltage output of the pressure sensor at 40 MPa pressure for different temperatures and diaphragm thicknesses, diaphragm size $1000\ \mu\text{m} \times 1000\ \mu\text{m}$, piezoresistor doping $1 \times 10^{19}\ \text{cm}^{-3}$.	49
Figure 3.19:	Location of the piezoresistors on top of the square diaphragm.	50
Figure 3.20:	The magnitude of longitudinal gauge factor of single crystal silicon (p-type), 6H-SiC and 2 C-SiC at room temperature under varying dopant concentration [72], [101]–[103].	54
Figure 3.21:	Piezoresistive coefficients as a function of resistivity and grains size (i.e. large $=0.8\ \mu\text{m}$ and small $=0.3\ \mu\text{m}$) at room temperature [104].	54
Figure 3.22:	The contour plots for a silicon diaphragm of geometry $500\ \mu\text{m} \times 500\ \mu\text{m} \times 25\ \mu\text{m}$ at an applied pressure of 10 MPa, (a) Deflection, (b) von-Mises stress, (c) Directional stress XX, (d) Directional stress YY.	58
Figure 3.23:	The output voltages of piezoresistive pressure sensors incorporating silicon diaphragms and Si, Poly-Si, SiC or diamond as piezoresistor materials, diaphragm geometry $500\ \mu\text{m} \times 500\ \mu\text{m} \times 25\ \mu\text{m}$.	59
Figure 3.24:	Deflection magnitudes along a line through the centre of the diaphragm for diaphragms of various materials, diaphragm geometry $500\ \mu\text{m} \times 500\ \mu\text{m} \times 25\ \mu\text{m}$, applied pressure -10 MPa.	60
Figure 3.25:	von-Mises stress magnitudes along a line through centre of the	60

	diaphragm for diaphragms of various materials, diaphragm geometry - $500\ \mu\text{m} \times 500\ \mu\text{m} \times 25\ \mu\text{m}$, applied pressure -10 MPa.	
Figure 3.26:	The directional stress XX along a line through the centre of the diaphragm for various diaphragms materials, diaphragm geometry - $500\ \mu\text{m} \times 500\ \mu\text{m} \times 25\ \mu\text{m}$, applied pressure -10 MPa.	61
Figure 3.27:	The directional stress YY along a line through centre of the diaphragm for diaphragms of various materials, diaphragm geometry - $500\ \mu\text{m} \times 500\ \mu\text{m} \times 25\ \mu\text{m}$, pressure -10 MPa.	61
Figure 3.28:	The maximum deflection vs applied pressure for various diaphragm materials, diaphragm geometry - $500\ \mu\text{m} \times 500\ \mu\text{m} \times 25\ \mu\text{m}$.	61
Figure 3.29:	von-Mises stress vs applied pressure for various diaphragm materials, diaphragm geometry - $500\ \mu\text{m} \times 500\ \mu\text{m} \times 25\ \mu\text{m}$.	61
Figure 3.30:	The output voltage of the pressure sensor based on Si, SiC and diamond, diaphragm geometry - $500\ \mu\text{m} \times 500\ \mu\text{m} \times 25\ \mu\text{m}$.	63
Figure 3.31:	Sensitivity of diamond based pressure sensors with two different configurations for locating the piezoresistors.	63
Figure 3.32:	The % nonlinearity of pressure sensors incorporating diaphragm as well as piezoresistors of Si, SiC and diamond, diaphragm geometry - $500\ \mu\text{m} \times 500\ \mu\text{m} \times 25\ \mu\text{m}$.	64
Figure 4.1:	Schematic for cross-section view of (a) Diffused piezoresistors and (b) SOI based pressure sensor	67
Figure 4.2:	Photographs of the mask layout for diffused piezoresistor and SOI technology based piezoresistive pressure sensors: (a) Chip layout for the diffused piezoresistor sensor, (b) Chip layout for SOI based pressure sensor, (c) Diffused piezoresistor sensor layout for 8×8 array, (d) SOI technology based pressure sensor layout for 8×8 array.	69
Figure 4.3:	Schematic of fabrication process flow of boron diffused piezoresistor based piezoresistive pressure sensor.	71
Figure 4.4:	Diffused piezoresistor based sensors; (a) Bottom view of fabricated waferside, (b) Top view of fabricated wafer, (c) Pressure sensor chip top side, (d) Bottom view of pressure sensor chip, (e) Sensor chip attached on a TO-12 header and wire bonded, (f) Packaged pressure sensor chip in a stainless steel housing.	72
Figure 4.5:	Schematic of fabrication process flow for SOI technology based piezoresistive pressure sensor	73
Figure 4.6:	(a) Fabricated SOI wafer, (b) Glass bonded wafer, (c) Top view of sensor chip, (d) Magnified view of piezoresistor (e) pressure sensor chip attached with TO-12 header.	74
Figure 4.7:	(a) Parts used for packaging of the pressure sensor, (b) Exploded view of pressure sensor package.	75
Figure 4.8:	Wheatstone bridge configuration.	76
Figure 4.9:	Compensation techniques; (a) parallel (b) series (c) parallel-series.	77
Figure 4.10:	Schematic of the signal conditioning circuit for obtaining 4 to 20 mA current loop response.	79
Figure 4.11:	PCB design layout files (a, b, c, d), Fabricated PCB top (e), and Assembled PCB with components (f).	80
Figure 4.12:	(a) Voltage response of pressure sensors for uncompensated and compensated conditions, (b) The 4-20 mA current response for uncompensated and compensated conditions.	81
Figure 5.1:	(a) Schematic of the pressure sensor characterisation setup, (b) Photograph of experimental setup.	84
Figure 5.2:	Pressure response under the elevated temperatures for (a) Passivated and	85

	diffused (SLNO2) and (b) SOI technology based (SLNO5) based pressure sensor with 150 μm diaphragm thickness and 100 bar pressure range.	
Figure 5.3:	Sensitivity and % degradation of sensitivity for pressure sensors (a) Diffused resistor based, and (b) SOI technology based.	86
Figure 5.4:	Calculated sensitivity (slope fitting) under elevated temperatures from the linear curve for (a) Diffused resistor based and (b) SOI technology based sensor respectively.	86
Figure 5.5:	Variation in the offset voltage under elevated temperatures for (a) Diffused resistor, and (b) SOI technology based pressure sensor.	87
Figure 5.6:	Variation in offset voltage under elevated temperatures for (a) Diffused resistor, and (b) SOI technology based pressure sensors using a linear curve fitting.	87
Figure 5.7:	Offset voltage drift at room temperatures for 900 seconds for (a) Diffused resistor based, and (b) SOI technology based pressure sensor.	88
Figure 5.8:	Variation in linearity under the elevated temperatures for (a) Diffused, and (b) SOI technology based pressure sensors.	88
Figure 5.9:	Variation of hysteresis under elevated temperatures for (a) Diffused resistor based and (b) SOI technology based pressure sensors.	89
Figure 5.10:	Resistance of piezoresistors vs temperature for (a) Diffused piezoresistor, and (b) SOI technology based pressure sensors.	89
Figure 5.11:	(a) Diffused resistor pressure sensor response under elevated temperature up to 100 $^{\circ}\text{C}$ (b) SOI technology based pressure sensor response under elevated temperature up to 200 $^{\circ}\text{C}$.	90
Figure 5.12:	(a) Sensitivity and (b) offset voltage under varying temperature for diffused and SOI technology based pressure sensors.	90
Figure 5.13:	(a) Estimated and calculated sensitivity of piezoresistive pressure sensor (b) The % change in sensitivity of simulated and experimental.	91
Figure 6.1:	Schematic diagram of the pressure sensor; (a) Cross section of the sensor chip, (b) Top view showing piezoresistors over the diaphragm, (c) Packaged sensor-Case I and (d) Packaged sensor-Case II.	94
Figure 6.2:	Forward sweep measurements showing the pressure sensor performance with total gamma dose.	96
Figure 6.3:	Backward sweep measurements showing pressure response with total gamma dose.	96
Figure 6.4:	The output voltage response at 50 bar and the percentage change in the output voltage of the piezoresistive pressure sensor due to total gamma dose.	97
Figure 6.5:	Changes in the sensitivity of the piezoresistive pressure sensor (in $\text{mV}/\text{V}/\text{bar}$) with total gamma dose.	97
Figure 6.6:	Offset voltage variation as a function of total gamma dose.	98
Figure 6.7:	The hysteresis observed in the pressure response due to total gamma dose.	98
Figure 6.8:	The variation of Wheatstone bridge resistances with total gamma dose.	99
Figure 6.9:	Output voltage vs applied pressure with varying irradiation dose.	100
Figure 6.10:	Change in offset voltage as a function of accumulated gamma dose.	100
Figure 6.11:	Output voltage vs applied pressure with varying irradiation dose without offset.	100
Figure 6.12:	Sensitivity vs accumulated dose for commercial pressure sensor.	100
Figure 6.13:	Measured IV characteristics of piezoresistors at different total doses.	101
Figure 6.14:	Change in the resistance with increasing cumulative dose of the ^{60}Co	101

	radiation.	
Figure 6.15:	Pressure response of all types of pressure sensors measured at room temperature up to 100 bar.	102
Figure 6.16	Response of diffused piezoresistor based pressure sensor after various gamma dose exposures. The data points for total dose irradiation of 22.56 Mrad(Si) and 30.56 Mrad(Si) (indicated as 'half bridge output') were obtained by measuring the half bridge output. The half bridge output data was doubled for comparison with output voltage data for irradiation up to the total dose of 11.74 Mrad(Si) (b) Sensitivity and offset voltage variation for diffused piezoresistor based pressure sensor after various gamma dose exposures..	103
Figure 6.17:	(a) Response of SOI wafer based pressure sensor after various gamma dose exposures. The plots indicate observable changes in sensitivity and offset voltage due to gamma irradiation (b) Sensitivity and offset voltage variation of the SOI wafer based piezoresistive pressure sensor after various gamma dose exposures. The plots indicate that degradation of sensor is rapid after total dose exposure of 10 Mrad(Si).	104
Figure 6.18	Response of the polysilicon piezoresistor based pressure sensor after various gamma dose exposures. All data points for total dose irradiation up to 30.56 Mrad(Si) overlap indicating a negligible change in the sensor response (b) Sensitivity and offset voltage variation for the polysilicon piezoresistor based pressure sensor after various gamma dose exposures. The plots indicate that there is negligible change in the sensitivity and a small change in the offset voltage.	105
Figure 6.19	(a) Comparison of the variation in the sensitivity of pressure sensors as a function of gamma dose exposure (b) Comparison of the offset voltage variation of pressure sensors as a function of gamma dose exposure (c) Comparison of the hysteresis variation of pressure sensors as a function of gamma dose exposure.	106
Figure 6.20:	Resistance variation with irradiation dose for Die 1.	106
Figure 6.21:	Resistance variation with irradiation dose for Die 2.	106
Figure A.1:	Pictorial representation of stress components at a point of interest.	118
Figure A.2:	Strain elongation and shear [111].	119
Figure A.3:	Shear strain representation [111].	120
Figure A.4:	(a) Mechanical analysis of micro unit of diaphragm [111] (b) Simplified top view of a thin plate.	125
Figure B.1:	(a) Electrical resistance of a homogeneous bar with dimensions of length (l) \times width (w) \times thickness t and resistivity (ρ), (b) When subjected to loading, all three can potentially change, leading to a change in the measured electrical resistance [94].	132
Figure B.2:	Crystal planes of silicon (a) (100), (b) (110), (c) (111) planes, (d) Diamond cubic lattice of single crystal silicon with each atom covalently bonded to its four neighbours, (e) Wafers smaller than 200 mm in diameter have flat that indicates the $\langle 110 \rangle$ direction, whereas larger wafers have a notch [94].	135
Figure B.3:	The stress components σ_{ij} represents the stress on face i in direction j .	135

	When $i = j$ and $i \neq j$ represents normal and shear stress components respectively [94].	
Figure B.4:	Schematic of Smith's test configurations for calculating a) Longitudinal, and b) Transverse piezoresistive coefficients.	138
Figure B.5:	Orientation dependency of the piezoresistive coefficient for p-type and n-type semiconductor resistors for lightly doped silicon in the (100) plane [94].	142
Figure B.6:	Piezoresistance factor $P(N, T)$ as a function of impurity concentration and temperature for (a) p-type, and (b) n-type Si. The plots are based on the data presented by Kanda [71].	144
Figure C.1:	Schematic representation of a piezoresistive pressure sensor; (a) Cross section view, (b) Top view of diaphragm, and (c) Wheatstone bridge configuration.	145

LIST OF TABLES

Table No.	Details	Page No.
Table 2.1:	Anisotropic etchant used for silicon.	11
Table 2.2:	Properties of materials used for MEMS[33].	15
Table 3.1:	Material properties of silicon [81].	35
Table 3.2:	Stress and deflection sensitivities of the various diaphragm structures, analysed using mapped brick mesh with parabolic hex element with 27 nodes.	39
Table 3.3:	Stress and deflection sensitivities for the diaphragms with different edge lengths and a thickness of 150 μm .	42
Table 3.4:	Selected dimensions of diffused pressure sensor for 20 MPa pressure range.	50
Table 3.5 :	Diaphragm dimension for half of pressure range pressures sensor for 10 MPa pressure.	50
Table 3.6:	Material properties and gauge factors of Si , Poly-Si, SiC and Diamond used for the simulation study.	56
Table 3.7:	Various parameters calculated from the data presented in Figure 3.22 to 3.32, diaphragm geometry 500 $\mu\text{m} \times 500 \mu\text{m} \times 25 \mu\text{m}$, maximum applied pressure 10 MPa.	65
Table 4.1:	Dimensions for piezoresistors, pad dimensions, contact pad openings and metal line width.	68
Table 4.2:	Dimensions of diaphragm for pressure sensor, pressure range 200 and 100 bar.	68
Table 4.3:	Mask details for piezoresistive pressure sensor.	69
Table 4.4:	Results of testing of signal conditioning circuit.	81
Table 5.1:	Summary of performance parameters of production batch of piezoresistive pressure sensors.	92
Table 6.1:	Performance parameters of the pressure sensors of different types.	103
Table A.1:	Coefficients for maximum stress and deflection in rectangular plates [33]	129
Table B.1:	Gauge factors of different types of strain gauges [113]	133
Table B.2:	Piezoresistive tensor components for lightly doped (10^{16}cm^{-3}) silicon in the (100) plane near room temperature [7]	141
Table B.3	Piezoresistive coefficients for (100) Si and doping less than 10^{18}cm^{-3} [113]	141
Table C.1	Comparison of the sensitivity for various configurations of Wheatstone bridge	147

LIST OF SYMBOLS AND ABBREVIATIONS

Symbol	Description
A	Area
A	Length of plate
a_c	Lattice constant
B	Width of plate
C	Constant in assumed deflection
C_{ijkl}	Elastic stiffness matrix
D	Flexural rigidity
E	Young's Modulus
E_F	Fermi energy
F	Force
F_s	Fermi integral function
G	Shear Modulus
GF	Gauge factor
H	Thickness of plate
h,k,l	Miller index
h_c	Plank's constant (i.e.)
k_b	Boltzmann constant
l,m,n	Direction cosine
l_b	Length of semiconductor bar
M	Bending moment
N	Electron concentration
N	Concentration
NL_i	Nonlinearity of pressure sensor
P	Applied pressure
P	Hole concentration
$P(N,T)$	Piezoresistive factor
Q	Shear moment
Q	Electron Charge (1.6×10^{-19} C)
R	Resistance
R_b	Bridge resistance
R_{dl}	Resistance of depletion layer and grain boundary for polysilicon
R_g	Resistance of grain conducting region for poly silicon
R_{se}	Series resistance
R_{sh}	Shunt resistance
S	Sensitivity of Wheatstone bridge
S_{ijkl}	Compliance matrix
S_p	Sensitivity of pressure sensor
T	Temperature
T_b	Thickness of semiconductor bar
TCR	Temperature coefficient of resistance
T_s	Stress Tensor
U	Displacement of plate in x-axis direction
V	Displacement of plate in y-axis direction
V	Number of carrier valleys
V	Supply voltage
V_l	Velocity
V_o	Output voltage
W	Displacement of plate in z-axis direction
w_b	Width of semiconductor bar

Greek Symbols

ρ_d	Density
Σ	Stress
T	Shear stress
E	Strain
Y	Poisson's ratio
Γ	Shear strain
Π	Piezoresistive coefficients
Δ	Change
δ	Assumed deviation in resistance
∇	Laplacian operator
A	Geometrical constant for maximum deflection
B	Geometrical constant for maximum stress
m_{eff}	Density of state effective mass
α_l	Change in resistance in longitudinal direction
α_t	Change in resistance in transverse direction

Subscript

A	Atmospheric
D	Dynamic
D	Density
DI	Depletion layer
G	Grain
L	Longitudinal
max	Maximum
n	Electron
p	Hole
r	Radial direction
ref	Reference
S	Static
T	Total
t	Transverse
x	X-axis direction
y	Y-axis direction
z	Z-axis direction
θ	Angle

Abbreviations

DRIE	Deep Reactive Ion Etching
EDP	Ethylene Diamine Pyrocatechol
FEM/A	Finite Element Method / Analysis
IC	Integrated Circuit
KOH/IPA	Potassium Hydroxide/Isopropyl Alcohol
LIGA	Lithographie, Galvanoformung, Abformung
MEMS	Micro-Electro-Mechanical Systems
MST	Microsystem Technology
PCB	Printed Circuit Board
PE, LP, CVD	Plasma-Enhanced, Low-pressure, Chemical Vapor Deposition
SOI	Silicon-On-Insulator
TMAH	Tetra Methyl Ammonium Hydroxide
TO	Transistor Outline

SYNOPSIS

Pressure sensors have a wide range of applications in several areas such as process control instrumentation in manufacturing industries, oil & gas, automotive, medical, avionics & aerospace, nuclear power plants, etc. Due to junction leakage, the operating temperature of the commercial sensors is limited to 125 °C. Several applications demand operation in stringent conditions such as higher temperature, ionizing radiation, etc. Hence, the development of pressure sensors for applications involving higher temperature and radiation environment is still an area open to research. The motivation behind the present thesis work is to develop piezoresistive pressure sensors which can work beyond the operating temperature range of commercial pressure sensors i.e. up to 125 °C and to understand gamma radiation induced performance degradation of pressure sensors. The extensive FEM simulation studies were carried out to analyse the effect of various parameters such as geometry & thickness of bulk micro machined diaphragm, piezoresistor location, piezoresistor doping concentration, diaphragm and piezoresistor materials, etc., on the pressure sensors performance. The optimisation of the design parameters were done using simulation studies to fabricate pressure sensors. Based on optimised design parameters, pressure sensor mask layouts were completed for fabrication of pressure sensor chip. The pressure sensors were designed for 100 bar/200 bar full scale ranges using two fabrication process flows (diffused piezoresistors and SOI). The pressure sensor chips were wire bonded and attached with the TO -12 header with stainless steel package for performance investigation. Performance investigations were done in terms of sensitivity, linearity, offset voltage, offset drift, hysteresis, etc under room temperature to elevated temperature conditions. In addition, the experimental investigations on the failure mechanism of piezoresistive pressure sensors were performed under the gamma radiation exposure.

The important contributions of this thesis work are summarized below:

- (i) An extensive simulation study for studying the effect of various design parameters on the response of pressure sensors has been presented. The effect of temperature on the pressure sensor performance was modelled and change in the response was quantitatively presented using the FEM analysis. Based on the analysis of the data, the design parameters of the pressure sensors were finalized for the fabrication.
- (ii) The quantitative simulation study of the piezoresistive pressure sensors using the wide band gap materials such as diamond and SiC has been carried out to theoretically estimate the response of the piezoresistive pressure sensors based on these materials. The results presented would be useful for designing the sensors based on these materials for high temperature high radiation operating environment.
- (iii) Pressure sensors using two types of process flows i. e. diffused resistor based process and SOI technology have been designed, fabricated and characterized. The performance investigation of the fabricated sensors has been carried out at different pressures and temperatures in terms linearity, offset voltage, sensitivity and hysteresis. The prototypes developed have shown expected performance up to operating temperature of 100 °C and 200 °C for diffused piezoressitor based and SOI technology based pressure sensors respectively. The SOI technology based sensors operated without failure up to 200 °C temperature with degradation of ~ 19% in the sensitivity. The temperature of 200 °C is well beyond the operating temperature range of 125 °C of commercial sensors. The sensor would be suitable for deployment in process control instrumentation with a temperature compensation circuit. A compact signal conditioning circuit has been designed and fabricated for processing the Wheatstone bridge output of the pressure sensor in to 4-20 mA current output with offset voltage compensation.

(iv) Gamma radiation induced degradation of two types of sensors i. e. with an oil filled package and without oil filled package have been carried out for understanding the failure mechanism of the piezoresistive pressures sensor. The experimental results clearly show that packaging of the sensor in terms of isolation oil could play a significant role in determining the radiation hardness of the sensors.

Chapter 1. INTRODUCTION

Pressure sensors have a broad range of applications in the several areas such as process control instrumentation in manufacturing industries, oil & gas, automotive, space, medical, etc. Micro-electro-mechanical-systems (MEMS) technology has played a significant role in the evolvement of miniaturised pressure sensors along with integration of microelectronics. For industrial applications, there are two major categories of pressure sensors, firstly based on piezoresistive transduction technique and secondly, based on capacitive transduction technique. Simplicity of fabrication, simple signal conditioning electronics, linearity and accuracy in pressure measurement are most preferred attributes of MEMS technology based piezoresistive pressure sensors. The MEMS technology for the fabrication of such pressure sensors for normal operating conditions has been well established.

Several industries (e.g. nuclear reactors, oil & petroleum industry, automobile industries, avionics & aerospace industries, etc.) demand pressure sensors operating in stringent conditions such as high temperature and/or radiation. Commercially available piezoresistive pressure sensors by different global manufacturers can be operated up to 125 °C operating temperature. Therefore, the enhancement in the operating temperature range of the piezoresistive pressure sensors is still an area of research. In addition, the performance of these sensors degrades when operated in an ionising radiation environment for e.g. applications in nuclear reactors and space. So far, only limited studies on radiation effect on piezoresistive pressure sensors have been reported in the literature. Therefore, the present thesis is focused on the design, fabrication and characterisation of MEMS technology based piezoresistive pressure sensors for enhancing the operating temperature of pressure sensors up to 200 °C and on the study of

ionising radiation-induced degradation of the performance of piezoresistive pressure sensors.

1.1 OBJECTIVE OF THE RESEARCH WORK

The objectives of the thesis work are as follow:

- a. FEM simulation study to investigate the effect of pressure sensor design parameters on the performance of sensors and design parameter optimization.
- b. Fabrication of MEMS piezoresistive pressure sensor using different processes.
- c. Development of characterisation setups for MEMS piezoresistive pressure sensors and signal conditioning circuit.
- d. Performance investigation of MEMS piezoresistive pressure sensor in terms of sensitivity, linearity, offset voltage, offset drift, hysteresis, etc.
- e. Study of the radiation effects on the MEMS piezoresistive pressure sensors.

1.2 ORGANISATION OF THE THESIS

This thesis is organised in the seven Chapters as given below:

Chapter 2 presents a comprehensive literature survey encompassing a review of MEMS technology based sensors. This involves the history of micromachining and MEMS, MEMS fabrication processes, materials used for MEMS devices, etc. The mathematical modelling of the pressure sensor using the theory of thin plate and theory of piezoresistivity in single crystalline silicon are explained in this Chapter. The analysis of pressure sensor response based on Wheatstone bridge configuration is also presented.

Chapter 3 deals with FEM simulation study of piezoresistive pressure sensors. An introduction to the simulation tool and steps to build a solid model of the pressure sensor

are discussed with a flow diagram. The results of the simulation study of piezoresistive pressure sensor performed in order to investigate the effect of various design parameters and the analysis of the data are presented. The change of pressure sensors response due to increased temperature in oxide isolated piezoresistor based pressure sensor is discussed. A comparative study of piezoresistive pressure sensor based on wide bandgap materials such as silicon carbide and diamond is presented. These materials are alternate materials for extending the operating temperature of pressure sensors beyond 125 °C.

Chapter 4 illustrates the design of mask and the fabrication process of the pressure sensors for diffused piezoresistors and SOI technology based pressure sensors. Additionally, development of the signal conditioning circuit to compensate for the offset voltage and to get an industrial standard 4-20 mA output response is presented.

Chapter 5 discusses the performance investigation results of piezoresistive pressure sensors (for diffused and SOI technology base pressure sensors). The performance has been evaluated in terms of parameters such as pressure response, sensitivity, offset voltage, offset drift in room temperature, linearity and hysteresis, etc. The measurements were carried out at room temperatures and also in higher temperature environments.

Chapter 6 presents the experimental investigation of gamma radiation-induced degradation of piezoresistive pressure sensors in order to draw inference for the degradation of the performance of piezoresistive pressure sensors.

Chapter 7 includes significant conclusions obtained from the current research work, recommendation for future scopes and contribution of this research towards the research field of piezoresistive pressure sensors.

Finally, appendices are presented at the end of thesis, which include the mathematical modelling of the piezoresistive pressure sensor using theory of thin plate, piezoresistivity and analysis of Wheatstone bridge in detail.

Chapter 2. LITERATURE SURVEY

2.1 INTRODUCTION

Today, the field of Micro-Electro-Mechanical Systems (MEMS) is growing at a faster pace in various areas. A pressure sensor is one of the first mature and commercialised device based on MEMS technology. These sensors have potential applications in several industries, e.g. process control, oil & petroleum, automobile, aerospace/avionics and consumer devices, etc. Integration of micromachining technology with IC technology resulted in the development of MEMS technology to realise various microstructures for sensors and actuators. MEMS technology led to advanced functionality, improved performance, smaller size and reduced cost for microsystems. Widely, the microsystems are recognised as MEMS or microsystems technology (MST) in Europe. Typically, the dimensions of MEMS devices are ranging from nanometres to millimetres. The advancement in R&D of micromachining processes along with integrated circuit technology (IC) has resulted in the expansion of MEMS technology for various applications. An overview involving the current demands of MEMS, the status of MEMS devices market and various processes adopted for MEMS fabrication, etc. is presented in next sections. In addition, mathematical models in terms of thin plate theory and theory of piezoresistivity are presented in details for piezoresistive pressure sensors

2.2 STATUS OF COMMERCIAL MEMS DEVICES

Recent years have been a golden era for the market of MEMS technology based devices. The use of microsensors such as pressure sensors, accelerometers, microphones, gas sensors, etc., are increasing in various industries [1]–[3]. In general, growing demand for MEMS devices in the Internet of Things (IoT) and wearable electronics makes them a

very promising sensing devices for consumer and industrial applications. Deployments of MEMS devices in various industries such as automotive, defence, space/avionics, nuclear power plant, etc. are very demanding area of applications for these devices.

The MEMS pressure sensor is currently leading the market with large share and it is expected to grow significantly by 2021 [4], [5]. The MEMS industry is creating new possibilities and it is facing new challenges. Previously, the challenge was a reduction in the size of MEMS chip, which in turn led to the decrease in price due to mass production based on the batch fabrication process. New trends in the field of MEMS research and developments are (R&Ds) [4]:

- a. Device development based on dedicated applications
- b. Fusion of different sensors
- c. Decreasing power consumption⁴

Therefore, the new trends are towards the performance enhancement of MEMS devices by sacrificing the chip size of sensing devices. The fabrication of such devices uses MEMS technology. In the next sections, micromachining and MEMS are discussed.

2.3 ADVANCEMENT IN MICROMACHINING AND MEMS TECHNOLOGY

MEMS is a technology that combines the process of micromachining with microelectronics to produce tiny sensors and actuators with several functionalities. The miniaturised mechanical structures such as diaphragm, cantilever, valves, gears, mirrors, are combined with microelectronics on a common substrate. In general, silicon wafers are used as a substrate. MEMS is an interdisciplinary field for R&D which involves design, engineering and manufacturing proficiency from a vast and diverse technical fields of science & technology. It comprises several domains such as IC fabrication technology,

mechanical engineering, material science, electrical engineering, chemistry and chemical engineering, fluid mechanics, optics, instrumentation, and packaging technology. The major microfabrication processes used for MEMS are i) lithography and micromachining for micro devices, ii) fabrication process adopted from IC technology (oxidation, doping, metallisation, die attachment, bonding, packaging, etc.), iii) special MEMS processes (LIGA, DRIE, etc.), and iv) fabrication process adopted from optics manufacturing (polishing and finishing, etc.). Micromachining is utilised to fabricate 3D microstructures as the foundation of MEMS devices [6].

The development of micromachining techniques at industrial level led to the introduction of sensors in commercial market, i.e. pressure sensor, accelerometer and later on the gyroscopes. Silicon is a primary material for structural element (as primary sensing) and transduction element (as secondary sensing) for MEMS technology based sensors. The discovery of silicon by Berzelius in 1824 is accountable for revolution in the field of microelectronics. Whereas, Smith had accelerated the era of MEMS with the discovery of piezoresistivity in the silicon and germanium [7]. Uhlir had become a pioneer to adopt single crystalline silicon in MEMS with the discovery of porous silicon [8]. His discovery ultimately led to development of various sensors based on the single crystalline silicon for MEMS devices. The invention of piezoresistivity demonstrated that gauge factor of semiconductor thin film strain gauge is 10-20 times larger than the metal thin film strain gauge and hence, a more considerable sensitivity of semiconductor based strain gauges [7]. Semiconductor (Si) based strain gauges were commonly available for various sensing applications from 1958 and became one of the mature sensing technologies by Kulite Inc. and Honeywell Inc. [9]. In 1970s and 1980s, MEMS commercialisation was started in full pace by various companies (e.g. Foxboro ICT, Transensory Devices, IC Sensors, IC

Transducers, Kulite Inc. and Novasensor). During the same era, Kurtz Petersen had discussed 'Silicon as a mechanical material' that worked as driving force for the development of MEMS devices based on silicon and also helpful in increasing awareness for the possibility using silicon in MEMS [10]. Further, development based on polysilicon micromachining process was done at the University of California, Berkeley by Howe and Muller [11]. Moreover, the ideas presented by Professor R Feynman in December 1959 during his famous presentation entitled on "There's Plenty of Rooms in Bottom" was responsible to speed up the R&D in field of MEMS technology [12], [13].

2.4 MEMS MANUFACTURING TECHNIQUES

Various manufacturing processes and materials are utilised to fabricate MEMS, which are adopted from integrated circuit (IC) technology, micromachining and optics. MEMS technology provided a driving force for R&D of other non-traditional microfabrication processes and materials. These processes are briefly described below.

2.4.1 Conventional IC technology processes and materials

The conventional processes and materials used in traditional IC technology are directly adopted for fabrication of MEMS devices. These processes are photolithography, thermal oxidation, dopant diffusion, ion-implantation, plasma activated chemical vapour deposition (PCVD), plasma-enhanced chemical vapour deposition (PECVD), evaporation, sputtering, etching, reactive ion etching (RIE), etc. Silicon, silicon dioxide, silicon nitride, polysilicon, aluminium are commonly used materials for the fabrication of IC and MEMS using these processes.

2.4.2 Additional processes and materials used in MEMS

In addition to IC fabrication processes, some advanced methods and materials are used in MEMS technology. These processes are anisotropic wet etching for single crystalline silicon, deep reactive ion etching (DRIE), X-ray lithography, electroplating, low-stress LPCVD, thick film resist (SU-8), spin casting, micro moulding, and batch micro-assembly, etc. The common materials used for fabrication of MEMS devices are crystalline silicon, polycrystalline silicon, piezoelectric films (PZT), magnetic films (Ni, Fe, Co and rare earth alloys), high temperature materials (SiC, ceramics, SOI, diamond), aluminium, stainless steel, platinum, gold, sheet glass and plastic (PVC and PDMS). Crystalline silicon is not only an excellent electronic material, but it also shows better mechanical properties comparable with steel.

2.5 CLASSIFICATION OF MEMS FABRICATION AND ETCHING PROCESSES

The following micromachining techniques are used to integrate multiple microstructures and patterns in complex MEMS devices [14], [15]. The micromachining is a process to define and etch structures with micron features sizes.

The classification of MEMS micromachining processes is as follow:

- a. Bulk micromachining
- b. Surface micromachining
- c. High aspect ratio micromachining

Micromachining involves partial or bulk removal of material from the substrate to create the microstructures. The removal of material is done by etching which can be isotropic or

anisotropic depending on the crystal orientation of the material. The fabrication of high aspect ratio structures is done using a combination of a wet and dry etching process. Single crystalline silicon etching with aqueous KOH solution was introduced in 1960s. Since MEMS structures are high aspect ratio structures, anisotropic deep silicon etching was introduced by Waggener et al. 1967 [16]. The details of etch rate for micromachining process to fabricate microstructures have been presented earlier [17].

2.5.1 Bulk micromachining

Bulk micromachining is the oldest fabrication technology to create microstructures for MEMS. The technique involves selective removal of substrate material in order to create tiny mechanical structure [14]. Anisotropic wet etching of single crystalline silicon results in V-grooves, channels, membrane, vias, nozzles, and cantilever by selective removal of the bulk material. The microstructures realized using anisotropic wet etching are depicted in Figure 2.1 (a). The deep reactive ion etching (DRIE) is a dry etch process to etch deeply into silicon wafer while leaving vertical walls and it is independent of crystallography orientation (Figure 2.1 (b)). Another process is micromoulding, which is the combination of DRIE and conformal deposition process (i.e. LPCVD) to create microstructures for MEMS.

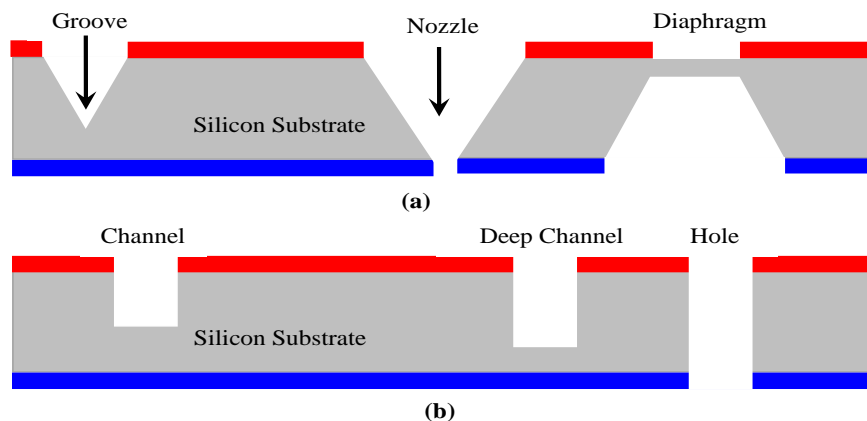


Figure 2.1: Bulk micromachining, (a) Anisotropic wet etching, (b) Deep reactive etching.

The process of chemical etching involves the immersion of a substrate into a chemical etchant to selectively etch out bulk material from the exposed substrate surface. The chemical wet etching process is popular in MEMS industries because of high etch rate and selectivity. The etch rate and selectivity are controlled by changing the chemical composition and temperature of etching solution. In isotropic etching, silicon is etched uniformly in all directions. However, in anisotropic etching, etch rate is dependent on the crystallographic orientation of substrate and the etch rate does not remain same in all direction (Figure 2.2 (a) and (b)). Mainly used anisotropic chemicals for Si bulk micromachining are listed in Table 2.1.

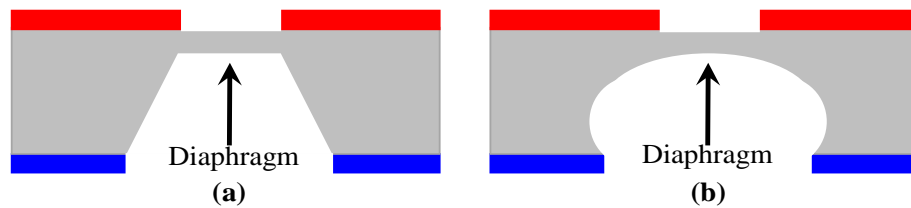


Figure 2.2: Types of etching, (a) Anisotropic etching, (b) Isotropic etching.

Table 2.1: Anisotropic etchant used for silicon.

Etchant	Operating temp (°C)	Etching rate (R) for orientation 100 (µm/min)	S=R100/R111	Mask materials
Ethylenediamine pyrocatechol (EDP) [18]	110	0.47	17	SiO ₂ , Si ₃ N ₄ , Au, Cr, Ag, Cu
Potassium hydroxide/Isopropyl alcohol (KOH/IPA)	50	1	400	Si ₃ N ₄ , SiO ₂ (etches at 2.8 nm/min)
Tetramethylammonium hydroxide (TMAH) [19]	80	0.6	37	Si ₃ N ₄ , SiO ₂

2.5.2 Surface micromachining

Surface micromachining is a process in which material is added on substrate to create microstructures. In bulk micromachining, the bulk material is removed from the substrate to realize a microstructure for sensing applications. The first surface micromachining structure for the resonant gate transistor was introduced by Nathanson [20]. This process

is utilised to fabricate low aspect ratio structures (Figure 2.3 (a, b, c)). Since this process is compatible with complementary metal oxide semiconductor (CMOS) process and hence, it is more suitable for integration with microelectronics. Two methods are utilised to deposit structural materials: (a) CVD (b) electroplating. Surface micromachining produces wide varieties of MEMS devices for many different applications [21].

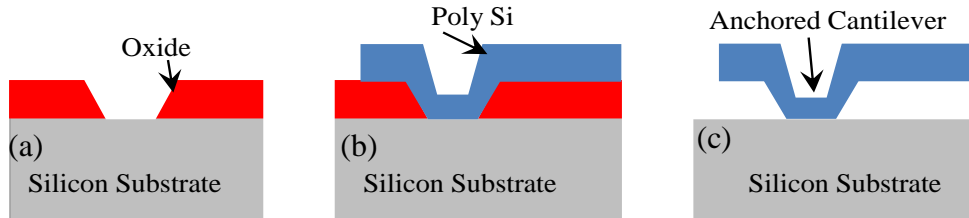


Figure 2.3: Illustration of the surface micromachining process.

2.5.3 High aspect ratio micromachining

The requirements of MEMS for some particular applications have led to the development of non-silicon microfabrication techniques. These techniques are discussed below.

2.5.3.1 LIGA

LIGA is a German acronym for lithographie, galvanofornung, abformung (i.e. lithography, electrodeposition and plastic moulding) [22]. It was developed in the Institute for Microstructure Technology at the Nuclear Research Centre, Karlsruhe, Germany [23], [24]. The LIGA is a fabrication process for High Aspect Ratio MEMS structures that was developed in the early 1980s [25]. In LIGA process, an X-ray beam is used to transfer a pattern from the mask to a thick resist layer and the resist is developed as a mould for electro-deposition of metal. A pictorial representation of LIGA process is given in Figure 2.4. LIGA essentially combines exceptionally thick film resist (often > 0.5 μm thick), and high energy X-ray lithography (~ 1 GeV) to pattern the resist to achieve vertical sidewall structures. The drawback is the requirement of high-energy X-

ray sources. The remarkable characteristics of X-ray LIGA-fabricated structures are high aspect ratios (order of 100:1), vertical and parallel side walls (angle of 89.9°), smooth sidewalls suitable for optical mirrors and height of structure from 10's μm to several millimetres.

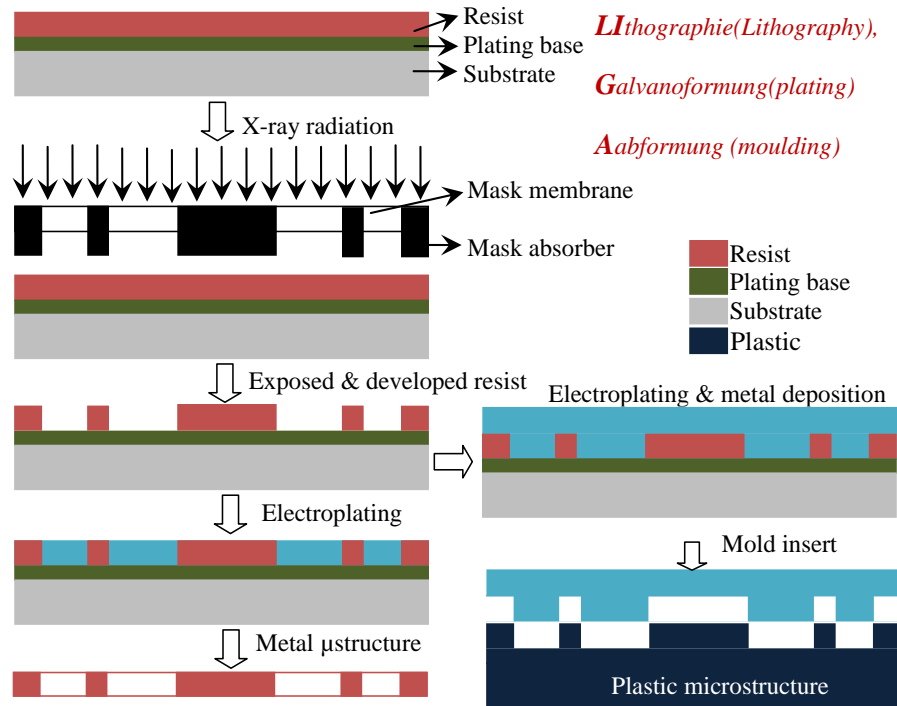


Figure 2.4: Schematic of the LIGA process [22].

2.5.3.2 SU-8 (UV LIGA)

The dependency on X-ray source is a significant drawback of the LIGA process. Hence, an alternative is developed using SU-8 as a negative resist. SU-8 as a substrate for LIGA is very cheap and with nearly similar performance. SU-8 is a particular epoxy-resin-based optical resist that can spin on in thick layers ($> 500 \mu\text{m}$) and patterned with commonly available contact lithography tool. It allows to achieve vertical sidewalls with high aspect ratio structures [26]. SU-8 is biocompatible and chemically stable material.

2.5.3.3 Plastic moulding with PDMS

Polydimethylsiloxane (PDMS) is a transparent material that is poured over a mould and

simply peeled off out from mould substrate after polymerisation [27]. Based on this single mould, many expensive structures can be fabricated. The PDMS faithfully reproduces even submicron features in a mould. PDMS is biocompatible and thus it is used in a variety of BioMEMS applications. Since PDMS is transparent, tissues, cells and other materials can be easily imaged through it.

2.5.4 Substrate bonding

In order to get mechanical support, long term stability and reliability of microstructures, the microsystems chips are bonded with another wafer i.e. silicon, glass, metal and polymeric wafer substrates. MEMS sensing chip is bonded with glass substrate to create cavity sealing or vacuum, or reference cavity or to accommodate deflection of cantilever beam/thin diaphragm. The techniques used to bond silicon wafer with other substrate are field assisted bonding (anodic bonding) invented by Wallis and Pomerantz [28], silicon fusion bonding (SFB) by Shimbo [29], [30]. Field assisted thermal bonding (anodic or electrostatic bonding or Mallory process) is commonly used to bond silicon with glass at a high temperature (e.g. 400 °C) and at a high voltage (e.g. 600 V). Silicon fusion bonding (SFB) is a process to join two Si wafers at high temperature (> 800 °C) in an oxidising environment without applying an electric field and no intermediate layer for bonding. Also, eutectic [31] and adhesive bonding [32] are used for wafer bonding.

2.6 ADVANTAGES OF SILICON FOR MEMS FABRICATION

Although several materials could be used for the fabrication of MEMS, silicon has unique advantages. The single crystal silicon is not only an excellent electronics material, but it also exhibits superior mechanical properties for MEMS. Micromachining has been validated in a variety of materials including metals, glasses, ceramics, polymers, and

various alloys. Material properties of few MEMS materials are listed in Table 2.2. Out of the mentioned materials, silicon is strongly associated with MEMS due to the extensive use of silicon within IC industry and availability. Silicon has excellent, controlled and well-understood electrical and mechanical properties. Silicon is also compatible with design tools existing at industries for the optimisation of the design of the microstructures for sensors and actuators

Table 2.2: Properties of materials used for MEMS[33].

Material	Yield Strength (GPa)	Knoop Hardness (kg/mm²)	Young's Modulus (GPa)	Density (g/cm³)
Diamond*	53	7000	1035	3.5
SiC*	21	2480	700	3.2
Al ₂ O ₃ *	15.4	2100	530	4.0
Si ₃ N ₄ *	14	3486	385	3.1
SiO ₂ (fibers)	8.4	820	73	2.5
Si*	7.0	850	190	2.3
Steel (Max Strength)	4.2	1500	210	7.9
Stainless Steel	2.1	660	200	7.9
Al	0.17	130	70	2.7

*MEMS materials

2.7 FABRICATION PROCESSES FOR MEMS

The fabrication techniques used for MEMS based on silicon consist of conventional methods developed for integrated circuit technology. Three essential elements in traditional processing of silicon (i.e. deposition, lithography, and etching) are adopted for MEMS fabrication. A pictorial representation of such processes is given in Figure 2.5. Deposition includes, i) oxidation, ii) chemical vapour deposition, iii) physical vapour deposition and iv) epitaxial growth. Lithography includes, i) optical beam, ii) electron beam and iii) X-ray lithography. Etching involves, i) dry etching and ii) wet etching processes. Many of these processes are modified for the fabrication of MEMS, for

example, use of thick photoresists, grey scale lithography, or deep reactive ion etching. Other techniques which are specially developed for MEMS but not used in IC fabrication are surface micromachining, wafer bonding, electroplating, LIGA, ion beam etching and deposition. Since the focus of the present work is MEMS technology based pressure sensor, an overview of these pressure sensors is presented in the consequent section.

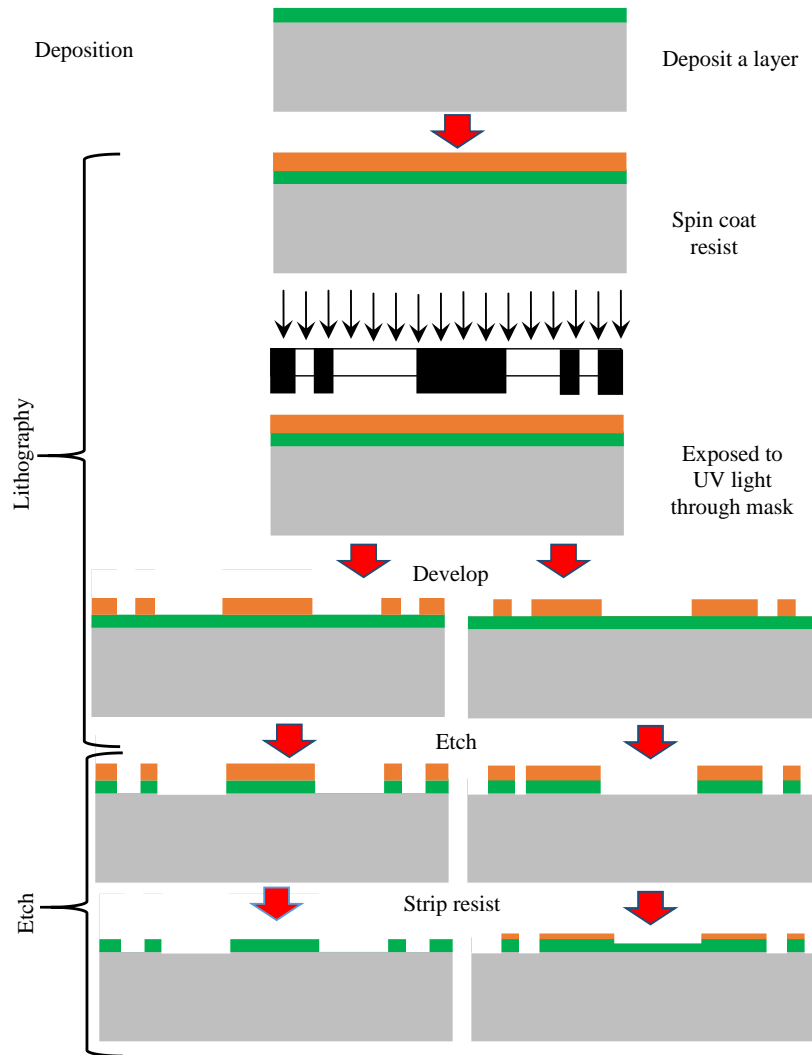


Figure 2.5: Schematic explanation of deposition, lithography and etching process with positive photoresist and negative photoresist [6].

2.8 MEMS PIEZORESISTIVE PRESSURE SENSOR: INTRODUCTION

Generally, the fabricated pressure sensor chip consists of a thin silicon diaphragm, piezoresistors and metal lines to connect the piezoresistor in a Wheatstone bridge

configuration. The chip also has the pads for wire bonding. A microscopic view of the die of the chip from the top side is presented in Figure 2.6 (a) and actual die with wire bonding is shown in Figure 2.6 (b). The sensor chip attached on TO header with wire bonds shown in Figure 2.6 (c). Actual packaged pressure sensor with electrical connection is shown in Figure 2.6 (d).

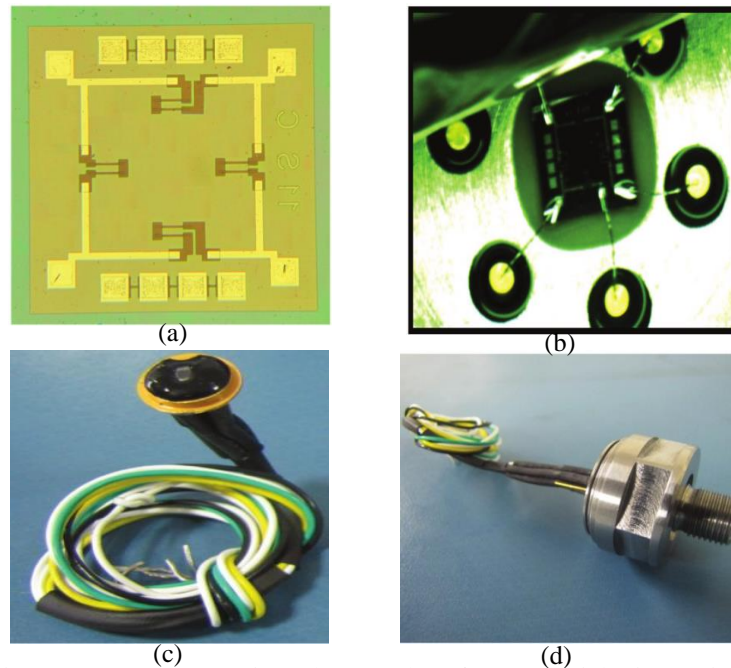


Figure 2.6: Representative photographs of commercial piezoresistive pressure sensor, (a) Top view of chip, (b) Chip mounted on TO header, (c) Wire connected with TO header, (d) Packaged pressure sensor with electrical connection [34].

The schematic of the final packaged pressure sensor is shown in Figure 2.7 with an exploded view in order to get a better understanding of the actual pressure sensor [34].

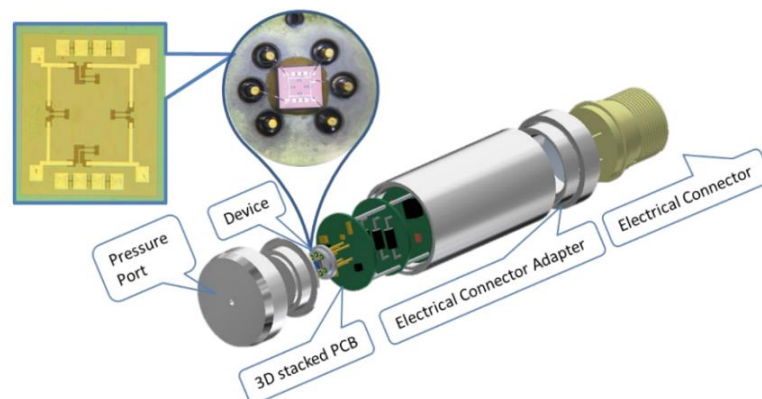


Figure 2.7: Schematic of pressure sensor with exploded view [34].

Various packages are available for the pressure sensors depending on the application requirements. Some of the commercially available packages are shown in Figure 2.8 (a)-(d). These include; i) a sensor housing with a single monolithic silicon pressure sensor die by Motorola MPX 2010 DP, ii) a dual in-line package (DIP) based miniature surface mount sensor by First Sensor which allows for PCB-mounting, and iii) DIP package sensor for assembly on PCB by AMSYS, and iv) a packaged pressure sensor by Honeywell Inc. for industrial heavy-duty applications.

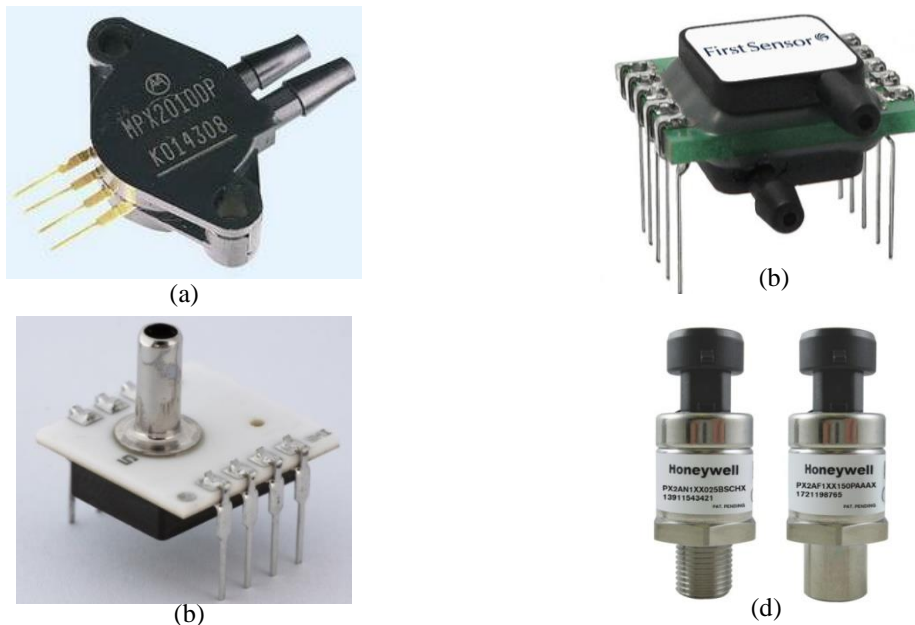


Figure 2.8: Various types of commercial packaging of pressure sensor: (a) Sensor housing a single monolithic silicon pressure sensor die by Motorola MPX 2010 DP, (b) Miniature surface mount technology with DIP housings allow for PCB-mounting by FirstSensor, (c) (DIP for assembly on PCB by AMSYS, (d) Pressure sensor by Honeywell Inc. for heavy duty applications.

2.9 CLASSIFICATION OF PRESSURE SENSORS

2.9.1 Classification based on transduction techniques

2.9.1.1 Piezoresistive pressure sensors

The piezoresistive effect is utilised in a variety of sensing devices as the transduction technique since its invention by Smith in 1954 for silicon and germanium [7]. The piezoresistive effect is a change of resistance due to applied strain/stress. The

strain/stresses are induced by means of external force or pressure. Generally, pressure sensors have thin diaphragm/micro cantilever, piezoresistors and reference cavity. The piezoresistors are diffused or ion implanted at high stress concentration regions of the microstructures. The resistance change is observed to be linear with respect to the applied pressure for small deflection of microstructures. Metal and semiconductor both exhibit the change in resistance due to the applied pressure/load/force. However, the change in resistance for the metal is dominated by the deformation of geometrical dimensions whereas change in resistivity is dominated in case of semiconductor. The change in resistance is constant irrespective of crystal orientation in metals and known as the isotropic effect. However, the change in the resistance is not constant irrespective of crystal orientation for semiconductor materials known as an anisotropic effect [35]. The change in resistance due to temperature is also observed which is known as thermoresistive effect [36]. It is to be noted that piezoresistive effect in the semiconductors is 10-20 times higher than the metal counterpart, hence use of the piezoresistive transduction technique has gained more popularity in MEMS devices. Initially, the piezoresistors were fabricated by selective diffusion of the boron in N-type Si wafer. The Si wafer with piezoresistors integrated is bonded to the glass or metal by epoxy (Figure 2.9 (a)). A schematic of a pressure sensor formed by bulk removal of silicon is shown Figure 2.9 (b). The schematic of anisotropic etched piezoresistive pressure sensor is shown in Figure 2.9 (c).

The accuracy of the mechanical structures is controlled in the range of microns and hence it is referred as micromachining technology. The salient features of pressure sensors based on silicon using micromachining technology are:

- a. Silicon is used as a structural element (primary sensing) and the piezoresistors as

a transduction element (secondary sensing).

b. Micromachining technology facilitates batch fabrication of sensing devices.

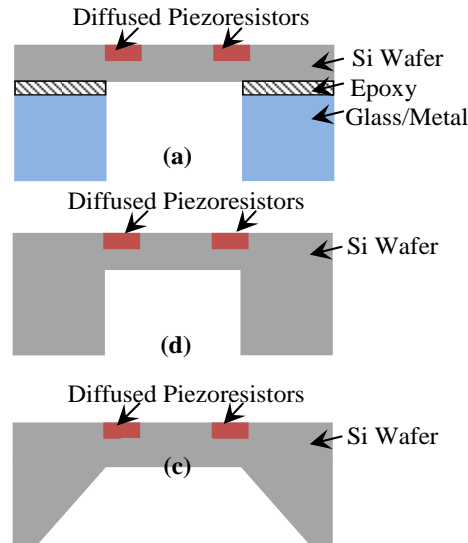


Figure 2.9: (a) Diffused piezoresistive pressure sensor: silicon wafer bonded with glass/metal, (b) Diffused piezoresistive pressure sensor using DRIE etching, (c) Diffused piezoresistive pressure sensor by anisotropic wet etching.

2.9.1.2 Capacitive pressure sensor

Piezoresistive pressure sensors are widely used in industries due to well established and developed fabrication technology. These sensors have good linearity, high sensitivity, ease of signal processing, etc. [37], [38]. However, piezoresistive sensing technique based sensors have some drawbacks such as high-temperature sensitivity and the piezoresistors are susceptible to junction leakage. An alternative technique is the use of capacitive sensing technique. A schematic of the capacitive pressure sensor is shown in Figure 2.10.

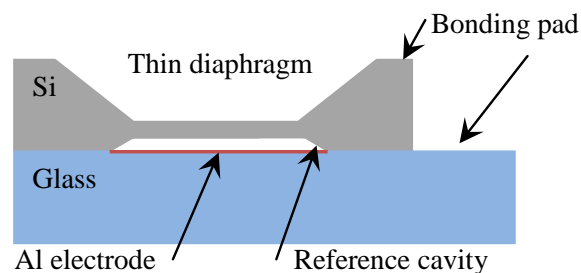


Figure 2.10: Schematic of a basic capacitive pressure sensor.

A silicon chip with the embedded thin diaphragm is hermetically bonded to a glass plate face to face by electrostatic bonding. The thin silicon diaphragm acts as an electrode of a capacitor and thin film metal on glass under diaphragm works as another electrode. The gap between the two plates is of the order of few microns. The operating principle of capacitive sensing based devices is based on the measurement of the change in the capacitance between two plates. A capacitive sensing technique is highly nonlinear, but it is immune to adverse effects. It is susceptible to radiation effects due to the accumulation of charge by ionising radiation. Hence, in a radiation environment, piezoresistive sensing is a more suitable technique. The capacitive sensing mechanism based sensor poses more difficulties in the measurement of small capacitance change due to parasitic & stray capacitance effects and electromagnetic interference from the environment.

2.9.1.3 The resonance based pressure sensors

The vibration frequency of a mechanical diaphragm or beam is changed with the external applied force/pressure. The change in the vibration frequency is calibrated in term of the applied physical parameters [39]. Sensors fabricated based on this transduction mechanism is known as resonant sensors. The mechanical properties of the resonator microstructure determine the stability of resonant sensors.

2.9.1.4 Piezoelectric pressure sensors

Piezoelectricity is the generation of charge under the induced strain. The sensors for the measurement of pressure using piezoelectric effect are known as piezoelectric pressure sensors. These sensors used for dynamic pressure measurements and not for static pressure measurements. Generally, a piezoelectric sensing element is fabricated by lead zirconate titanate (PZT) or zinc oxide (ZnO). A piezoelectric material is deposited in high

stress or strain area on the diaphragm/cantilever for charge generation due to applied pressure. The piezoelectric transduction technique is also a self-powered mechanism for the sensors.

2.9.2 Classification of pressure sensors based on pressure measurement method

2.9.2.1 Absolute pressure measurement

A pressure measurement with reference to vacuum is known as an absolute pressure measurement. The packaging of pressure sensor chip is crucial for making a vacuum cavity for the reference. The schematic of an absolute pressure sensor is depicted in Figure 2.11. Generally, the manifold absolute pressure (MAP) sensor used for automobile application are absolute pressure sensors. Pressure sensor used for cabin pressure control, satellites and launch vehicles are some of the examples of absolute pressure sensors.

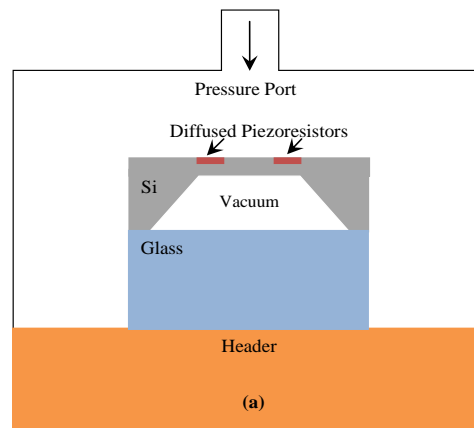


Figure 2.11: Schematic representation of an absolute pressure sensor.

2.9.2.2 Gauge pressure sensor

A pressure sensor used for pressure measurement with respect to atmospheric (ATM) pressure is known as gauge pressure sensor. The packaging of the gauge pressure is designed for atmospheric pressure as a reference pressure. The schematic of a gauge pressure sensor is depicted in Figure 2.12. The pressure sensors used for vehicle tire and

blood pressure are examples of such type of pressure sensors.

2.9.2.3 Differential pressure sensor

Pressure sensors used to measure the difference of pressures is known as a differential pressure sensor. Generally, differential pressure sensors require at least two ports for pressure sensing application. If one of the port gets high pressure, then it leads to the rupture of the thin diaphragm. Hence, safety precautions are taken for the thin diaphragm. The schematic of a differential pressure sensor is depicted in Figure 2.13. Differential pressure sensors are used in medical devices to decide respiratory flow or to define the air flow in the heating ventilating and air conditioning (HVAC) systems.

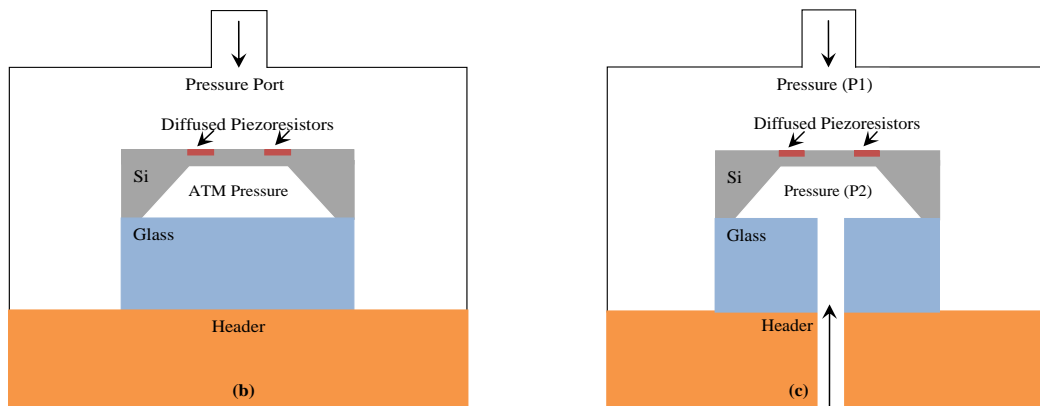


Figure 2.12: Schematic representation of a gauge pressure sensor.

Figure 2.13: Schematic representation of a differential pressure sensor.

2.9.2.4 The symbol used for pressure sensors

The symbols for new generation pressure sensors fabricated with IC technology use a Greek letter psi and the standard symbol for the operational amplifier (Figure 2.14).

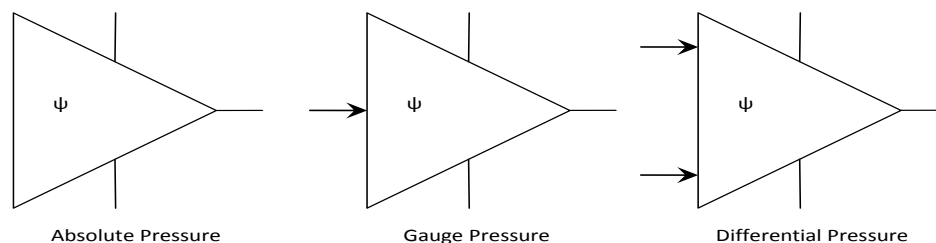


Figure 2.14: Symbols for the pressure transducer.

2.10 RELIABILITY AND USE OF MEMS IN A HARSH ENVIRONMENT

Due to the advancement in MEMS technology, microsystems are being increasingly used in harsh or inaccessible environments involving high temperature, high pressure, (bio)-chemical, mechanical disturbances such as shock and vibrations, electromagnetic noise, radiation, or high vacuum [40]. Such environments are encountered in the industries such as oil/process, chemical, automotive, space, aircraft, medical implants, etc. [40]. The reliability of MEMS devices is an important criteria for the deployment of MEMS based systems in various applications as mentioned above. As MEMS incorporate mechanically moving parts, specific reliability tests are required for evaluating the mechanical reliability in addition to standard electrical reliability tests which are employed for integrated circuits [41]. Standard methods for the evaluation of reliability of MEMS are involved in accelerated testing, temperature cycling, shock and vibrations, burn-in, etc. Since most of the industrial or consumer applications of MEMS do not involve operation in harsh environments, standard reliability test methods used for commercially available MEMS do not include testing of MEMS reliability or failure in such environments. Therefore, it is a keen interest to investigate the reliability of the MEMS devices under the harsh environments such as in high temperature and radiation.

2.10.1 Radiation-induced effects in MEMS

Generally, temperature induced effects are studied for automobile and oil & petroleum industries. However, radiation-induced effects on MEMS is less explored area of research. For applications such as space and near nuclear reactors, the radiation hardness of MEMS becomes the prime concern. The radiations are classified as charged particle radiations such as electrons, protons and other charged particles and uncharged radiations

such as neutrons, X-rays, gamma rays. Energy loss of these radiations in the matter is through ionising energy loss or non-ionising energy loss. Heavy particles such as protons, neutrons and other charged particles are known to create displacement damage in silicon [42]. A lot of research has been carried out to understand radiation-induced degradation of silicon based electronic devices and integrated circuits using ionising radiations such as gamma radiation [43], [44]. However, radiation-induced degradation of MEMS is still not well understood because of higher complexity in terms of materials, packages, types of input-output parameters and sensing or actuating mechanisms. Reviews of radiation effect on silicon based MEMS and emerging MEMS and NEMS based on a variety of materials have been presented by Shea et al. [45] and Arutt et al. [46] respectively. A few studies have been reported on the experimental investigation of radiation effects on MEMS technology based sensors [45], [46], [55], [47]–[54]. The effect of ionising radiations such as gamma, protons and non-ionising radiations such as neutrons on different types of MEMS has been presented in these reports. It has been observed that ionising radiation causes significant degradation in the performance of accelerometers [47]–[50], optical mirrors [51], RF relay switches [52] and resonators [53]. The operation of these devices is based on the electrostatic or piezoelectric actuation of the mechanical elements. The degradation in the performance of these devices has been attributed to the accumulation of radiation-induced trapped charges in the dielectric/silicon dioxide layer under the mechanical element of the MEMS devices due to the radiation environment. In addition, the failure mode was observed to be strongly dependent on the device architecture and technology used in the fabrication. A study of radiation effect due to proton fluence of the order of 10^{16} cm^{-2} on MEMS silicon strain gauges has shown that the radiation observed damage is because of the displacement damage in silicon which

resulted in the change of effective gauge factor [54]. Considering the expected total particle fluence of 10^{11} / cm^2 , which would be accumulated in a device over a 30 year lifetime, from this study, it was concluded that silicon strain gauges are relatively robust to radiation damage for operation at high altitudes [54].

2.10.2 Radiation-induced degradation of silicon

Silicon is prominently used in MEMS as an electrical element as well as a mechanical structural element. Even at the high end of typical doses of Mrad for space applications, the amount of damage to silicon as a mechanical element is considered reasonably small with no remarkable change in Young's modulus [45]. A very few studies have examined the effect of radiation on mechanical properties of materials incorporated in MEMS. A 37% decrease of the modulus of elasticity of a 2 μm thick silicon nitride membrane has been reported with exposure to X-rays with an incident dose of 114 kJ/cm^2 while the Poisson's ratio for the material remained unchanged [56]. The changes in Young's modulus of silicon due to non-ionising energy loss (NIEL) has been reported for high proton fluences of the order of 10^{16} cm^{-2} [54]. For doses of the order of Mrad, the amount of damage to silicon is considered small resulting in an insignificant change in the mechanical properties of silicon [45]. Radiation-induced performance degradation of silicon based MEMS devices are strongly dependent upon the sensing/actuation mechanism, device design and type of materials used for the fabrication. The radiation-induced degradation of capacitive MEMS devices such as accelerometers, gyros, etc., has been observed to be to be different than that for MEMS devices based on piezoresistive sensing mechanism.

2.10.3 Radiation-induced degradation in piezoresistive sensors

The experimental studies of gamma radiation-induced degradation of piezoresistive pressure sensors are very limited [55], [57]. The radiation-induced degradation of the pressure sensor was observed to be sample dependent. McCready et al. had reported that commercially available piezoresistive pressure transducers (Kulite Semiconductor XTE-190-25A and XCE-062-25A) failed after radiation exposure to 10-100 krad [57]. With their subsequent experiment with pressure transducers (Kulite Semiconductor XTE-190-25A) in a pulsed neutron and gamma radiation, it was demonstrated that the pressure transducers withstood the total neutron fluence of 8.7×10^{15} n/cm² and total gamma dose of 4.4 Mrads (Si). Holbert et al. examined the response of Kulite SOI piezoresistive pressure transducers subjected to a high gamma dose using a ⁶⁰Co source [55]. The transducers were incorporated with a temperature compensation circuit. They had reported a catastrophic failure of a pair of biased Kulite XTE-190-25A pressure transducers at doses of 7.3 and 24.3 Mrad. A pair of transducers irradiated in unbiased mode survived up to 11 Mrad of gamma dose. An output voltage drift with no input pressure, i.e. offset voltage of 1–3% was observed for the total dose of about 20 Mrads [55]. The changes in piezoresistor magnitude were thought to be the cause of this drift. Holbert et al. have demonstrated the degradation in the output response of a bulk micromachined piezoresistive accelerometer and a silicon on insulator (SOI) pressure sensor under high gamma dose [55]. Both sensor types were found to experience similar performance degradation with a drift in offset voltage and a slight change in sensitivity. The drift in offset voltage for all sensors was attributed to the change in resistance of the silicon piezoresistors due to the decrease of the volume for current flow. The ionising radiation-induced generation of oxide and interface trapped hole charges was considered

to create a depletion region surrounding the periphery of the piezoresistors causing reduction of volume for current flow [55]. It has been reported that the radiation-induced displacement damage due to protons can produce a change in resistance of the individual piezoresistor elements of silicon strain gauges [54]. It was primarily ascribed to the effect of charge carrier removal due to charge carrier trapping at induced defects. However, ^{60}Co gamma radiation with energy of about 1 MeV is not expected to cause displacement damage. It has been proposed that gamma radiation cause trapped oxide charges and interface states generation in the silicon dioxide region surrounding the piezoresistors [55]. This results in the formation of a depletion edge around the piezoresistors causing effective area for the current flow to reduce and hence increasing the piezoresistor magnitudes. The increase of piezoresistor magnitude depends on the doping type and concentration, and on the piezoresistor dimensions. The increase in the resistance of piezoresistors is expected to be lower for piezoresistors with larger geometry, higher doping concentration and for n-type doping.

2.10.4 MEMS piezoresistive pressure sensors for high temperatures

Commercially produced piezoresistive pressure sensor has bulk micromachined silicon diaphragm with ion implanted or diffused piezoresistors in a Wheatstone bridge configuration. Due to junction leakage, the operating temperature of the sensors is limited to 125 °C. Several applications of these sensors in industries such as oil, automotive, space, etc demand pressure sensors operating at higher temperatures. Hence, development of pressure sensors for high temperature operation has recently received significant attention. In order to increase the temperature range of operation, several approaches have been reported [58]–[61]. Sensors have been fabricated using wide band gap materials such as SiC or diamond [62]–[64]. However, these technologies are not

compatible with silicon technology and hence the sensors are expensive. The junction leakage problem can be solved by using single crystal silicon or polysilicon piezoresistors which are isolated from the silicon diaphragm using a silicon dioxide layer [65]–[67]. Polysilicon piezoresistor based sensors are less expensive compared to SOI based pressure sensors. However, the sensitivity of polysilicon based pressure sensors is less compared to single crystal silicon based SOI pressure sensor. Fabrication of pressure sensors based on single crystal silicon based piezoresistors using SOI technology has been recently reported [68]. Such sensors have been demonstrated to operate at 350 °C temperatures.

2.11 SUMMARY

A comprehensive literature survey for MEMS technology and pressure sensors based on this technology are discussed in this Chapter. Also, radiation induced effects on the MEMS and pressure sensors are presented in detail from various published literature. In the next Chapter, the simulation study is presented to investigate the mechanical and electrical behaviour of pressure sensors. Based on the results of this study, the design of the pressure sensor was selected to fabricate using MEMS technology.

Chapter 3. DESIGN AND SIMULATION STUDY OF PIEZORESISTIVE PRESSURE SENSORS

3.1 INTRODUCTION

As discussed in the previous Chapter, the response of the piezoresistive pressure sensors is dependent on the generation of stresses in the thin diaphragm due to applied pressure and consecutive changes in the resistance of piezoresistors. In this Chapter, a simulation study is presented to investigate the effect of various design parameters on the response of pressure sensors. Based on the results of this study, the design optimisation of piezoresistive pressure sensors is carried out for diffused piezoresistor and SOI technology based pressure sensors for their fabrication. In addition, the temperature effect on the response of SOI technology based pressure sensors and sensors based on wide bandgap materials is studied using FEM simulations.

3.2 ANALYTICAL MODELLING OF PRESSURE SENSORS

A piezoresistive silicon pressure sensor consists of a thin silicon diaphragm with piezoresistors connected in a Wheatstone bridge configuration to obtain an electrical output. The schematic of a piezoresistive pressure sensor and Wheatstone bridge configuration have been presented in previous Chapter 2. The diaphragm geometrical parameters are selected to maximise the sensitivity without exceeding limits for failure.

3.2.1 A simplified equation for maximum deflection and induced stress

The generated stress and deflection in thin silicon membranes can be modelled using the theory of thin plates [35], [69]. Details of the modelling have been discussed earlier in Chapter 2. Generalised equations to determine maximum deflection and stress of uniform

thick and perfectly clamped thin diaphragm are given in equations (3.1) and (3.2) [33] ,

$$w_{\max} = \alpha \frac{Pa^4}{Eh^3} \quad (3.1)$$

$$\sigma_{\max} = \beta \frac{Pa^2}{h^2} \quad (3.2)$$

Where a is the length of diaphragm edge, E is Young's modulus, h is thickness of diaphragm and P is applied pressure, w_{\max} is a maximum deflection of diaphragm σ_{\max} is maximum stress generated in the diaphragm, α and β are geometrical coefficients.

The geometrical coefficient α and β are dependent on the shape of the diaphragm and for a square diaphragm, geometrical coefficients α and β are 0.0138 and 0.3078 respectively [33]. The maximum deflection occurs at the centre of the diaphragm and maximum stress occurs at the middle of each edge. A square diaphragm has highest induced stress under a particular pressure compared to a circular or a rectangular diaphragm. Hence, this geometry is usually chosen for obtaining maximum sensitivity.

3.2.2 Simplified equations for the change in resistance of piezoresistors

A simplified equation for the change in the resistance of piezoresistors due to the applied pressure is given in equation (3.3). In the case of single crystal silicon, ΔR is a function of silicon crystal orientation, dopant types and concentration. The normalised change in resistance is given by [61],

$$\frac{\Delta R}{R} = \pi_l \sigma_l + \pi_t \sigma_t \quad (3.3)$$

Where, σ_l and σ_t are longitudinal and transverse stresses respectively π_l and π_t are longitudinal and transverse piezoresistive coefficients respectively.

Piezoresistors are aligned in [110] orientation on top of (100) diaphragm. The longitudinal and transverse piezoresistive coefficients are expressed mathematically as $\pi_l = 0.5 \times (\pi_{11} + \pi_{12} + \pi_{44})$ and $\pi_t = 0.5 \times (\pi_{11} + \pi_{12} - \pi_{44})$ respectively [7]. The π_{44} is dominant for p-type piezoresistors in [110] orientation on n-type diaphragm.

3.2.3 Effect of temperature on the change of piezoresistor resistance

The piezoresistor is a function several parameters [70] and expressed as in equation (3.4),

$$\frac{\Delta R}{R} = f(\pi(N, T), \sigma) \quad (3.4)$$

Where, σ is the stress induced in diaphragm and $\pi(N, T)$ is piezoresistance coefficient.

The variation in the piezoresistive coefficients depends on the temperature and doping concentration. A theoretical model for variation in piezoresistive coefficients with dopant concentration and temperature has been earlier presented [71], [72] and is given as in equation (3.5),

$$\pi(N, T) = P(N, T)\pi^{ref} \quad (3.5)$$

Where, π^{ref} is piezoresistive coefficient at 27 °C for lightly doped material (dopant concentration of 10^{16} cm^{-3}) and P (N, T) is a piezoresistive factor indicating the dependence on temperature and concentration of dopant [71].

All piezoresistive coefficients, (π_{11} , π_{12} and π_{44}) can be scaled linearly using a piezoresistive factor ($P(N, T)$). The conductivity of the doped region of piezoresistors is dependent on several parameters as given as in equation (3.6) [73],

$$\sigma(x, T) = qn(x)\mu_p(n(x), T) \quad (3.6)$$

Where, q is charge of the free carrier, $n(x)$ is concentration at various depths of piezoresistive layer realised by implantation/diffusion for p-type piezoresistors and $\mu_p(n(x), T)$ is the mobility (dependent on temperature and doping of p-type resistors).

Assuming a uniformly doped piezoresistive layer given as in equation (3.7),

$$\sigma(T) = qN\mu_p(N, T) \quad (3.7)$$

In order to obtain Wheatstone bridge output response of a pressure sensor at different temperatures and doping concentrations, a variation of mobility and piezoresistive coefficient has been taken into account as per equations 3.5 to 3.7 during simulations.

3.2.4 Calculation of the sensitivity of a pressure sensor

The sensitivity of the pressure sensor is defined as the slope of the output response plot with respect to the applied pressure given as in equation (3.8) [35].

$$S_p = \frac{\Delta V_o}{\Delta P} \frac{1}{V_{in}} \quad (3.8)$$

Where, S is sensitivity, V_{in} is input voltage, ΔV_o output voltage change, ΔP is pressure.

3.2.5 Nonlinearity calculation

Nonlinearity is the deviation of the actual response, i.e. calibration curve from the expected linear response of the pressure sensor, as the output signal does not vary linearly with input pressure. The non-linearity error at a specific calibration point is mathematically represented as in equation (3.9) [35],

$$NL_i = \frac{V_o(P_i) - \frac{V_o(P_m)}{P_m} P_i}{V_o(P_m)} \times 100\% \quad (3.9)$$

Where, NL_i is percentage nonlinearity, $V_0(P_i)$ is instantaneous output voltage at and applied pressure P_i , $V_0(P_m)$ is the output voltage at maximum applied pressure P_m .

In the present work, the FEM simulations have been carried out to study the effect of various design parameters on the pressure response. In the next section, the process of modelling using the FEM simulator is described.

3.3 METHODOLOGY AND MATERIAL PROPERTIES

The design optimisation of the pressure sensor is carried out using a commercially available FEM tool used for parameter optimisation of MEMS devices. The generation of a 3D model for simulation process includes; i) defining of the material properties, ii) assigning the fabrication sequence of the device, and iii) incorporating the 2 D layout of the design. The dominant material properties of silicon are listed in Table 3.1.

Table 3.1:Material properties of silicon [74].

Properties		Silicon
Elastic Constant (MPa)		1.30×10^5
Poisson's Ratio		2.78×10^{-1}
Density (kg/ μm^3)		2.33×10^{-15}
TCE Integral Form(1/K)		2.49×10^{-6}
Thermal Conductivity (pW/ $\mu\text{m K}$)		1.57×10^8
Specific Heat (pJ/kg K)		7.03×10^{14}
Electrical Conductivity (pS/ μm)		1.40×10^9
	$\pi_{11=}$	6.60×10^{-5}
Piezoresistive Coefficient (1/MPa)	$\pi_{12=}$	-1.10×10^{-5}
	$\pi_{44=}$	1.38×10^{-3}

Generally, for bulk micromachined pressure sensors, a square diaphragm is created using KOH/TMAH/EDP etching of the bulk silicon material. Silicon is one of the best material

for mechanical structures because it exhibits properties similar to steel [10]. The mechanical analysis has been performed using FEM tool and the data is exported for further analysis. The electrical response of the piezoresistive pressure sensor is calculated by piezoresistive coefficients which are well defined for crystalline silicon in literature.

3.3.1 Steps to build a 3D model

The methodology used for the simulation study is described stepwise in the current section. During the simulation process, it is required to provide inputs parameters for material properties, process flow and 2D layout. Based on these three inputs, the solid model is created. Furthermore, solid model is meshed in the finite elements for analysis purpose. The analysis tool is a multi-physics tool to analyse the design in various domains. Generally, solid models are created using the material database present in the tool. However, material properties can also be defined by the user as per requirements. The steps used to build a solid model are given in Figure 3.1(a), (b), and (c). The 3D model of anisotropically etched silicon diaphragm and meshed structure are as shown in Figure 3.1 (d) and (e) respectively. A mapped brick mesh with fine element size (i.e. 25 μm) for the diaphragm and course element size (i.e. 100 μm) for the bulk silicon material are created for carrying out simulations.

The pressure sensor design in the present work was targeted for 20 MPa full-scale operation. Considering a safety margin of a factor of 2, the design was targeted for a maximum pressure of 40 MPa. The dimensions of the diaphragm were varied to optimise the geometrical parameters i.e. edge length and thickness of the diaphragm. Subsequent to the optimisation of diaphragm parameters, stress concentration regions for locating piezoresistors over the diaphragm were identified. The Wheatstone bridge output

response was obtained for different pressures and temperatures for a particular doping concentration of piezoresistors. Variation of mobility and piezoresistive coefficient with temperature were considered for study of temperature induce effect on pressure response.

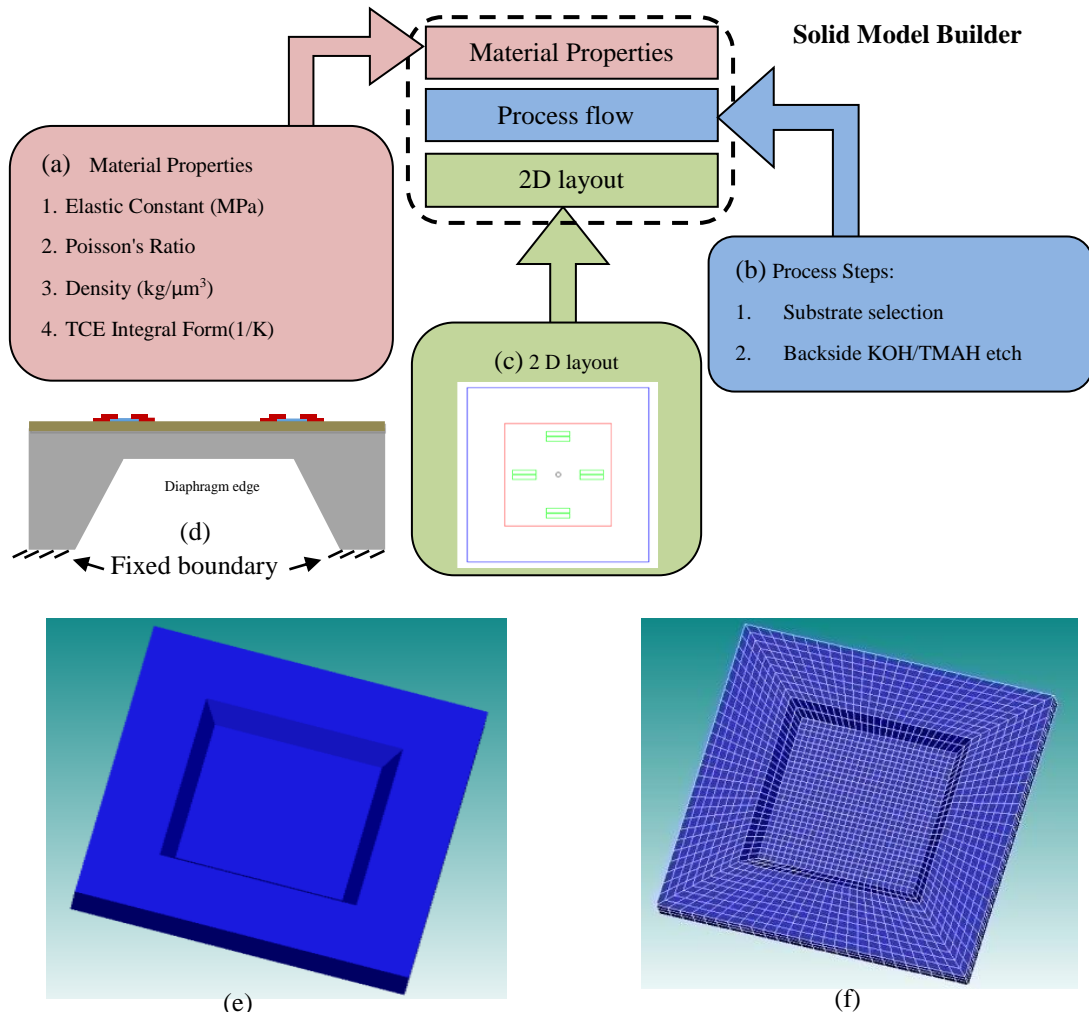


Figure 3.1: Simulation to build solid model (a) material property selection, (b) Process definition, (c) 2D layout, (d) Fixed boundary condition (e) 3D solid model, and (f) 3D meshed model.

3.3.2 Effect of diaphragm shape on the mechanical response

The fabrication processes used for the fabrication of silicon diaphragms i.e. DRIE or bulk micromachining results in shapes of the diaphragms, which are different than thin plates. Hence, initially, different various possible diaphragm shapes were analysed using FEM simulations. The mechanical responses of diaphragm structures were studied to estimate

the effect of diaphragm shape on the mechanical response of the pressure sensor. The solid and meshed models of these structures with fixed boundaries for an ideal case are depicted in Figure 3.2 for i) a conventional thin plate, ii) DRIE etched diaphragm with straight edges and iii) anisotropically etched diaphragm using TMAH/KOH etch.

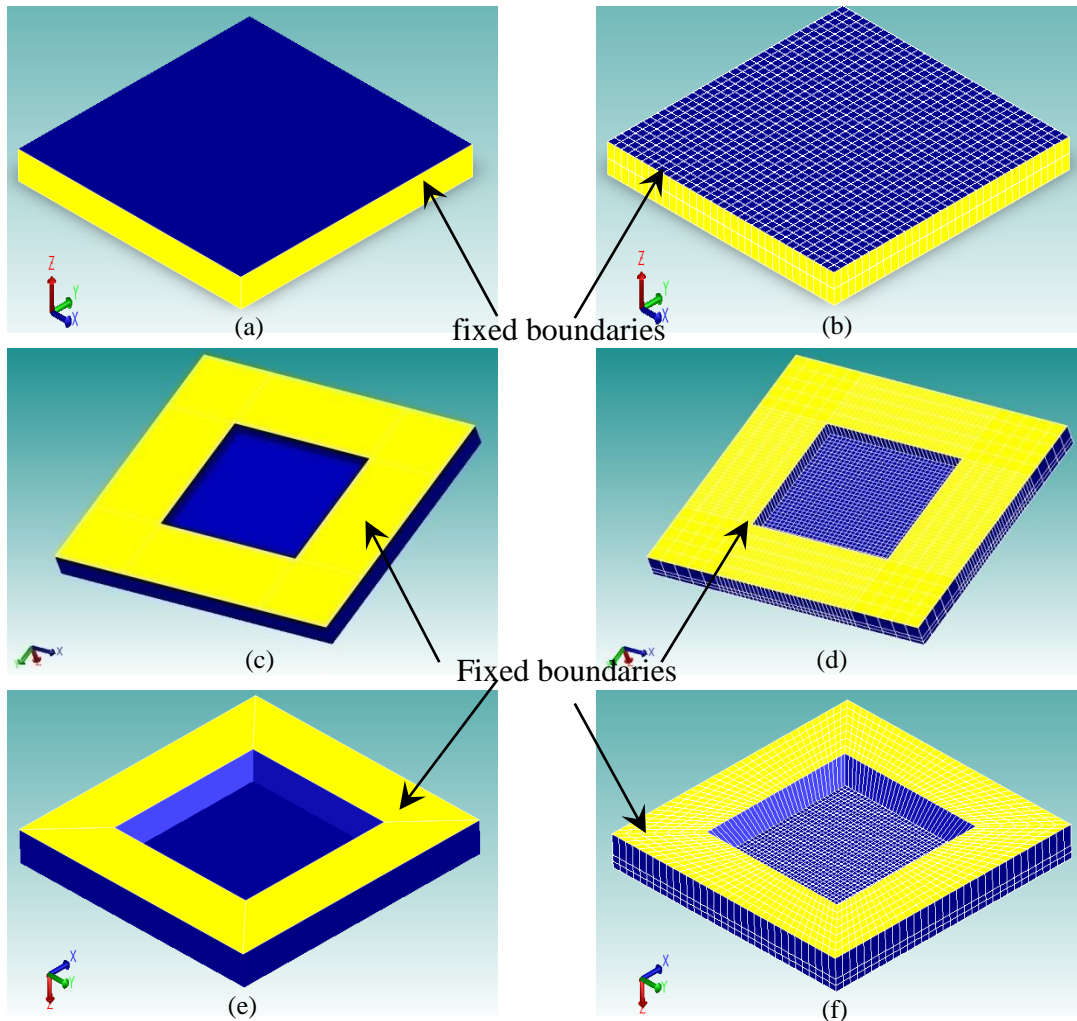


Figure 3.2: Simulations for i) Model of plate (a) solid model, (b) mesh model, ii) DRIE etched diaphragm (c) Solid model, (d) Mesh model, iii) Anisotropically etched diaphragm (e) Solid model (f) Mesh model; diaphragm size $2000\ \mu\text{m} \times 2000\ \mu\text{m} \times 150\ \mu\text{m}$. The yellow color regions are depicted as fixed boundary conditions.

The mechanical responses in terms of displacement and von Mises stress are depicted in Figure 3.3 (a) and (b) respectively for these diaphragm shapes. It is observed that depending on the fabrication process used, the mechanical response of the diaphragms of different shapes is different due to the differences in the side walls. A quantitative

comparison of the deflection sensitivity and stress sensitivity for these structures is listed in Table 3.2. The sensitivity is higher for KOH/TMAH etched thin diaphragm due to differences in the structure at the edges (i.e. edges are sloped at 54.7° for KOH/TMAH etched, at 90° for DRIE etched diaphragm) which resulted in differences in the stresses generated at the edges. The use of KOH/TMAH etch diaphragm structure is more common due to simple fabrication process. Hence, further analysis was carried out using anisotropically etched diaphragms.

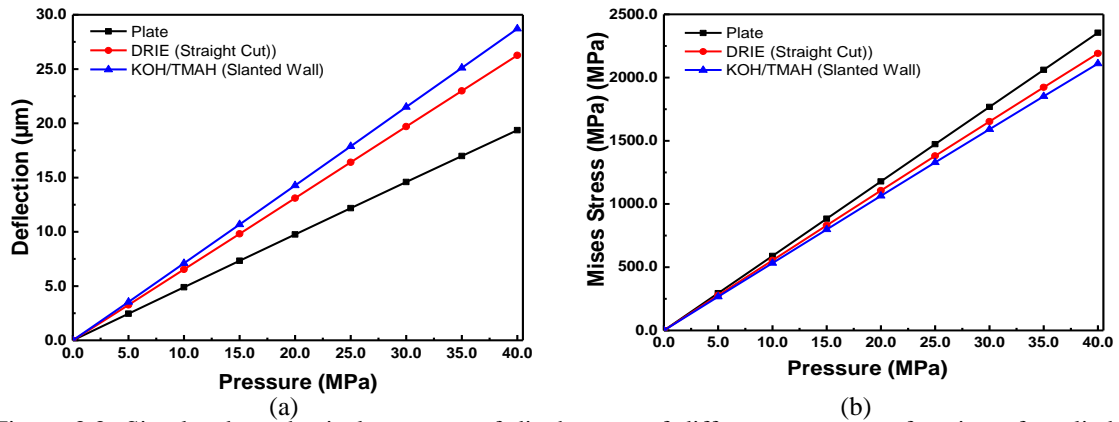


Figure 3.3: Simulated mechanical response of diaphragms of different types as a function of applied pressure; (a) Deflection (b) von Mises stress, diaphragm size $2000 \mu\text{m} \times 2000 \mu\text{m} \times 150 \mu\text{m}$.

Table 3.2: Stress and deflection sensitivities of the various diaphragm structures, analysed using mapped brick mesh with parabolic hex element with 27 nodes.

Diaphragm type	Stress Sensitivity (MPa/MPa)	Deflection Sensitivity ($\mu\text{m}/\text{MPa}$)	Number of nodes	Number of elements	Volume of geometry
Plate	58.87	0.487	22445	2178	$6.0 \times 10^8 \mu\text{m}^3$
DRIE (Straight Cut)	54.76	0.655	44533	4458	$5.4 \times 10^9 \mu\text{m}^3$
KOH/TMAH (Slanted)	52.77	0.720	48845	4950	$5.2 \times 10^9 \mu\text{m}^3$

3.3.3 Effect of diaphragm geometry on mechanical response

The thin diaphragms with different geometrical parameters as given below were analysed in order to understand the effect of diaphragm geometrical parameters on the induced stress and deflection:

- (i) The edge length of $2000 \mu\text{m}$, $1500 \mu\text{m}$, $1000 \mu\text{m}$ and $750 \mu\text{m}$
- (ii) Variation in diaphragm thickness from $25 \mu\text{m}$ to $400 \mu\text{m}$

Typical deflection and von Mises stress contours obtained through simulations are depicted in Figure 3.4 (a) and (b) respectively. As expected, the maximum deflection occurs in the centre and maximum stress regions are located in the centre of four edges, close to the fixed edges. The maximum deflection and maximum von Mises stress obtained for 40 MPa applied pressure are $1.6 \mu\text{m}$ and 3.6 MPa respectively for the diaphragm size of $1000 \mu\text{m} \times 1000 \mu\text{m} \times 200 \mu\text{m}$. The stress contours in X and Y directions (i.e. σ_{xx} and σ_{yy}) are shown in Figure 3.5(a) and (b) respectively. For best sensitivity, the piezoresistors are located in the high-stress concentration regions.

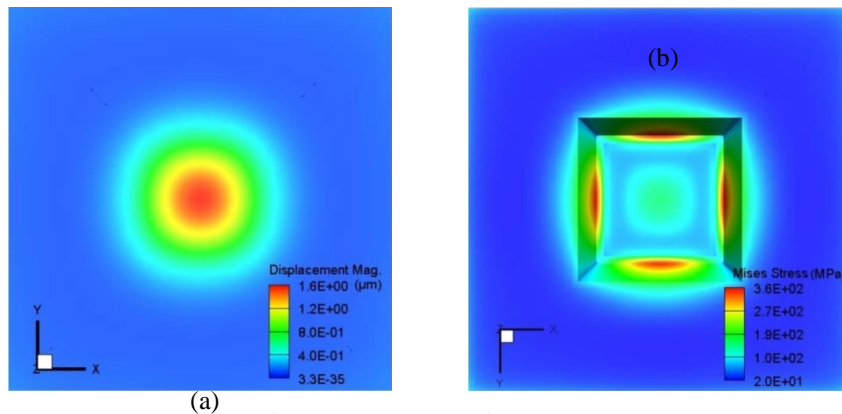


Figure 3.4: Contour plots for the diaphragm of size $1000 \mu\text{m} \times 1000 \mu\text{m} \times 200 \mu\text{m}$ for applied pressure 40 MPa; (a) Deflection, (b) von Mises stress.

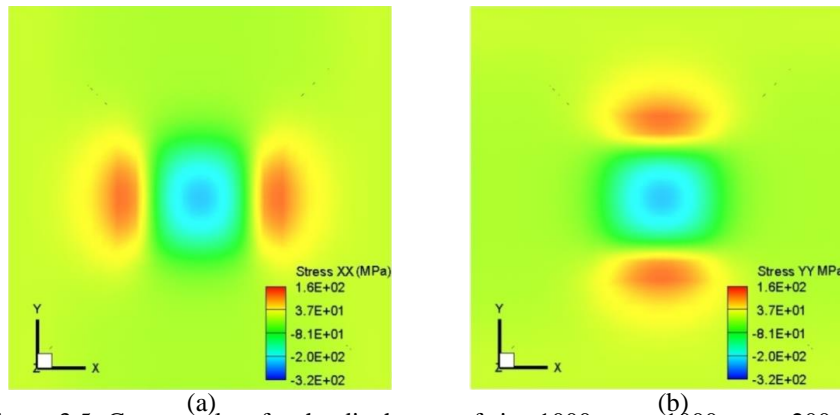


Figure 3.5: Contour plots for the diaphragm of size $1000 \mu\text{m} \times 1000 \mu\text{m} \times 200 \mu\text{m}$ for the applied pressure of 40 MPa; (a) Stress XX, and (b) Stress YY.

The parametric simulation was carried out by varying diaphragm thickness and edge length of the diaphragm in order to study their effect on the deflection and generated stresses. The results obtained from the simulations for maximum deflection and induced

stresses are summarised in Figure 3.6 (a), (b) and Figure 3.7 (a), (b) respectively. The thin plate theory considers ‘plate’ as a structure with lateral dimensions of the plate much larger than the thickness of the plate [69], [70]. The thin plate theory takes advantage of this disparity in dimensions of the plate to simplify the three-dimensional solid mechanics problem to a two-dimensional problem. Also, it is required that the sensors should withstand at least five times the full scale pressure. Hence the limiting values for the maximum deflection of 20 % of the diaphragm thickness and maximum induced stresses 10 % of the yield strength were adopted considering the constraints for validation of thin plate theory and safety margins for the operation of the sensor.

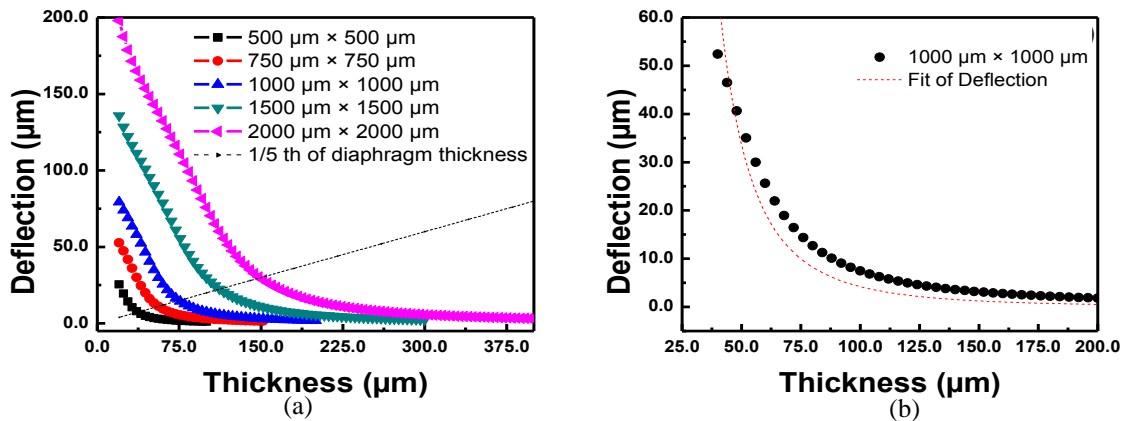


Figure 3.6: (a) Maximum deflection vs thickness of diaphragm for varying edge lengths of the diaphragm under applied pressure 40 MPa, (b) Validation of deflection variation for diaphragm size of 1000 μm × 1000 μm, under applied pressure 40 MPa.

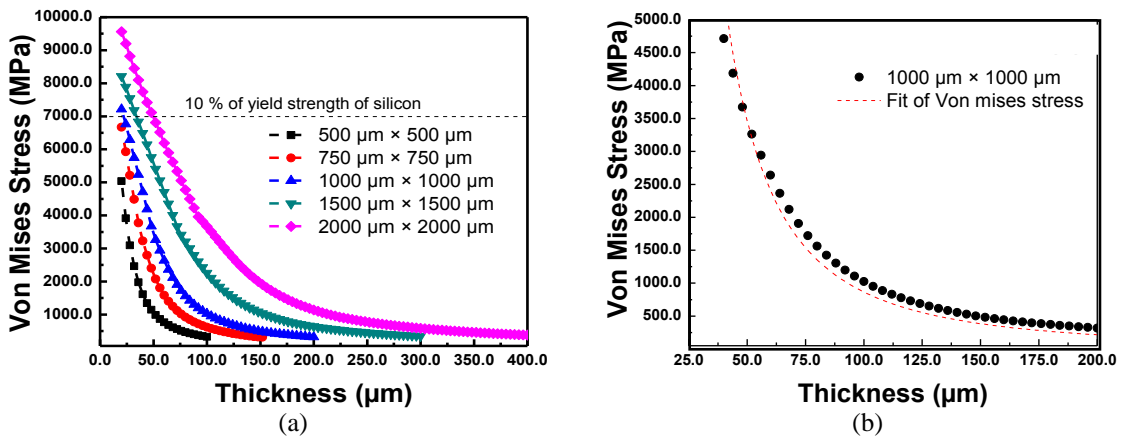


Figure 3.7: (a) Maximum von Mises stress vs thickness of diaphragm for varying edge lengths of the diaphragm under applied pressure 40 MPa, (b) Validation of von Mises stress for diaphragm size of 1000 μm × 1000 μm, under applied pressure 40 MPa.

As anticipated from equation (3.1) and (3.2), the deflection and stresses increase with the increase of diaphragm size and with the decrease in diaphragm thickness. In order to validate the simulation results, the maximum deflection data for diaphragm size of $1000 \mu\text{m} \times 1000 \mu\text{m}$ with different thicknesses (Figure 3.6 (b)) is fitted with a polynomial. As expected, the maximum deflection shows the dependence of h^3 . Similarly, the maximum stress shows the dependence of h^2 (Figure 3.7(b)) with diaphragm thickness. The effect of applied pressure for different edge lengths of the diaphragm on the maximum deflection and induced stress are depicted in Figure 3.8 (a) and (b) respectively for $150 \mu\text{m}$ diaphragm thickness. The effect on the deflection sensitivity and induced stress sensitivity due to the change in edge length of diaphragm is presented in Table 3.3.

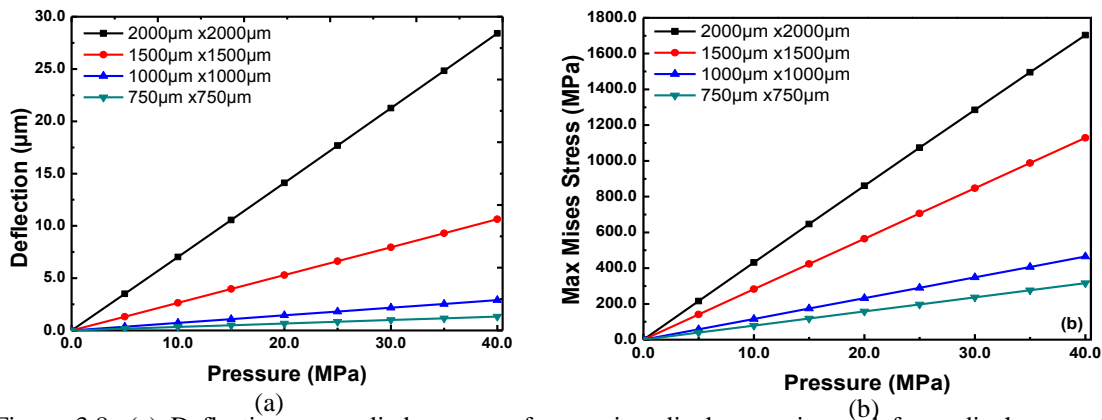


Figure 3.8: (a) Deflection vs applied pressure for varying diaphragm size and for a diaphragm of thickness of $150 \mu\text{m}$, (b) von Mises stress vs applied pressure for varying diaphragm size and for a diaphragm thickness $150 \mu\text{m}$.

Table 3.3: Stress and deflection sensitivities for the diaphragms with different edge lengths and a thickness of $150 \mu\text{m}$.

Diaphragm type	Stress Sensitivity (MPa/MPa)	Deflection Sensitivity ($\mu\text{m}/\text{MPa}$)
$2000 \mu\text{m} \times 2000 \mu\text{m}$	42.52	0.710
$1500 \mu\text{m} \times 1500 \mu\text{m}$	28.16	0.260
$1000 \mu\text{m} \times 1000 \mu\text{m}$	11.51	0.070
$750 \mu\text{m} \times 750 \mu\text{m}$	7.67	0.032

The diaphragm deflection and von Mises stress variation at the surface of the diaphragm along a horizontal line (i.e. X-axis) through the centre for different thickness is presented

in Figure 3.9 (a) and (b) respectively. The deflection is observed to be maximum at the centre and minimum at the edge of the diaphragm. Whereas, maximum induced stresses are observed close to the diaphragm at the centre of diaphragm edge. As expected, the deflection and stresses increases with reducing the diaphragm thickness. Similarly, variation of stress components along X and Y direction is plotted in Figure 3.10 (a) and (b) respectively. For stress in X-axis direction, the maximum tensile stress region is located near the diaphragm edge and maximum compressive stress region is located in the centre. The sensitivity of the pressure sensor depends on the resultant stress as shown in Figure 3.11. From resultant stress data plotted in Figure 3.11, the piezoresistor location is identified as 30 μm offset from the edge of diaphragm ($1000 \mu\text{m} \times 1000 \mu\text{m} \times t \mu\text{m}$, where, t is 100 to 200 μm) for maximizing the sensitivity of pressure sensor. Simulation study shows that depending on the thickness, the maximum stress region is not always at the edge, but some distance away depending on the thickness. This is probably due to the sloping walls of the diaphragm where the thickness increases gradually away from the diaphragm edge. Hence, the location of piezoresistor is changed accordingly.

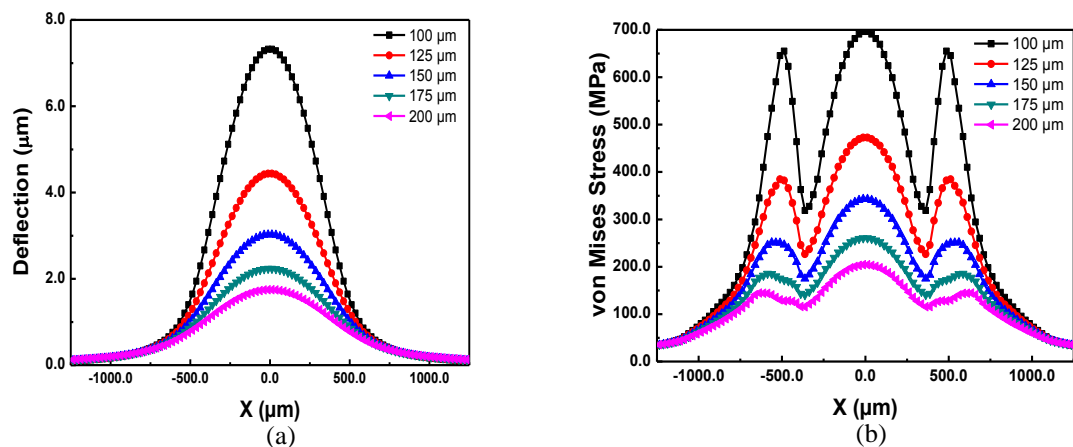


Figure 3.9: (a) Deflection profile, and (b) von Mises stress for diaphragm size of $1000 \mu\text{m} \times 1000 \mu\text{m}$ for different diaphragm thicknesses; applied pressure is 40 MPa.

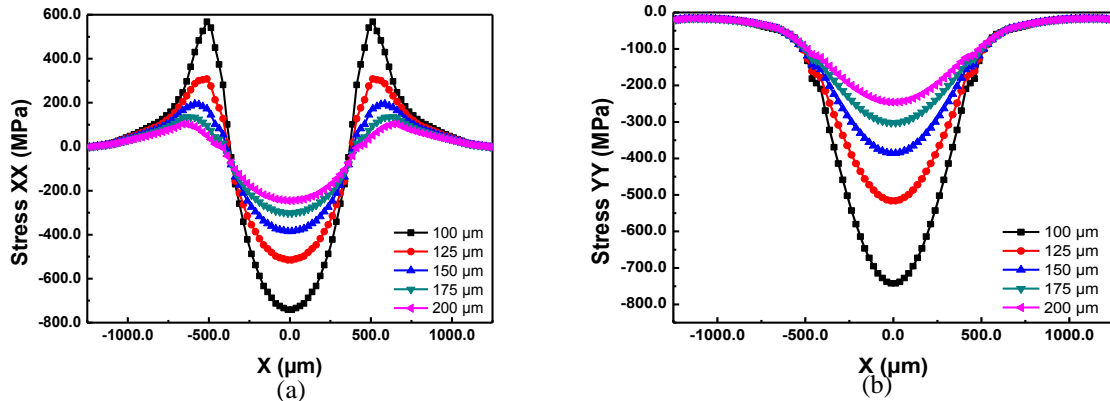


Figure 3.10: (a) Stress XX Profile, and (b) Stress YY profile along the centre of the diaphragm for diaphragm size of $1000 \mu\text{m} \times 1000 \mu\text{m}$ with different diaphragm thicknesses; applied pressure is 40 MPa.

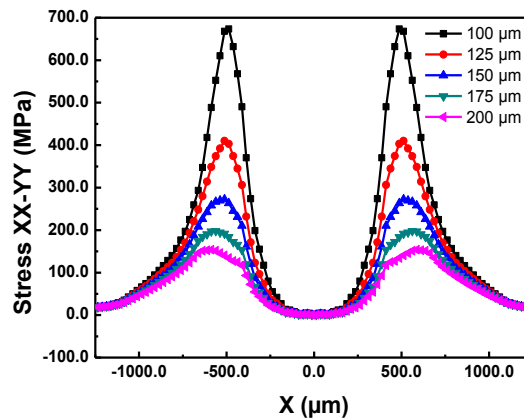


Figure 3.11: Resultant stress profile along the centre of the diaphragm for diaphragm size of $1000 \mu\text{m} \times 1000 \mu\text{m}$ with different diaphragm thicknesses; applied pressure is 40 MPa.

3.3.4 Identification of the location of piezoresistors for maximum sensitivity

The location of the piezoresistors on top of the thin diaphragm is decided based on high-stress concentration region. The maximum change in the current is observed near the middle of diaphragm edge for longitudinal and transverse resistance (Figure 3.12). These piezoresistors were connected in the Wheatstone bridge configuration to get an electrical output under applied pressure. The optimised location was finalised based on the magnitude of maximum change in the current for piezoresistors. The schematic for location of piezoresistors on diaphragm is depicted in Figure 3.13.

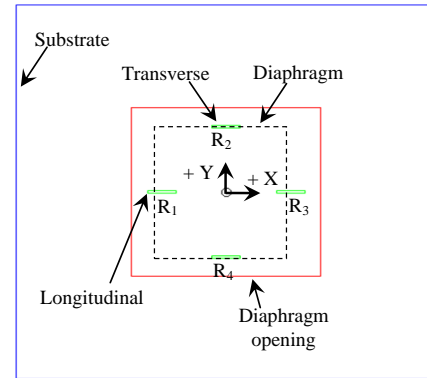
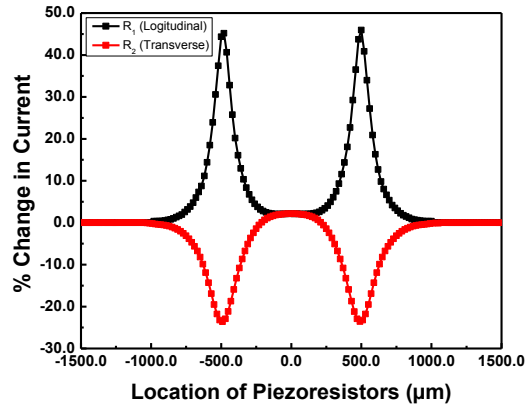


Figure 3.12: Identifying the location of the maximum change in the resistance for the diaphragm size $1000 \mu\text{m} \times 1000 \mu\text{m} \times 150 \mu\text{m}$.

Figure 3.13: Placement of the piezoresistors on the top of the diaphragm.

To identify location of piezoresistors, a parametric simulation was carried out by varying the location of the piezoresistor over the diaphragm. The longitudinal piezoresistor, R_1 , was moved from $-X$ to $+X$ and transverse piezoresistor, R_2 , was moved from $-Y$ to $+Y$ axis on top of the diaphragm.

3.3.5 Analysis of pressure sensor response and nonlinearity

Subsequent to the location identification of piezoresistors, the output voltage of the Wheatstone bridge was obtained through simulations for a piezoresistor doping concentration of $1 \times 10^{19} \text{ cm}^{-3}$. The output voltage for pressure up to 40 MPa is plotted for three diaphragm thicknesses of $100 \mu\text{m}$, $150 \mu\text{m}$ and $200 \mu\text{m}$ (Figure 3.14 (a)). As expected, the pressure response with a thinner diaphragm shows higher sensitivity compared to that observed for thicker diaphragm (Figure 3.14(b)).

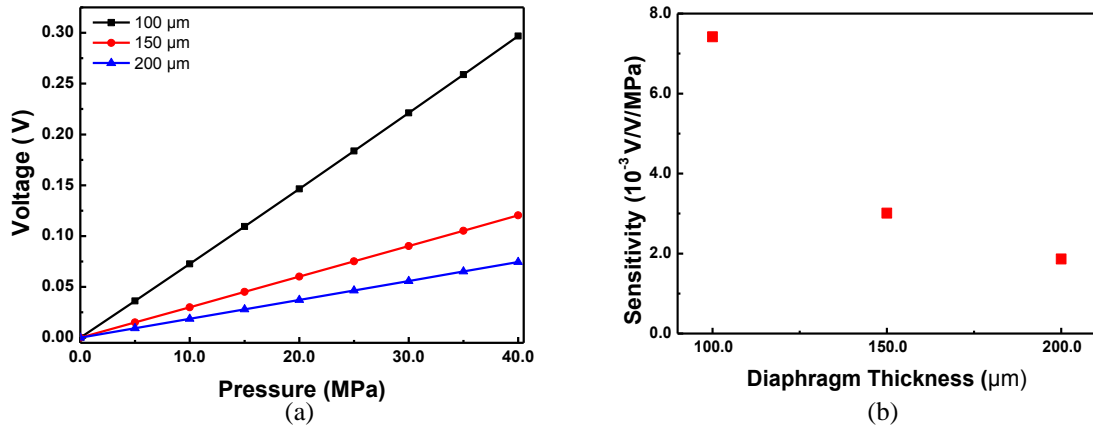


Figure 3.14: (a) Output voltage of the Wheatstone bridge for different diaphragm thicknesses, diaphragm size $1000 \mu\text{m} \times 1000 \mu\text{m}$, (b) Sensitivity vs thickness of diaphragm for pressure sensor (diaphragm: $1000 \mu\text{m} \times 1000 \mu\text{m} \times 200 \mu\text{m}$, Piezoresistor concentration $1 \times 10^{19} \text{cm}^{-3}$).

Since, there is a trade-off between sensitivity and nonlinearity, the percentage nonlinearity for pressure sensors with these three diaphragm thicknesses was obtained. The % nonlinearity analysis was carried out for $1000 \mu\text{m} \times 1000 \mu\text{m}$ diaphragm dimensions with varying thickness. It is observed that % non-linearity for a thicker diaphragm (i.e. $200 \mu\text{m}$) is least as compared to a thinner diaphragm (Figure 3.15).

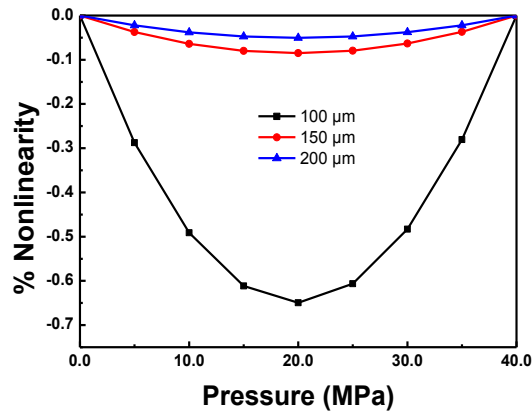


Figure 3.15: The % nonlinearity of pressure sensor using diaphragm size $1000 \mu\text{m} \times 1000 \mu\text{m}$ with varying thickness.

Hence, for better linearity, diaphragm thickness of $200 \mu\text{m}$ was chosen for further analysis with temperature dependence of the output response for pressure sensor. The simulation of pressure sensor response carried out for studying the effect of the concentration of piezoresistors shows that the output response decreases with the increase

in the doping concentration of piezoresistors due to the decrease in piezoresistive coefficient (Figure 3.16 (a) and (b)).

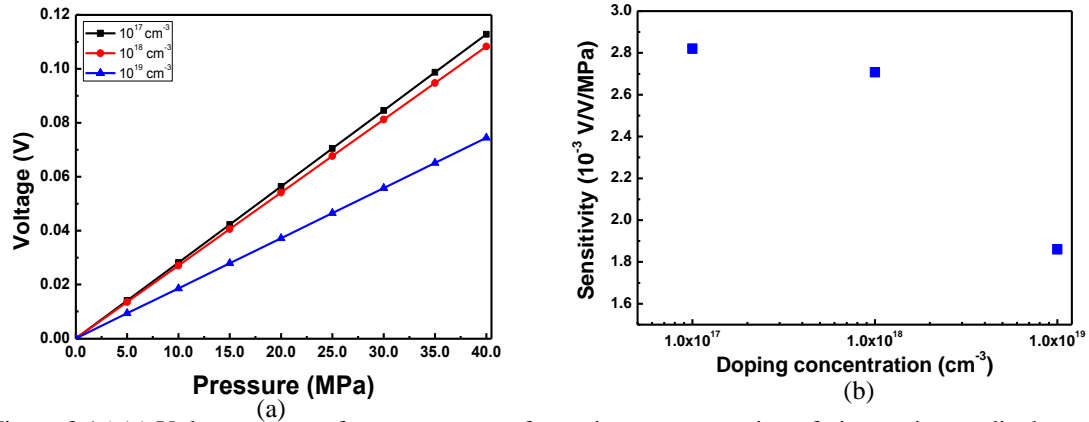


Figure 3.16:(a) Voltage output of pressure sensor for various concentration of piezoresistors, diaphragm size – $1000 \mu\text{m} \times 1000 \mu\text{m} \times 200 \mu\text{m}$, (b) Sensitivity as a function of doping concentration.

3.3.6 Quantitative analysis of temperature dependence of pressure sensor response

Subsequent to finalisation of pressure sensor design parameters, simulations were carried out to analyse the change of Wheatstone bridge output response with temperature. It was assumed that the resistors are electrically isolated by a thin silicon dioxide layer from the micromachined diaphragm and hence the problem of junction leakage at higher temperature is avoided. As discussed in the later Chapters, this was implemented using SOI wafer based fabrication process. As discussed in Section 3.2.3, for this analysis, i) the change of conductivity of boron doped piezoresistors due to mobility variation with temperature and ii) change of piezoresistive coefficient with temperature, were both provided as input parameters to the simulator. Due to mobility variation, the resistance of piezoresistors is observed to increase from $3.43 \text{ k}\Omega$ at $25 \text{ }^\circ\text{C}$ to $3.93 \text{ k}\Omega$ at $200 \text{ }^\circ\text{C}$. The results of the analysis of pressure sensor response up to 40 MPa pressure are summarised in Figure 3.17 (a) and (b) for different temperatures in the range of $25 \text{ }^\circ\text{C}$ to $200 \text{ }^\circ\text{C}$. As expected, the output response of pressure sensor gradually decreases with increase in the

temperature. From the data plotted in Figure 3.17 (a), the decrease of sensitivity obtained for various temperatures is shown in Figure 3.17 (b).

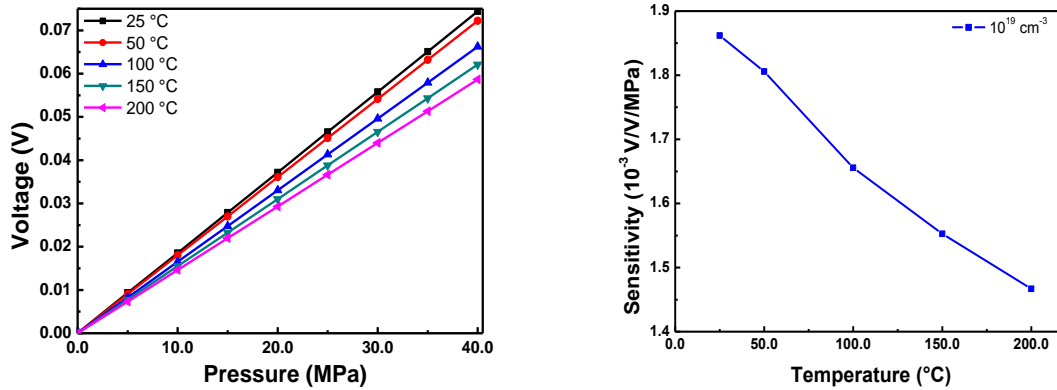


Figure 3.17:(a) The voltage output of pressure sensor with varying temperatures for diaphragm size of $1000 \mu\text{m} \times 1000 \mu\text{m} \times 200 \mu\text{m}$, piezoresistor doping $1 \times 10^{19} \text{cm}^{-3}$, (b) Sensitivity of pressure sensor at different temperatures, diaphragm size $1000 \mu\text{m} \times 1000 \mu\text{m} \times 200 \mu\text{m}$, piezoresistor doping $1 \times 10^{19} \text{cm}^{-3}$.

Compared to the output voltage at $25 \text{ }^\circ\text{C}$, the pressure sensor with diaphragm of thickness $200 \mu\text{m}$ shows a decrease of output voltage at $200 \text{ }^\circ\text{C}$ to $1.57 \times 10^{-2} \text{ V}$. Similarly, the pressure sensor with $100 \mu\text{m}$ thick diaphragm shows the output voltage decrease of $6.32 \times 10^{-2} \text{ V}$. The output at 40 MPa is observed to decrease by 21.16% at $200 \text{ }^\circ\text{C}$ compared to the output at $25 \text{ }^\circ\text{C}$. However, the percentage change with respect to output voltage at $25 \text{ }^\circ\text{C}$ is the same for diaphragms of both thicknesses. The temperature effect on the output response has been plotted for the diaphragms of different thicknesses in Figure 3.18. The results of simulations as summarised in Figure 3.17 ((a) and (b)) and Figure 3.18 give a quantitative estimation of temperature response variation of SOI based piezoresistive pressure sensor in the range of $25 \text{ }^\circ\text{C}$ to $200 \text{ }^\circ\text{C}$ for different diaphragm thicknesses at 40 MPa . Though the piezoresistors have a high doping concentration of $1 \times 10^{19} \text{cm}^{-3}$, the response at $200 \text{ }^\circ\text{C}$ significantly decreases compared to the response at $25 \text{ }^\circ\text{C}$ and the decrease of response is observed to be about 21% . The observed decrease in the pressure response could be attributed to the decrease in the piezoresistive coefficient

with temperature. Hence, a suitable temperature compensation technique needs to be adopted for reducing the temperature sensitivity of pressure sensor.

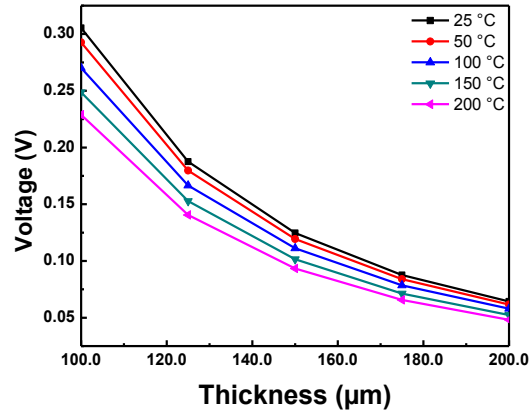


Figure 3.18: Voltage output of the pressure sensor at 40 MPa pressure for different temperatures and diaphragm thicknesses, diaphragm size - $1000 \mu\text{m} \times 1000 \mu\text{m}$, piezoresistor doping - $1 \times 10^{19} \text{cm}^{-3}$.

3.4 SELECTION OF DESIGN PARAMETERS FOR THE PIEZORESISTIVE PRESSURE SENSORS

3.4.1 Selected parameters for diffused/ion implanted piezoresistor based pressure sensors

The schematic of the placement of piezoresistors on the top of thin diaphragm is presented for piezoresistive pressure sensors for 100 bar and 200 bar operation (Figure 3.19). The optimised dimensions of the diaphragm are presented in Table 3.4. In order to accommodate half scale pressure range i.e. 100 bar in the same wafer, the length of diaphragm edge was increased to produce two pressure range devices in the single fabrication processes. The diaphragm dimensions are listed in Table 3.5.

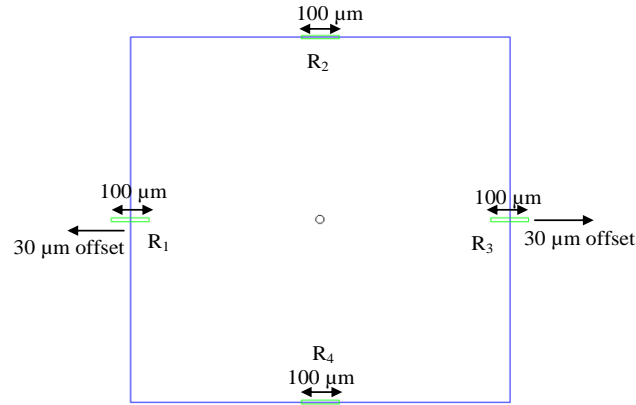


Figure 3.19: Location of the piezoresistors on top of the square diaphragm.

Table 3.4: Selected dimensions of diffused pressure sensor for 20 MPa pressure range.

Pressure (bar)	Diaphragm ($\mu\text{m} \times \mu\text{m}$)	Thickness (μm)	Resistors Position		Expected sensitivity (mV/V/bar)
			for R_1, R_3 (μm)	for R_2, R_4 (μm)	
200	1000 × 1000	200	30	30	0.182
	750 × 750	150			0.180

Table 3.5 : Diaphragm dimension for half of pressure range pressures sensor for 10 MPa pressure.

Pressure (bar)	Diaphragm ($\mu\text{m} \times \mu\text{m}$)	Thickness (μm)	Resistors Position		Expected sensitivity (mV/V/bar)
			for R_1, R_3 (μm)	for R_2, R_4 (μm)	
100	1414 × 1414	200	30	0	0.382
	1060 × 1060	150			0.362

3.4.2 Selected parameters for SOI wafer based pressure sensors

It was assumed that the thin buried oxide does not cause changes in the stress distribution at the surface. In one case, the piezoresistors were diffused in silicon. In the other case, the silicon piezoresistors were patterned over a silicon dioxide insulating layer. The diaphragm geometry, location of piezoresistors were the same.

3.5 COMPARATIVE STUDY OF PRESSURE SENSOR BASED ON WIDE BANDGAP MATERIALS

The diffused/ion-implanted silicon based sensors have limitation of operating temperature range up to 125 °C. There is a keen interest to investigate suitability of alternative materials for operation of pressure sensors beyond this temperature limitation. Wide bandgap materials such as diamond or SiC are considered suitable for high temperature applications. In this section, a quantitative analysis of piezoresistive pressure sensors based on wide bandgap materials is presented using FEM simulations.

3.5.1 Use of silicon as a material for MEMS

In general, silicon is the material of choice for fabrication of Microelectromechanical Systems (MEMS) because it utilizes well-established IC fabrication technology along with silicon micromachining. Silicon is commonly used as piezoresistive sensing application in order to fabricate sensors because of silicon exhibits piezoresistivity with high gauge factor. Moreover, it is also utilised as micromechanical structure due to its excellent mechanical properties. However, degradation in the performance of electrical behaviour of silicon based piezoresistive pressure sensors are observed beyond 125 °C. It is because of excessive reverse current in the junction isolation of the piezoresistors that is caused by thermal generation of carriers. The variation of piezoresistive coefficients of silicon with doping and temperature was well studied and reported in the literature [71], [72]. High temperature operating conditions are present in wide applications areas in automotive, avionics & aerospace, defence, process control, and oil & gas industries, nuclear power plant, etc. A conventional silicon piezoresistive sensor fabrication process is adopted by using a smart-cut SOI process or using polycrystalline silicon piezoresistors

isolated from the silicon diaphragm by an insulating SiO₂ layer [1], [65]–[67], [75], [76]. Therefore, internationally, the research is being carried out to enhance the operating temperature range of piezoresistive pressure sensors using alternate materials for MEMS fabrication. In the present work, a quantitative analysis is carried out for the response of pressure sensors based on wide bandgap materials.

3.5.2 Use of wide bandgap material as alternative piezoresistive materials

The fabrication processes based on wide bandgap semiconductor materials, i.e. silicon carbide (SiC), diamond and group III-nitrides are proposed to further increase the operating temperature range of MEMS [64], [77]–[79]. The main property of the wide bandgap materials is higher bandgap than silicon, which enables much higher operating temperatures. The bandgap of the silicon, silicon carbide, diamond and gallium nitride are 1.1 eV, 3.3 eV, 5.5 eV and 3.4 eV respectively. The properties of these materials are discussed briefly in the next subsections.

3.5.2.1 Silicon carbide

The silicon carbide is used as a piezoresistive material in various adverse sensing applications due to its superior material properties. The main properties are in terms of high Young's modulus (424 GPa), high operating temperature range up to 1800 °C, high thermal conductivity 500 W/mK and highly chemical inertness [80]. In addition, the single crystal SiC has a wide bandgap (2.39–3.33 eV) as compared to single crystal silicon (1.12 eV). Pioneering works have been reported by Mehrengany and Howe for the development of SiC based MEMS for high temperature and harsh environmental applications [81]–[84]. Silicon carbide can be deposited on silicon substrates in monocrystalline, polycrystalline and amorphous forms [85]. Doped single or

polycrystalline SiC films can be realised over silicon dioxide using processes such as low-pressure chemical vapour deposition (LPCVD), single crystal smart cut process and epitaxial process [82], [86]–[88]. Generally, the piezoresistive coefficient of SiC is lower as compared to silicon. Hence, the sensitivity of such devices is less. However, its suitability in high temperature makes it a prominent candidate for the piezoresistive sensing applications. The gauge factor of n-type 3C-SiC decreases by approximately 50% at temperatures from room temperature to above 400 °C and is in the range of 5-18 at 450 °C which makes it suitable for high-temperature applications [64]. Studies of variation of the gauge factor of SiC based pressure sensors have been carried out for temperatures up to 400 °C and observed the degradation in its performance [88]. The gauge factor of the silicon carbide polytypes is presented and compared with silicon in Figure 3.20.

3.5.2.2 Diamond

Considering the potential of polycrystalline diamond for high-temperature harsh environment MEMS applications, experimental studies of boron doped diamond piezoresistors and membranes have been carried out for pressure sensor [78], [89]–[91]. The gauge factor of diamond is random and varied in wide range. Gauge factor is dependent on process technology and various parameters such as type of doping, size of crystal, orientation, etc. For boron doped polycrystalline diamond films, processes such as microwave plasma CVD, hot filament CVD and plasma enhanced CVD is used [88], [91], [92]. Dependency of resistivity/ concentration and grain size is given in Figure 3.21. Variation of gauge factors of boron-doped polycrystalline diamond film over a silicon diaphragm has been investigated up to 500 °C [92]. The gauge factors were observed to vary in the range of 5-241. The gauge factors showed a decrease with increased temperature from room temperature to around 100–300 °C and an increase with further

higher temperature up to 500 °C. The oxidation of polycrystalline diamond films in air has been observed to begin at temperatures exceeding 600 °C, while in nitrogen environment no oxidation has been observed up to the studied temperature of 1300 °C [93]. Hence, the application of diamond based pressure sensor would be limited to about 600 °C in the case of oxidising ambient. The oxidation of diamond at higher temperatures could be prevented by the deposition of a suitable passivation layer over the diamond surface for further extending the operating temperature range.

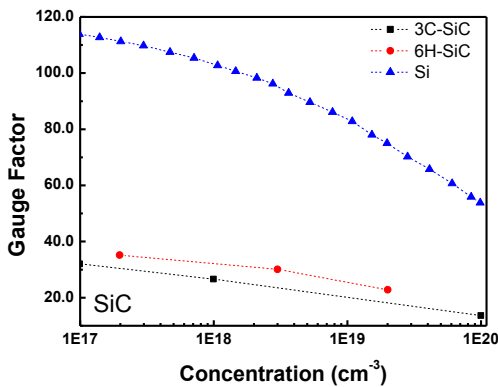


Figure 3.20: The magnitude of longitudinal gauge factor of single crystal silicon (p-type), 6H-SiC and 2 C-SiC at room temperature under varying dopant concentration [94]–[97].

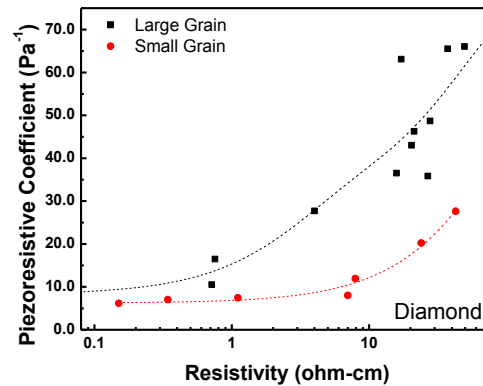


Figure 3.21: Piezoresistive coefficients as a function of resistivity and grains size (i.e. large =0.8 μm and small=0.3 μm) at room temperature [98].

Recently, nanocrystalline diamond (NCD) is considered a very promising material for fabrication of piezoresistive MEMS for harsh environment [99], [100]. The Temperature dependence of piezoresistance was measured from room temperature up to 200 °C for NCD films. The temperature dependence of the gauge factor was observed to be lower compared to the SOI silicon piezoresistors [99]. The gauge factor for NCD film was observed to be constant up to 120 °C and showed an increase up to 200 °C, while, SOI resistors showed a decrease of gauge factor. The technology of creating ultra-thin (< 200 nm) nanocrystalline diamond (NCD) films, on glass substrate, enabled fabrication of a pressure sensor for harsh environment [100]. Since these films can be deposited on different substrates and their properties could be tuned by varying deposition parameters,

unique pressure sensors using such films on other substrates could be developed for harsh environment applications.

3.5.3 Materials and methodology used for simulation study

Specific material properties as listed in Table 3.6 were used for the simulation study. In addition, particularly for polysilicon, SiC and diamond films, the gauge factors would depend on deposition conditions such as temperature, doping concentration, film thickness, etc. It would result in deviation of the experimentally observed parameters from the theoretically expected parameters. Material properties of the wide bandgap materials are selected from literature. Phan et al. have presented comparison of material properties of the most common single crystalline SiC polytypes with silicon and other wide bandgap materials such as diamond and GaN [64]. The material properties of silicon such as Young's modulus, Poisson's ratio, etc., depending on the orientation of the silicon wafer. Also the piezoresistive coefficients for silicon are dependent on orientation, type of doping, doping concentration and temperature [10], [71], [74], [101], [102]. The transverse and longitudinal piezoresistive coefficients of boron doped piezoresistors in $\langle 110 \rangle$ direction are of opposite polarity but almost equal in magnitude. Hence, boron doped $\langle 100 \rangle$ oriented silicon piezoresistors are used for the Wheatstone bridge configuration based silicon pressure sensors. Similarly, the piezoresistive coefficient of polysilicon piezoresistors vary with doping concentration and deposition conditions [10], [71], [74], [101], [102]. For standard boron-doped polysilicon films of the thickness of a few thousand nanometers and doping of about 10^{19} to 10^{20} cm^{-3} , the longitudinal gauge factor is 20-30 and transverse gauge factor is less than < -7 [103], [104]. However, recently it has been observed that nano-polysilicon films with 80-100 nm thickness have improved piezoresistive properties such as higher gauge factor and one order lower

temperature coefficient of resistance compared to the films of standard thickness [105]. Based on the various published reports, material properties of Si and poly Si were incorporated in the material database of the simulator. Similarly, the material properties for diamond or SiC used in the simulations were based on the published data [64], [77], [78], [106]. The material properties used for the simulation study are given in Table 3.6.

Table 3.6: Material properties and gauge factors of Si, Poly-Si, SiC and Diamond used for the simulation study.

Properties	Silicon [10],	Poly Silicon	SiC	Diamond	
	[71], [74], [101], [102]	[103], [104], [107]–[109]	[77], [105], [106]	[78]	
Elastic Constant (GPa)	130	170	445	1143	
Poisson's Ratio	0.28	0.28	0.19	0.07	
Shear Modulus (GPa)	50.78	66.40	186.79	554.85	
Density (kg/cm ³)	2.3	2.3	3.23	3.52	
Yield Strength (GPa)	7	7	21	> 60	
Gauge Factor	Longitudinal	122.0 ^a	39.4 ^b	30.3 ^c	9.89 ^d
	Transverse	-110.9 ^a	-15.2 ^b	-25.1 ^c	-2.82 ^d

^aGauge factor for silicon is considered for P-type boron doped piezoresistors with moderate doping $\sim 10^{18}$ cm⁻³ and <110> orientation. ^bFor polysilicon, the gauge factors are at doping of 4×10^{19} cm⁻³ [105]. ^cFor single crystalline SiC piezoresistors in <110> orientation, the piezoresistive coefficients are at doping of 5×10^{18} cm⁻³ [106]. ^dGauge factor for the polycrystalline diamond film is calculated from piezoresistive coefficient at a resistivity of ~ 20 Ω -cm [78].

The FEM simulation study of the pressure sensors involved i) defining the material properties, ii) incorporating the fabrication sequence of the device, and iii) incorporating the 2 D layout of the design as discussed earlier. A mapped brick type of mesh with the parabolic hex elements (27 nodes) as recommended in the software was used for generating finite element based mesh. The number of nodes and elements were 119643 and 13140 respectively with geometry volume as 3.57×10^9 μm^3 . The data obtained through simulations is further used for sensitivity calculations. FEM simulations were

done to calculate the electrical output based on induced stresses. The pressure sensor response in terms of the output voltage and sensitivity for various cases obtained through analysis of simulation data is discussed in the next section.

3.6 RESULTS AND DISCUSSION

The comparison of the response of the pressure sensors based on wide band gap materials with silicon based pressure sensors was done for two cases. In Case I, response of the pressure sensor was studied for incorporating bulk micromachined silicon diaphragm with oxide isolated piezoresistor of SiC and diamond on top of silicon diaphragm. The diaphragm of SiC or diamond could be then released by bulk micromachining of silicon until the interface with SiC or diamond layer. In Case II, response of the pressure sensor was analysed by incorporating bulk micromachined thin diaphragm and piezoresistors of the same materials with oxide isolation. A quantitative study using Finite Element Method for pressure sensor response with these materials incorporated as piezoresistors and diaphragms has been carried out. The analysis results presented in current section are also based on assumption which were discussed earlier.

3.6.1 Silicon diaphragm and piezoresistors of different materials

Generally, operating range of the pressure sensor is dependent on the geometrical dimension of the thin diaphragm and material properties, i.e. Young's modulus. Since Young's modulus of the SiC and diamond is higher as compared to silicon, a pressure range of SiC and diamond pressure sensors is expected to be higher than the silicon diaphragm based pressure sensor. Hence, in this analysis a smaller lateral dimension of silicon diaphragm is selected i.e. $500\ \mu\text{m} \times 500\ \mu\text{m}$ and thickness was optimized to $25\ \mu\text{m}$. This was based on the criteria that maximum deflection does not exceed more than

the 25 % of the diaphragm thickness at 10 MPa. Moreover, it was considered that there are no initial stresses in the diaphragm. The contour plots for deflection and von-Mises stress are shown in Figure 3.22 (a) and (b) respectively at 10 MPa. As expected, the deflection is maximum in the centre and stresses are concentrated in a region located at the middle of the diaphragm edge. The longitudinal (XX) and transverse (YY) stress contours are shown in Figure 3.22 (c) and (d) respectively for the silicon diaphragm.

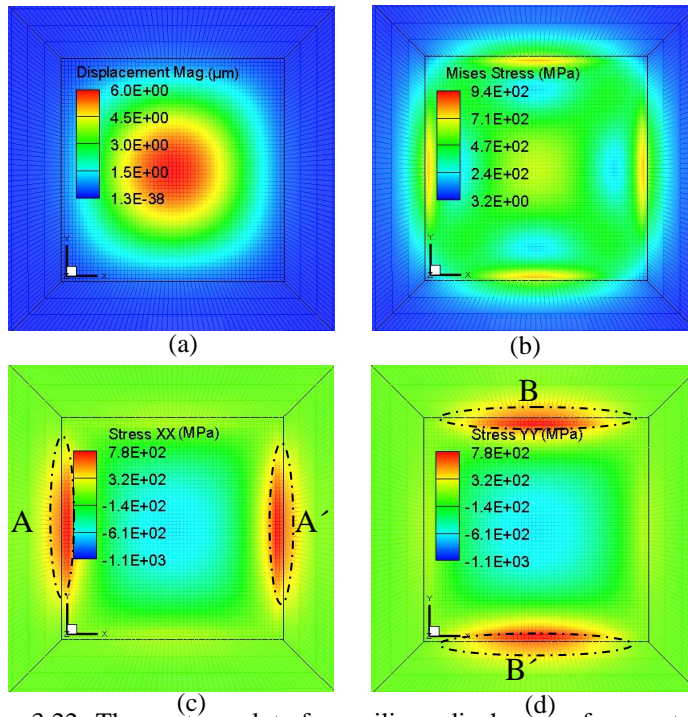


Figure 3.22: The contour plots for a silicon diaphragm of geometry $500 \mu\text{m} \times 500 \mu\text{m} \times 25 \mu\text{m}$ at an applied pressure of 10 MPa, (a) Deflection, (b) von- Mises stress, (c) Directional stress XX, (d) Directional stress YY.

The maximum tensile and compressive stress is observed at the middle of diaphragm edge and at the centre of the diaphragm respectively. The stress concentration regions are indicated as A, A' for stress XX (Figure 3.22(c)) and B, B' for stress YY (Figure 3.22(d)). Since the change in the resistance of piezoresistors is strongly dependent on the magnitude of stress, maximum stress locations as shown in Figure 3.22 (c) and (d) are selected for piezoresistor implantation/diffusion. The change of the resistance of piezoresistors is calculated based on the directional stresses and piezoresistive coefficient

of the piezoresistors. In order to maximize the sensitivity of pressure response, the location of two piezoresistors in the XX maximum stress regions i.e. A, A' and two piezoresistors in the YY maximum stress regions i.e. B, B' at the edges as can be seen from the contour plots were identified. The output voltage response is calculated for pressure sensors incorporating silicon diaphragm with piezoresistors of different materials, i.e. Si, Poly Si, SiC and diamond. Piezoresistors are considered electrically insulated from silicon diaphragm. Figure 3.23 shows the comparison of Wheatstone bridge output voltage variation with the input pressure for the pressure sensors incorporating silicon diaphragm with different piezoresistor materials.

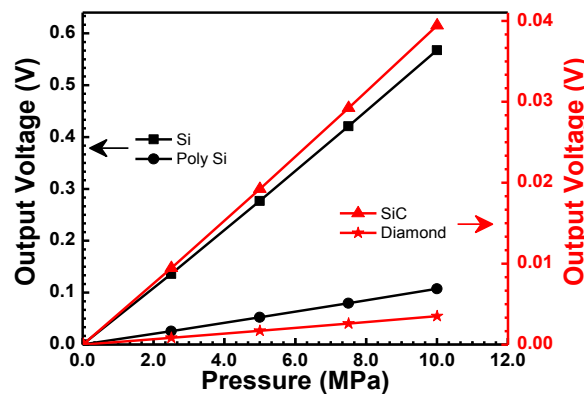


Figure 3.23: The output voltages of piezoresistive pressure sensors incorporating silicon diaphragms and Si, Poly-Si, SiC or diamond as piezoresistor materials, diaphragm geometry - $500 \mu\text{m} \times 500 \mu\text{m} \times 25 \mu\text{m}$.

From the plots shown in Figure 3.23, the sensitivity of pressure sensor for different piezoresistor materials was obtained and the data is listed in Table 3.7. As can be seen from Figure 3.23, pressure sensors with silicon diaphragms and with diamond or SiC piezoresistors exhibit quite lower sensitivities compared to a sensor incorporating single crystal silicon piezoresistors. The decrease of sensitivity for these piezoresistor materials can be attributed to their lower gauge factors compared to silicon. Additionally, for diamond and polysilicon, transverse gauge factors are also lower compared to longitudinal gauge factors causing a further decrease of sensitivity.

3.6.2 Diaphragm and piezoresistors of the same material

In this case, FEM simulations were carried out for obtaining the mechanical response of diamond and SiC diaphragms with the same geometrical parameters as those for the silicon diaphragm. The comparison of deflection and von-Mises stresses along a line through the centre of diaphragm for various diaphragm materials under the applied pressure of 10 MPa is given in Figure 3.24 and Figure 3.25 respectively. From Figure 3.24, it is evident that for a particular pressure and for identical geometrical parameters, deflection magnitudes are considerably lower for diamond and SiC diaphragms as compared to that observed for the silicon diaphragm. However, as expected, the generated stresses at the edges are of similar magnitudes for diaphragms of silicon, SiC and diamond (Figure 3.25).

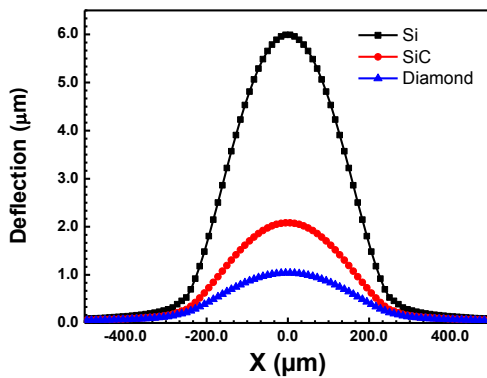


Figure 3.24: Deflection magnitudes along a line through the centre of the diaphragm for diaphragms of various materials, diaphragm geometry - $500 \mu\text{m} \times 500 \mu\text{m} \times 25 \mu\text{m}$, applied pressure -10 MPa.

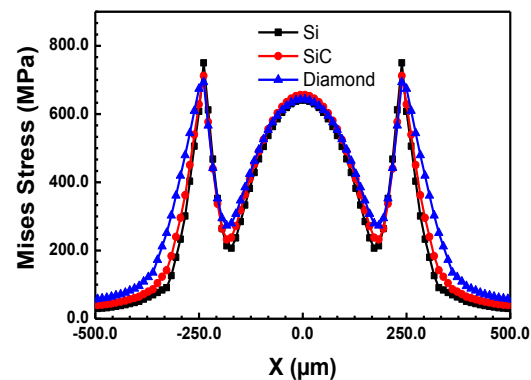


Figure 3.25: von-Mises stress magnitudes along a line through centre of the diaphragm for diaphragms of various materials, diaphragm geometry - $500 \mu\text{m} \times 500 \mu\text{m} \times 25 \mu\text{m}$, applied pressure -10 MPa.

The comparison of XX and YY directional stresses for these diaphragms is shown in Figure 3.26 and Figure 3.27 respectively. These plots show that at a particular pressure, the stresses are highest for a silicon diaphragm and lowest for a diamond diaphragm. The comparison of maximum deflection magnitudes and von-Mises stress magnitudes for diaphragms of different materials at various applied pressures is shown in Figure 3.28

and Figure 3.29 respectively. Using the data obtained through FEM simulations, the electrical outputs of the pressure sensors based on silicon, SiC or diamond is calculated. The output voltages of these piezoresistive pressure sensors for different pressures are plotted in Figure 3.30.

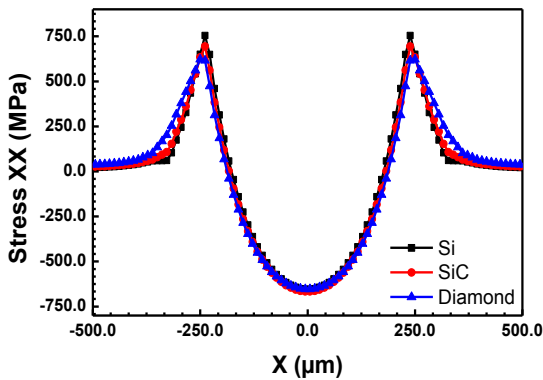


Figure 3.26: The directional stress XX along a line through the centre of the diaphragm for various diaphragms materials, diaphragm geometry - $500 \mu\text{m} \times 500 \mu\text{m} \times 25 \mu\text{m}$, applied pressure -10 MPa.

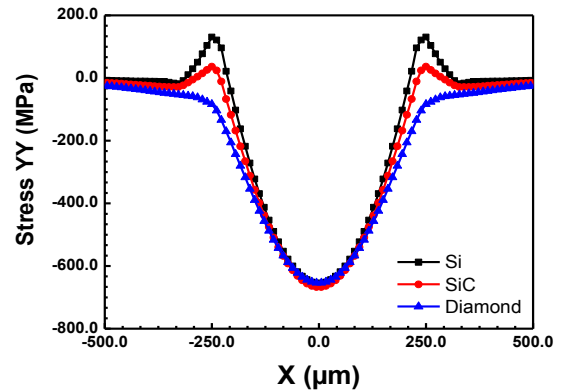


Figure 3.27: The directional stress YY along a line through centre of the diaphragm for diaphragms of various materials, diaphragm geometry - $500 \mu\text{m} \times 500 \mu\text{m} \times 25 \mu\text{m}$, pressure -10 MPa.

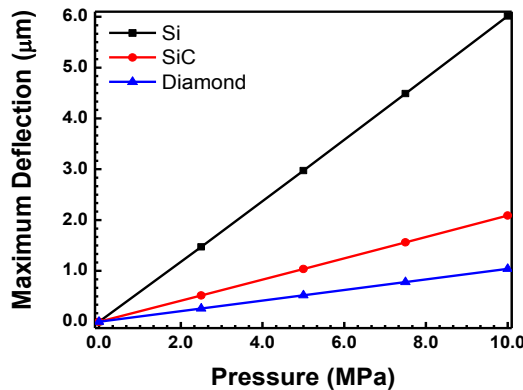


Figure 3.28: The maximum deflection vs applied pressure for various diaphragm materials, diaphragm geometry - $500 \mu\text{m} \times 500 \mu\text{m} \times 25 \mu\text{m}$.

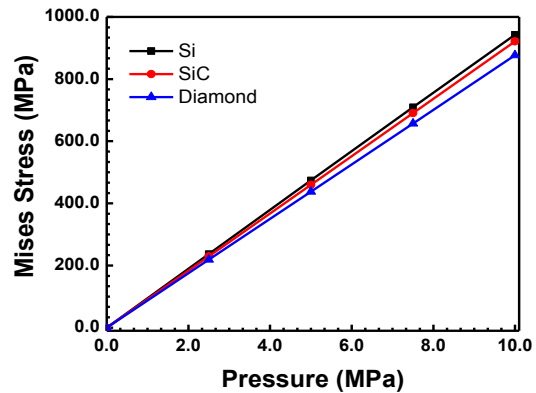


Figure 3.29: von-Mises stress vs applied pressure for various diaphragm materials, diaphragm geometry - $500 \mu\text{m} \times 500 \mu\text{m} \times 25 \mu\text{m}$.

Using the data plotted in Figure 3.28 and Figure 3.29, the deflection sensitivity and stress sensitivity were calculated and the data are tabulated Table 3.7. The observed decreased sensitivities of diamond and SiC based sensors are because of lower induced stresses for a particular applied pressure and mainly because of the lower gauge factors. The comparison of sensitivities tabulated in Table 3.7 shows that the sensitivities for diamond

and SiC are a bit higher when piezoresistors as well as diaphragm material both are diamond or SiC. Due to lower Poisson's ratio of diamond or SiC, the resultant stress (stress XX - stress YY) is higher when the diaphragm is fabricated with these materials compared to the resultant stress when diaphragm is fabricated with silicon. It could result in a higher change of piezoresistance resulting in higher sensitivity.

3.6.3 Improving sensitivity of diamond based pressure sensors

Since the transverse gauge factor of the diamond is very low, it is not suitable for a conventional piezoresistor configuration in which four resistors are placed close to the edges so that two resistors see longitudinal and two resistors see transverse stress. To take advantage of the fact that piezoresistive coefficient in the longitudinal direction is quite higher compared to the piezoresistive coefficient in the transverse direction, another geometry of locating piezoresistors for diamond based pressure sensor was investigated. In this geometry, two piezoresistors (longitudinal direction) are placed close to the edge and two piezoresistors (longitudinal direction) are placed in the centre. The output voltage calculated for this geometry is plotted in Figure 3.31. It is seen that sensitivity of pressure response is increased in configuration 2 compared to configuration 1. The sensitivity in configuration 1 (all piezoresistors are at the edges) is 3.9×10^{-4} V/V/MPa and the sensitivity in configuration 2 (two piezoresistors at the edge and two at centre) is 4.8×10^{-4} V/V/MPa.

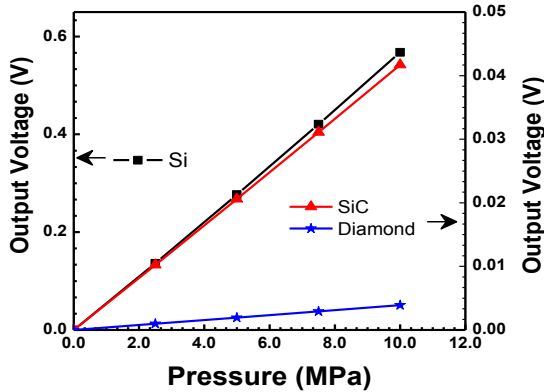


Figure 3.30: The output voltage of the pressure sensor based on Si, SiC and diamond, diaphragm geometry - $500 \mu\text{m} \times 500 \mu\text{m} \times 25 \mu\text{m}$.

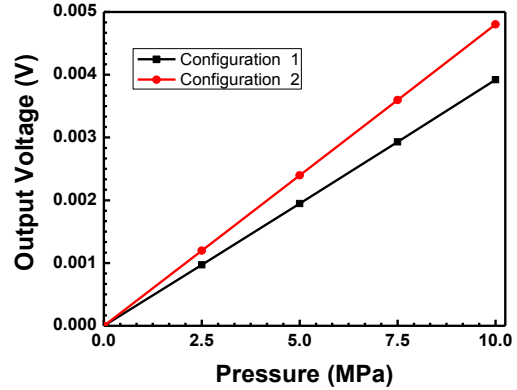


Figure 3.31: Sensitivity of diamond based pressure sensors with two different configurations for locating the piezoresistors.

3.6.4 Nonlinearity of pressure sensor response

In addition to sensitivity, the nonlinearity of response is an important specification for pressure sensors. Theoretically, the nonlinearity in the pressure response is due to the i) differences in the sensitivities of four piezoresistors comprising the Wheatstone bridge, ii) nonlinearity of the mechanical response with the applied pressure, and iii) nonlinearity of piezoresistive coefficients with stress.

As per the linear theory, it is assumed that the stress distribution is a result of pure bending. This assumption requires that the deflection of the diaphragm be small compared with its thickness. In the present case, the nonlinear structural analysis was included in the simulation. Hence the observed nonlinearity is only due to the deflection of the diaphragm. The % nonlinearity was calculated using equation 5.11 from the simulated output response of pressure sensors of different materials (Figure 3.32). The % nonlinearity obtained at a pressure of 10 MPa is tabulated (Table 3.7) for pressure sensors with Si, SiC or diamond diaphragms. From Figure 3.32, it is evident that the silicon based pressure sensor has higher % nonlinearity (-1.26 %) while diamond based pressure sensor has the least % nonlinearity (-0.30 %). Since the deflection for a particular pressure is

lower in diamond compared to silicon, diamond diaphragm based pressure sensor response is more linear compared to silicon for particular pressure input.

From Figure 3.32, it can be inferred that if the same % nonlinearity is considered, diamond based pressure sensors can be operated up to much higher pressures compared to silicon based pressure sensors. For e.g. for ~1.25 % nonlinearity, the maximum possible range of the pressure sensor is 10 MPa, 25 MPa and 55 MPa respectively for Si, SiC and diamond based pressure sensors. Thus, even if diamond based sensors have a lower sensitivity of response compared to silicon based sensors, they can be operated up to much higher pressures. It is found that % nonlinearity is higher in case of silicon based piezoresistive pressure sensor as compared to silicon carbide and diamond. For the given % Nonlinearity the operating pressure range is higher in case of SiC and diamond shown in Figure 3.32.

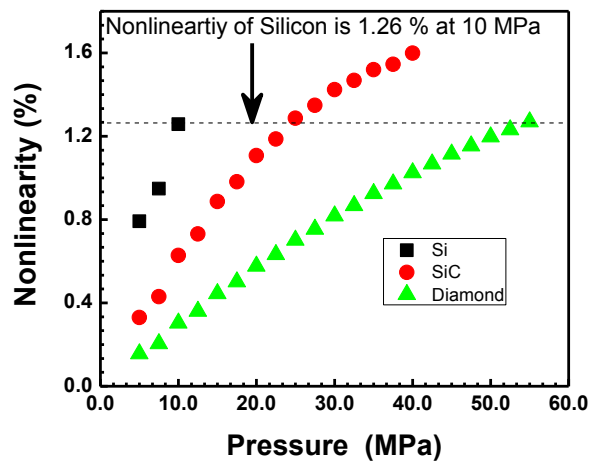


Figure 3.32: The % nonlinearity of pressure sensors incorporating diaphragm as well as piezoresistors of Si, SiC and diamond, diaphragm geometry - $500\ \mu\text{m} \times 500\ \mu\text{m} \times 25\ \mu\text{m}$.

As can be seen from Table 3.7, the pressure sensors with SiC or diamond piezoresistors are observed to have sensitivities lower by factors of 14.4 and 161.1 respectively with respect to the sensitivity of a conventional silicon piezoresistor based pressure sensor. The deflection sensitivity for silicon diaphragm is higher by a factor of about six times to

the deflection sensitivity of a diamond diaphragm while the stress sensitivities are of similar magnitudes. The comparison of the two types of configurations of diamond piezoresistors shows that improvement in the sensitivity by about 23 % can be obtained by a configuration in which resistors are located longitudinally over the diaphragm. The comparison of various parameters i.e. sensitivity, deflection and stress sensitivity obtained from the data plotted in Figure 3.22 to Figure 3.32 is presented in Table 3.7.

Table 3.7: Various parameters calculated from the data presented in Figure 3.22 to 3.32, diaphragm geometry $500 \mu\text{m} \times 500 \mu\text{m} \times 25 \mu\text{m}$, maximum applied pressure 10 MPa.

Parameters	Materials			Remark	
	Silicon	SiC	Diamond		
Sensitivity(V/V/MPa)	Case I	4.4×10^{-2}	3.1×10^{-3}	2.7×10^{-4}	
	Case II	4.4×10^{-2}	3.5×10^{-3}	3.6×10^{-4}	(config.1)
			4.5×10^{-4}	(config.2)	
Deflection sensitivity ($\mu\text{m}/\text{MPa}$)	0.6	0.2	0.1		
Von-Mises Stress Sensitivity	94.3	92.1	87.6		
% Nonlinearity	-0.8	-0.6	-0.3		

3.7 SUMMARY

The design optimisation of piezoresistive pressure sensors in terms of the geometrical dimensions of the diaphragm and location of piezoresistors are presented using the FEM simulation. The variation of the deflection and induced stress as a function of thickness are found to be as expected. The locations of piezoresistors on diaphragms are optimised to obtain maximum sensitivity. The electrical output and % non-linearity of the piezoresistive pressure sensor is also estimated using FEM simulation. The change of pressure response at different temperatures is investigated by providing temperature variation of mobility in the doped piezoresistors and change of piezoresistive coefficient as input parameters to the simulator. Moreover, a quantitative analysis of the temperature effect on piezoresistive pressure sensor response for operation at 200 bar, 200 °C is

presented. A quantitative study of the response of pressure sensors based on high bandgap materials such as SiC and diamond has been carried out as these materials are suitable for high radiation environment and high-temperature operation. Based on the simulation study of silicon based pressure sensors, the design of the sensors was optimized. The details of fabrication of pressure sensors using the optimized design is presented in the next Chapter.

Chapter 4. MASK DESIGN, FABRICATION OF PRESSURE SENSORS AND DESIGN & DEVELOPMENT OF A SIGNAL CONDITIONING CIRCUIT

4.1 INTRODUCTION

Design optimisation and simulation study for the piezoresistive pressure sensor was presented in the earlier Chapter. In this Chapter, layout design is presented to fabricate masks for the piezoresistive pressure sensors. The mask design was done based on the optimised parameters presented in Chapter 3. The fabrication process adopted for the fabrication of diffused and Silicon-On-Insulator (SOI) technology based pressure sensors is discussed. Moreover, development of signal conditioning circuit for pressure sensors is described for compensation of offset voltage and to obtain current response in 4-20 mA.

4.2 MASK DESIGN OF DIFFUSED AND SOI TECHNOLOGY BASED PRESSURE SENSORS

The schematic cross section of diffused piezoresistor and SOI technology based pressure sensors is given in Figure 4.1 (a) and (b) respectively.

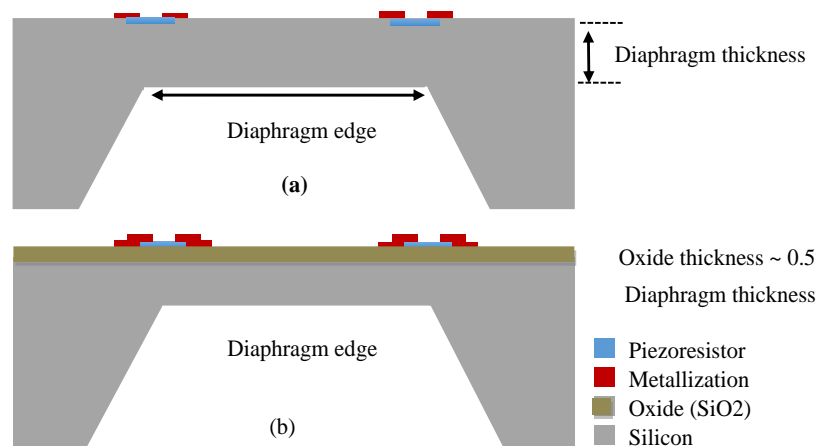


Figure 4.1: Schematic for cross-section view of (a) Diffused piezoresistors and (b) SOI based pressure sensor

The dimensions of piezoresistor, contact pads, width of metal lines and contact pads opening used for the mask design of these sensors are listed in Table 4.1. These parameters were finalised considering the processing equipment capability of the foundry. Mask design was targeted to obtain two ranges of pressure sensor chips in a single wafer process by keeping the diaphragm thickness constant. The design was done for two thicknesses of diaphragms, i.e. 200 μm and 150 μm . Based on the simulation results, the dimensions of diaphragms were chosen and listed in Table 4.2 for the diaphragm thickness of 200 μm and 150 μm respectively.

Table 4.1: Dimensions for piezoresistors, pad dimensions, contact pad openings and metal line width.

Types	Dimensions
Piezoresistor dimension	100 μm \times 10 μm
Contact opening to Piezoresistor	10 μm \times 10 μm
Pad dimension	200 μm \times 200 μm
Metal line width	20 μm

Table 4.2: Dimensions of diaphragm for pressure sensor, pressure range 200 and 100 bar.

Pressure Range (bar)	Dimensions of diaphragm (μm \times μm \times μm)	Backside-etch opening* (μm \times μm)
200 bar	1000 \times 1000 \times 200	1212 \times 1212
100 bar	1414 \times 1414 \times 200	1626 \times 1626
200 bar	750 \times 750 \times 150	1033 \times 1033
100 bar	1060 \times 1060 \times 150	1343 \times 1343

*Calculation for the back side opening has been done using the assumption that thickness of the wafer is 350 μm .

The parameters listed in Table 4.2 were used for the fabrication of masks for diffused piezoresistor as well as the SOI based pressure sensors. However, alignment marks for diffused piezoresistors and SOI based pressure sensors were different because of the differences in fabrication processes. Hence, separate sets of masks were fabricated for

these two types of sensors. The pictorial representation for layout of a single chip and an array of the pressure sensor dies on the wafer are presented in Figure 4.2 for diffused and SOI technology based sensors. The details of the mask for diffused piezoresistor and SOI based pressure sensor are given in Table 4.3.

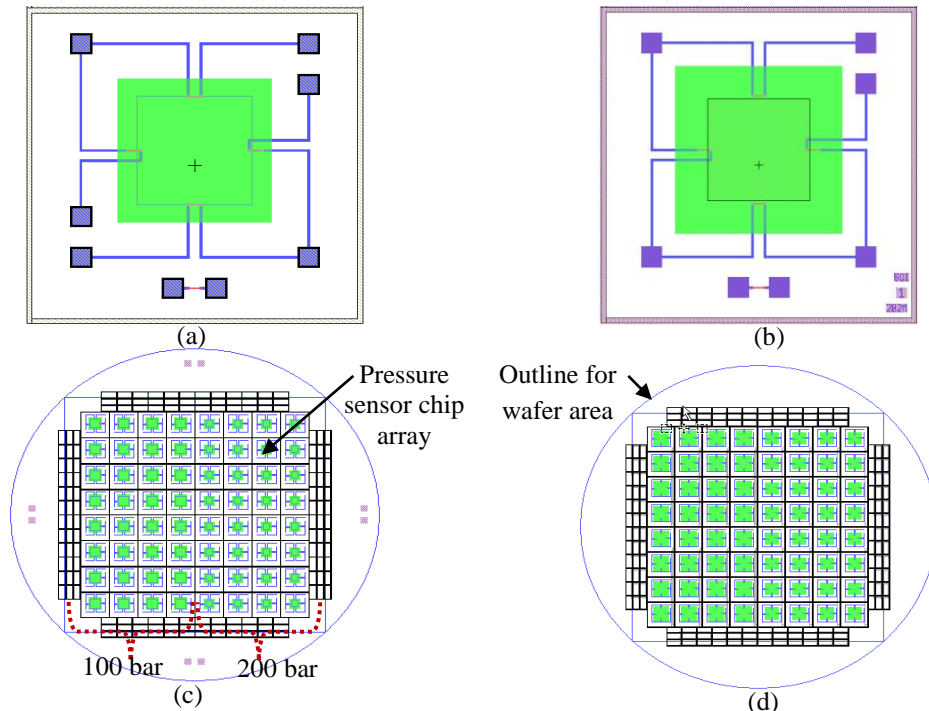


Figure 4.2: Snapshots of the mask layout for diffused piezoresistor and SOI technology based piezoresistive pressure sensors: (a) Chip layout for the diffused piezoresistor sensor, (b) Chip layout for SOI based pressure sensor, (c) Diffused piezoresistor sensor layout for 8×8 array, (d) SOI technology based pressure sensor layout for 8×8 array.

Table 4.3: Mask details for piezoresistive pressure sensor

Mask No.	PLG Step	Step Name	Field Type
Mask#1	PLG 1	Alignment	Dark Field
Mask#2	PLG 2	Gridline	Dark Field
Mask#3	PLG 3	Cavity	Dark Field
Mask#4	PLG 4	PZR	Dark Field
Mask#5	PLG 5	Metallisation	Bright Field
Mask#6	PLG 6	Passivation	Dark Field
Mask#7	PLG 7	Contact open	Dark Field

The mask consists of the features (device area) and field (non-device area). Therefore, all the masks are classified in the dark and bright field mask. First, second, third and seventh masks are dark field for alignment and thickness control, gridline, cavity and

metallisation respectively. Whereas, fourth, fifth and sixth masks are bright field for piezoresistor, passivation and contact opening respectively.

4.3 FABRICATION PROCESS DEVELOPMENT FOR PIEZORESISTIVE PRESSURE SENSORS

The fabrication processes for diffused piezoresistor and SOI based pressure sensor were decided so that they have many common steps except for the boron diffusion step. The SOI wafers were procured with a device layer of specific concentration and thickness so that this layer itself can be used for piezoresistors. The device layer was separated by a thin ($\sim 1.0 \mu\text{m}$) buried oxide layer from the handle layer. The handle layer was etched to realise the diaphragm. Moreover, thickness of the device layer was reduced using oxidation process and subsequent etching of oxide layer. In this section, the fabrication process flow for diffused and SOI technology based pressure sensor is described.

4.3.1 Fabrication process for diffused piezoresistor based pressure sensor

The fabrication process steps used for the fabrication of diffused piezoresistor based pressure sensors are listed below:

- (i) Silicon wafer with 100 orientation is selected to fabricate the pressure sensor.
- (ii) A thermally grown layer of SiO_2 is grown for the alignment mark and gridlines.
- (iii) Backside window opening is performed to create diaphragm by TMAH etching.
- (iv) Subsequently, the process step for the boron diffusion is performed to create piezoresistors as transduction elements.
- (v) Further, metallisation is carried out to connect the piezoresistors in Wheatstone bridge configuration.

- (vi) A passivation layer of SiO₂ is deposited to protect the piezoresistors and metal lines from external environments.
- (vii) In order to package the pressure sensor chips, a glass wafer was bonded to the backside of the fabricated wafer.
- (viii) Finally, the LASER dicing is performed to separate the pressure sensor chips.

The above processes are schematically presented in step 1 to 8 of Figure 4.3.

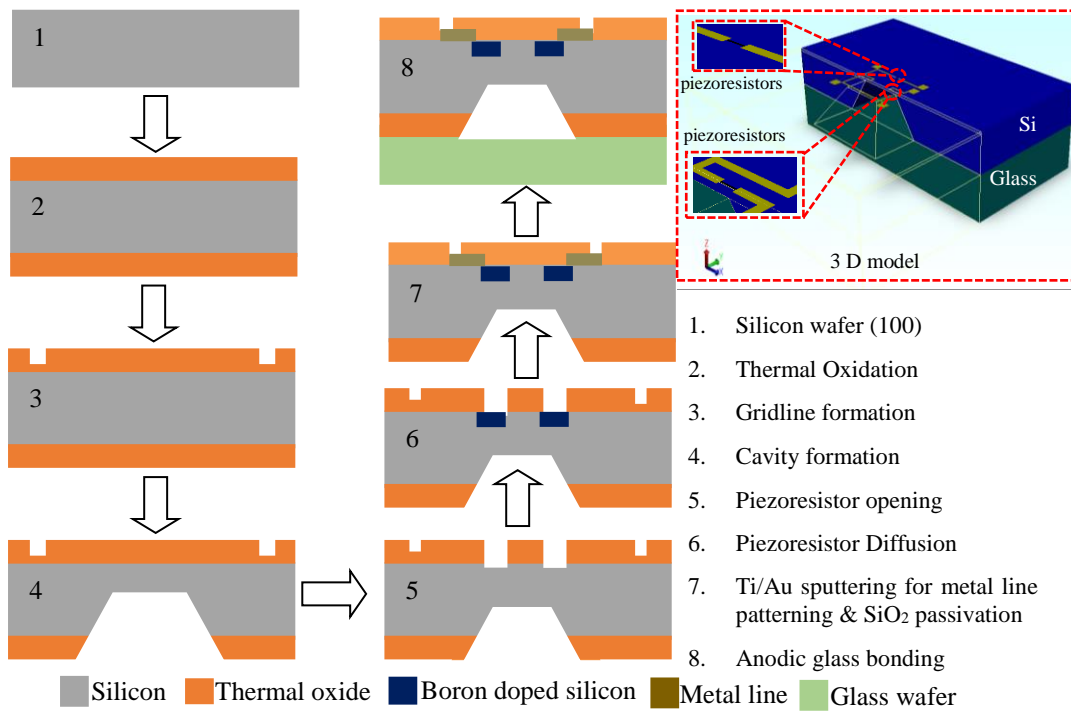


Figure 4.3: Schematic of fabrication process flow of boron diffused piezoresistor based piezoresistive pressure sensor.

The photographs of the fabricated wafer as viewed from the backside and top side for diffused piezoresistor based pressure sensors are presented in Figure 4.4 (a) and (b) respectively. Backside cavity and top side gridlines are clearly visible in the photographs. Magnified views for the top and backside of the fabricated pressure sensor chip are presented in Figure 4.4 (c) and (d) respectively. After fabrication, the fabricated sensor chips were attached to a TO-12 header and wire bonding was done in order to connect bonding pads of the chip to the pins of TO-12 header. The picture of the pressure sensor

mounted on the TO-12 header is given in Figure 4.4 (e). For testing the pressure sensor, the TO-12 header was housed in a leak-proof stainless steel housing (Figure 4.4 (f)). The performance investigations of pressure sensor was studied by carrying out various measurements after final assembly.

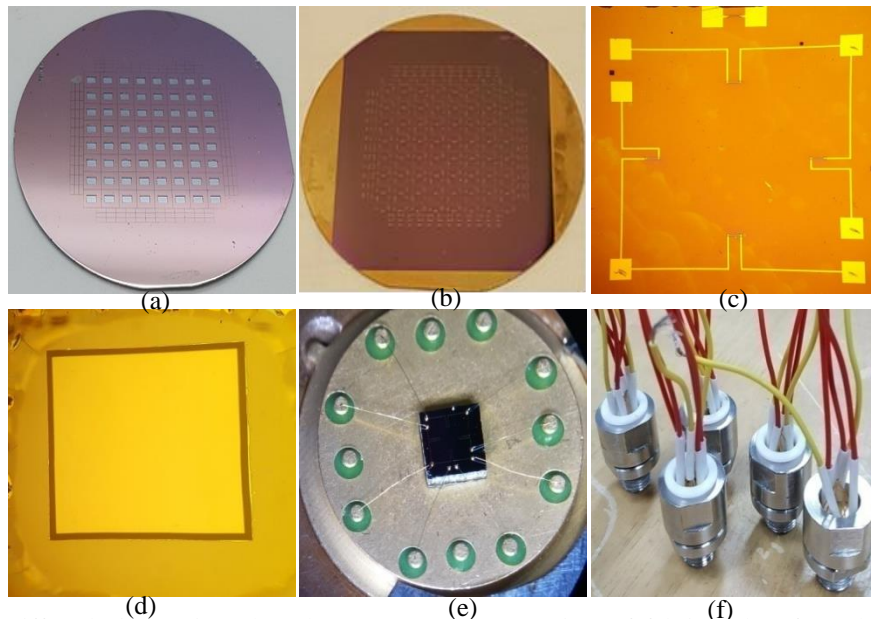


Figure 4.4: Diffused piezoresistor based sensors; (a) Bottom view of fabricated wafer , (b) Top view of fabricated wafer , (c) Pressure sensor chip top view, (d) Bottom view of pressure sensor chip (e) Sensor chip attached on a TO-12 header and wire bonded, (f) Packaged pressure sensor chip in a stainless steel housing.

4.3.2 Fabrication process for SOI based pressure sensor

The fabrication process flow of SOI technology based pressure sensor is described below:

- (i) SOI wafers with device layer thickness of $2\ \mu\text{m}$, handle layer of $650\ \mu\text{m}$ and a buried oxide layer of $1\ \mu\text{m}$ are used for the fabrication of pressure sensors.
- (ii) Wafers are oxidised for obtaining one-micron thick oxide layer and the oxide is etched. This is done to reduce the device layer thickness.
- (iii) Thermal oxidation is done to create alignment marks and for grid line etching.
- (iv) Afterwards, photolithography of gridline is performed followed by the photolithography of the backside cavity. The top side gridline is protected during window opening for cavity etching.

- (v) The piezoresistors are etched in the device layer and metallisation is performed to connect all piezoresistors in Wheatstone bridge configuration.
- (vi) Further, passivation with deposited oxide is performed to protect the metal lines and piezoresistors from the external environments.

The process steps are shown schematically in Figure 4.5 (1-7).

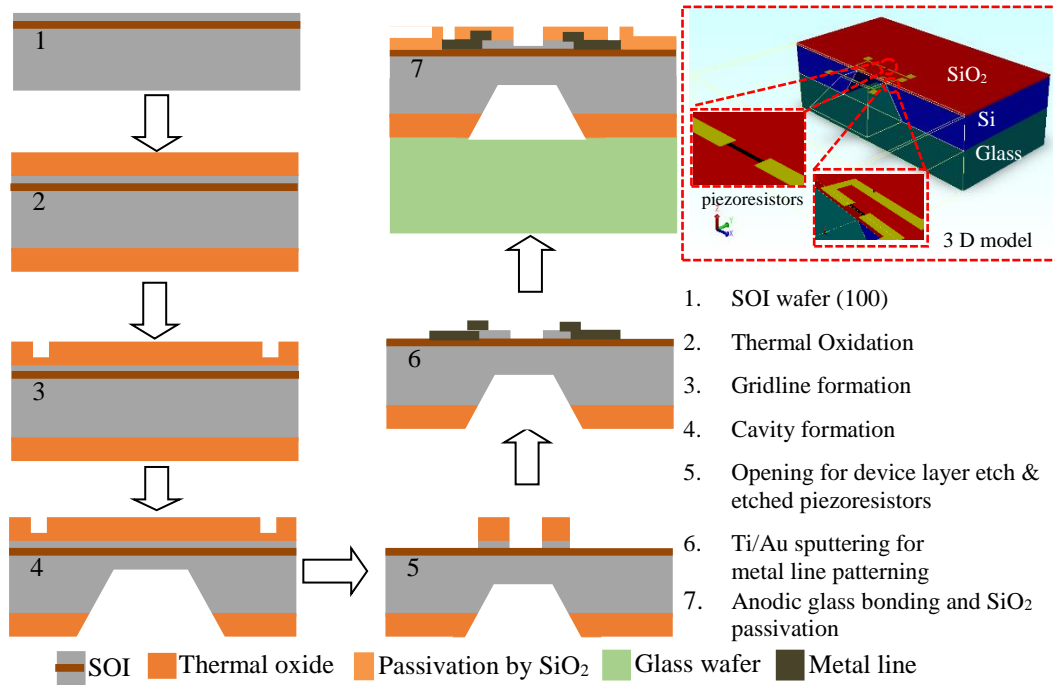


Figure 4.5: Schematic of fabrication process flow for SOI based piezoresistive pressure sensor.

The photographs of the fabricated wafer of SOI technology based piezoresistive pressure sensor are presented in Figure 4.6 (a) and (b). The magnified view of a die showing all four piezoresistors in a Wheatstone bridge configuration and a particular piezoresistor are shown in Figure 4.6 (c) and (d) respectively. The fabricated pressure sensor chips were attached to TO-12 headers and contact pads were wire bonded with header pins Figure 4.6 (e). Finally, TO-12 header with pressure sensor chip was packaged in the stainless steel housing similar as diffused pressure sensor (Figure 4.4 (f)) for characterisation of pressure sensor response.

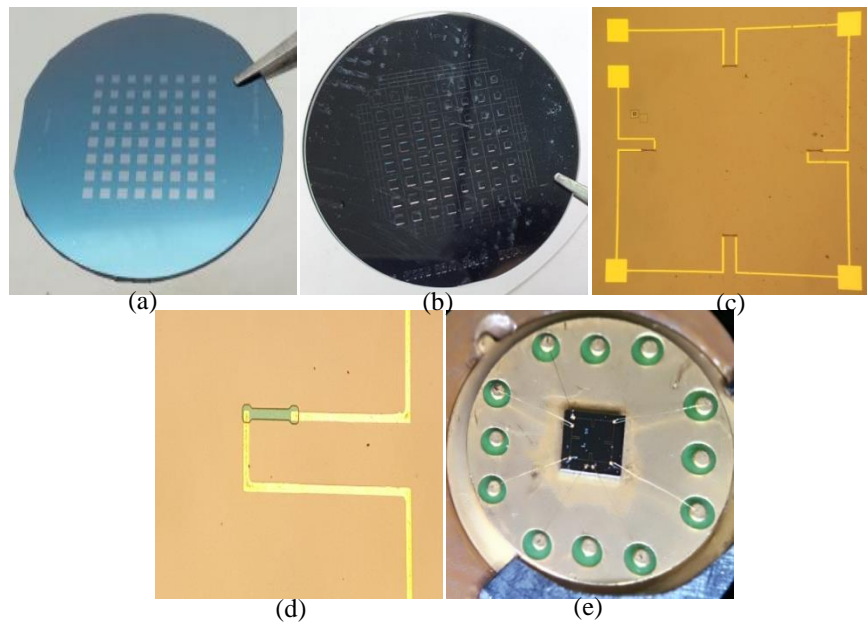


Figure 4.6: (a) Fabricated SOI wafer, (b) Glass bonded wafer, (c) Top view of sensor chip, (d) Magnified view of piezoresistor (e) pressure sensor chip attached with TO-12 header.

4.4 DETAILS OF PRESSURE SENSOR PACKAGE

The pressure sensor packaging is a crucial step in order to test the pressure response. The packaging needs to be leak proof and electrically isolated from the device. There is no universal packaging technique available for MEMS devices because the devices are designed to operate in specific application area. In order to investigate the response of the pressure sensor chips for different applied pressures, the sensor chip with a TO-12 header was packaged in the stainless steel housing. Pictorial representation of the parts used to package and its exploded view are given in Figure 4.7 (a) and (b).

The following parts were used in the metal housing used for packaging:

- a. Teflon Jacket in order to make isolation of header leads.
- b. Stainless steel housing with $\frac{1}{4}$ inch NPT threads.
- c. Metal washer in order to make leak proof housing.
- d. TO-12 header.

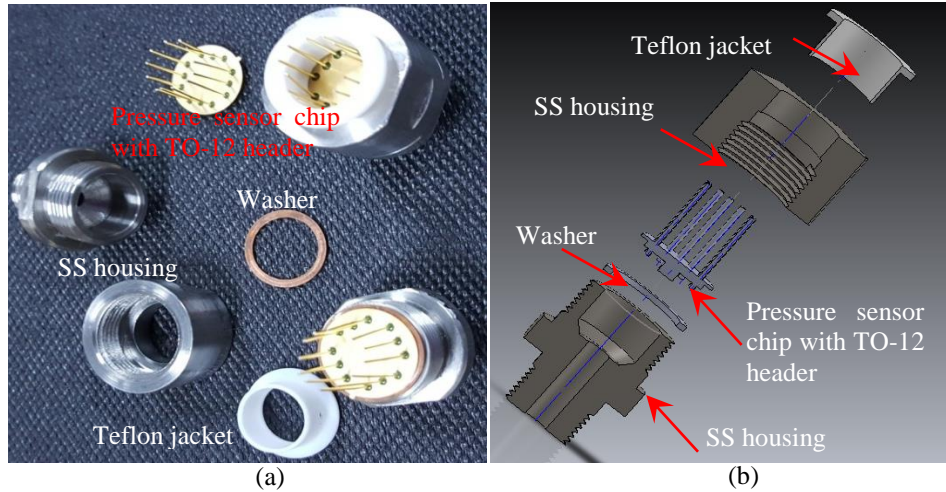


Figure 4.7: (a) Parts used for packaging of the pressure sensor, (b) Exploded view of pressure sensor package.

In the next section, design and fabrication of a signal conditioning circuit are discussed.

4.5 SIGNAL CONDITIONING CIRCUIT

The pressure sensor converts non-electrical signal, i.e. pressure, into electrical signal, i.e. voltage. However, the electrical output of the sensors needs further amplification. Therefore, a signal conditioning circuit is needed for amplification of pressure sensor output to a suitable voltage or current level for further processing. The Wheatstone bridge on the top of the thin diaphragm is one of the most used techniques to convert pressure signal into the electrical signal. The resistances of Wheatstone bridge piezoresistors are not identical which leads to the offset voltage. A suitable compensation technique is required to compensate the offset voltage. Design, fabrication and experimental evaluation of the signal conditioning circuit were carried out for offset compensation, output amplification and to obtain 4 to 20 mA output response. The 4-20 mA current response is highly immune to external noise and hence is an industry standard.

4.5.1 Analysis and modelling of Wheatstone bridge for offset voltage compensation

A piezoresistive pressure sensor is fabricated using the MEMS technology with bulk

micromachined silicon diaphragm having implanted/diffused piezoresistors on the top of thin diaphragm. The output of the bridge must be zero under unstressed condition and it must also remain zero for other any temperature because all four resistors have the same temperature coefficients. However, in practice there is always a non zero voltage output under the unstressed condition. The non-zero output is referred to as the offset voltage of the piezoresistive pressure sensor. The main possible reasons for offset voltage are [35]:

- i. Geometrical deviation of resistors from their nominal values.
- ii. Initial stresses in the diaphragm due to the thermal mismatch of the piezoresistor layer and silicon substrate.
- iii. Non-identical temperature dependency of piezoresistors.

Here, analytical modelling of the offset voltage and temperature coefficient of offset (TCO) is presented. We consider that all four piezoresistors are identical and equal to the nominal resistance $R_1 = R_2 = R_3 = R_4 = R_b$ as shown in Figure 4.8.

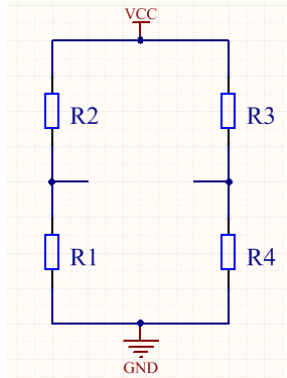


Figure 4.8: Wheatstone bridge configuration.

Also, we assume that each resistance has some deviation from the nominal resistance value, i.e. $R_1 = R_b(1 + \delta_1)$, $R_2 = R_b(1 + \delta_2)$, $R_3 = R_b(1 + \delta_3)$ and $R_4 = R_b(1 + \delta_4)$.

$$V_{offset} = V_{o1} - V_{o2} = \frac{R_1 R_3 - R_2 R_4}{(R_1 + R_2)(R_3 + R_4)} V_{cc} = \left(\frac{\delta_1}{4} + \frac{\delta_3}{4} - \frac{\delta_2}{4} - \frac{\delta_4}{4} \right) V_{cc}, \quad V_{offset} = \left(\frac{\delta}{4} \right) V_{cc} \quad (4.1)$$

Where, $\frac{\delta}{4} = \frac{\delta_1}{4} + \frac{\delta_3}{4} - \frac{\delta_2}{4} - \frac{\delta_4}{4}$

The offset voltage is not temperature dependent if and only if all the resistors have the same temperature coefficient of resistance. It is difficult to get an identical temperature coefficient for all piezoresistors [35]. Hence, the compensation of offset voltage is essential task before signal conditioning. The configuration for the offset compensation is presented in (Figure 4.9 (a) –(c)).

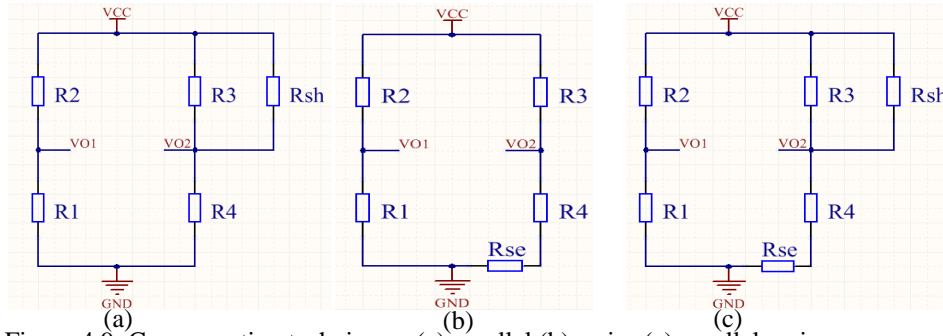


Figure 4.9: Compensation techniques; (a) parallel (b) series (c) parallel-series.

The offset compensation is usually done by a passive resistor component in the parallel or series configuration. In order to make offset voltage less temperature dependent, the passive resistor is to be selected with a smaller temperature coefficient than the diffused/implanted piezoresistors. Mathematically, the required value of selected resistor for offset compensation is calculated as explained in the consecutive sections.

4.5.1.1 Offset compensation using a parallel configuration

The compensation resistor is utilised to tune the value as per the desired nominal resistance [35]. Hence, resistance of parallel configuration is equal to nominal resistance,

R_b (Figure 4.9 (a)).

$$\frac{R_3 R_{sh}}{R_3 + R_{sh}} = R_b \frac{R_b (1 + \delta_3) R_{sh}}{R_b (1 + \delta_3) + R_{sh}} = R_b \quad ; \text{or } \delta_3 R_{sh} = R_b + R_b \delta_3 \quad (4.2)$$

Where, δ_3 is a smaller value, hence,

$$R_{sh} = \frac{R_b}{\delta_3} \quad (4.3)$$

Generally, TCR is defined as; $TCR = \frac{R_t - R_0}{R_0} \frac{1}{T_t - T_0}$

$$TCR_{R_3 \parallel R_{sh}} = \frac{R_{3t} \parallel R_{sh} - R_0 \parallel R_{sh}}{R_0 \parallel R_{sh}} \frac{1}{T_t - T_0}; \quad TCR_{R_3 \parallel R_{sh}} = \frac{R_{sh}}{R_0 + R_{sh}} \frac{R_{3t} - R_0}{R_0} \frac{1}{T_t - T_0} \quad (4.4)$$

$$TCR_{R_3 \parallel R_{sh}} = \frac{R_{sh}}{R_0 + R_{sh}} TCR_3 \quad (4.5)$$

Where, $R_3 \parallel R_{sh}$ is the parallel configuration of the resistors and TCR_3 is TCR for piezoresistor R_3 . Due to the parallel configuration effective "Temperature coefficient of Resistance" (TCR) is reduced as shown in the above equation.

4.5.1.2 Offset compensation using series configuration

The compensation resistor is utilised to tune the value as per the desired nominal resistance [35]. Hence, the resistance of series configuration should be equal to the nominal resistance (Figure 4.9(b)).

$$R_4 + R_{se} = R_b \text{ or } R_b(1 + \delta_4) + R_{se} = R_b \quad (4.6)$$

$$R_{se} = -\delta_4 R_b \quad (4.7)$$

The effective temperature coefficient of resistance (TCR_{eff}) is calculated for series configuration as;

$$TCR_{R_3 + R_{se}} = \frac{(R_{4t} + R_{se}) - (R_0 + R_{se})}{R_0 + R_{se}} \frac{1}{T_t - T_0} \text{ or } TCR_{R_3 + R_{se}} = \frac{R_{4t} - R_0}{R_0 + R_{se}} \frac{1}{T_t - T_0} \quad (4.8)$$

Hence, the effect of the TCR due to the Wheatstone bridge resistance is reduced due to external passive components as shown in the above equations.

4.5.1.3 Offset compensation using parallel-series configuration

Offset compensation of the piezoresistive pressure is done using parallel-series compensation technique [35]. The parallel-series configuration is given in Figure 4.9(c).

4.5.2 Design and testing of signal conditioning circuit

As per industrial standards, the response of pressure sensor is calibrated in terms of 4 to 20 mA current for zero and maximum applied pressure respectively. Based on the requirements of pressure sensor output signal processing, a survey was conducted for various ICs suitable for the application. The IC XTR105 by Texas Instruments Inc. was identified for the development of the electronics. The schematic of the signal conditioning circuit is shown in Figure 4.10. A layout of circuit was made, the PCB was fabricated and fabricated PCB was assembled with required components (Figure 4.11).

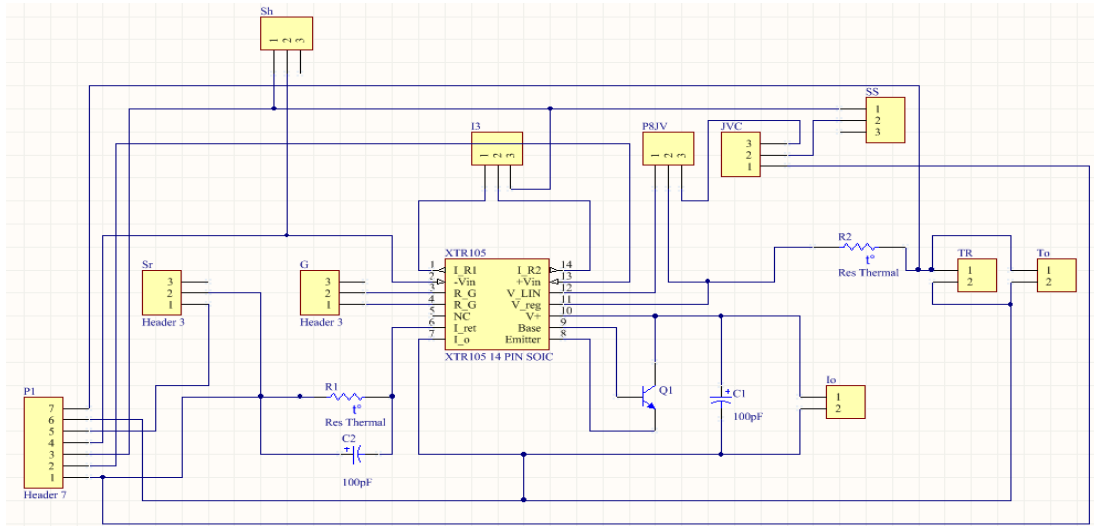


Figure 4.10: Schematic of the signal conditioning circuit for obtaining 4 to 20 mA current loop response.

The designed circuit has features such as; i) possibilities for the compensation of offset voltage by one of the three configurations as discussed above, ii) amplification of sensors output, iii) constant voltage or constant current supply source. Finally, the designed and fabricated signal conditioning circuit was tested for 4 to 20 mA current output and offset voltage compensation using a pressure sensor. The sensor was characterised with and without offset compensation. The testing results of the developed signal conditioning circuits are presented for compensation of offset voltage. The output voltage was recorded for uncompensated and compensated case using a commercial pressure sensor.

In addition, response in terms of the 4 to 20 mA was obtained for uncompensated and compensated pressure response.

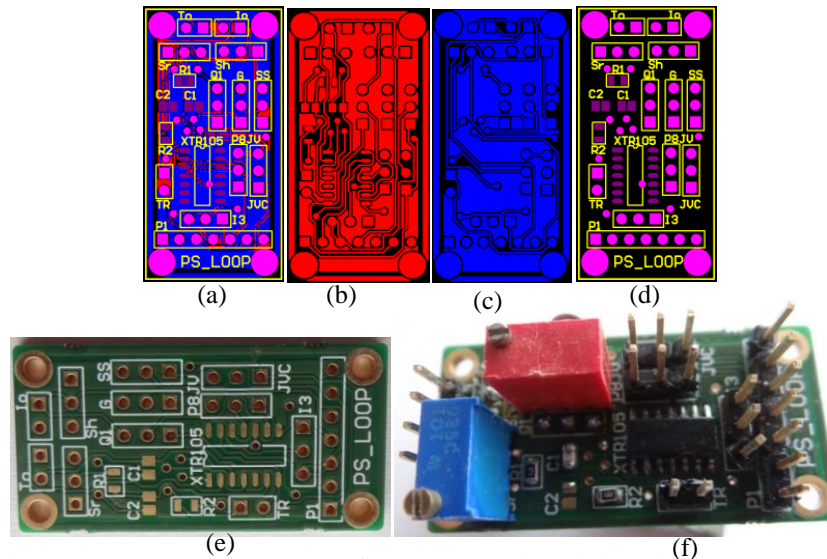


Figure 4.11: PCB design layout files (a, b, c, d), Fabricated PCB top (e), and Assembled PCB with components (f).

The XTR105 is a current transmitter IC with 4-20mA response using 2-wire. It also has a provision to amplify the output voltage. It has two precision power sources i.e. constant current and constant voltage source. It is mainly consisting of instrumentation amplifiers with gain control option and current output circuit on a single IC. The instrumentation amplifier gain can be configured for a wide range of pressure/ temperature measurements. The XTR105 operates on loop power-supply voltages down to 7.5V.

The sensor performance was measured under uncompensated condition using both the supply modes. The offset voltage was subsequently nullified using the designed and developed signal conditioning circuit. The data obtained after offset compensation is presented in Figure 4.12 (a). The response of pressure sensor in terms of the 4 -20 mA output is presented in Figure 4.12 (b).

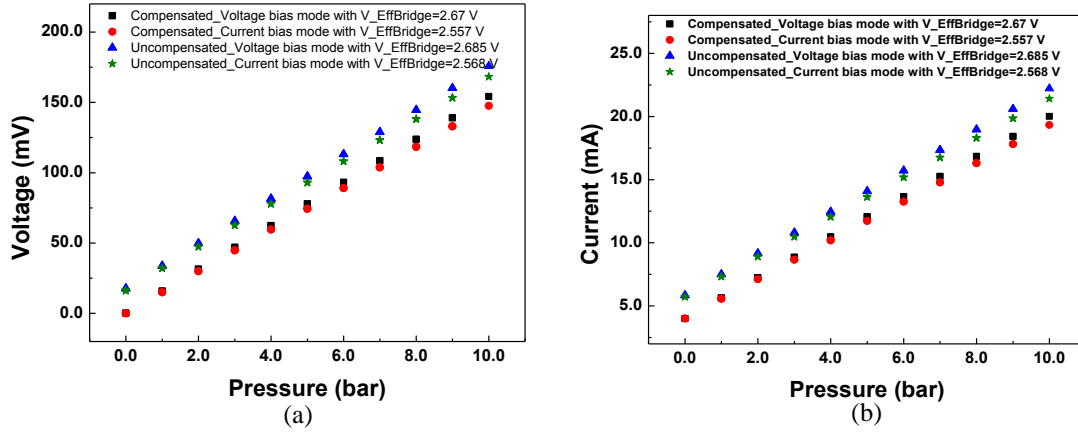


Figure 4.12: (a) Voltage response of pressure sensors for uncompensated and compensated conditions, (b) The 4-20 mA current response for uncompensated and compensated conditions.

The compensation of offset voltage was successfully achieved using the developed signal conditioning circuit in both the supply modes i.e. constant current source and constant voltage source. The results of testing of the circuit are presented in Table 4.4.

Table 4.4 Results of testing of signal conditioning circuit.

Resistance	R_t k Ω	R_{12} k Ω	R_{23} k Ω	R_{34} k Ω	R_{54} k Ω	R_b k Ω	Effective supply voltage (V)	Voltage at series-shunt Resistor (V)	Compensated resistance		Remark
									R_{sh} (k Ω)	R_{se} (Ω)	
Uncompensated	13.75	3.42	3.48	3.39	3.47		2.685	2.359	NA	NA	
	13.65	3.46	3.39	3.47	3.41	3.43	2.677	2.359	132.3	~2	Parallel
Compensated	13.72	3.49	3.40	3.45	3.39	3.45	2.695	2.359	∞	90.39	Series
	13.63	3.46	3.39	3.39	3.39	3.41	2.675	2.374	148.9	11.26	Series-Parallel

4.6 SUMMARY

In this Chapter, the mask design of the pressure sensor was presented in order to fabricate the mask for pressure sensor development. The pressure sensor was fabricated based on the diffused piezoresistors and SOI based technology. The fabrication processes were discussed in detail. The packaging process adopted for the pressure sensor was explained.

In order to compensate offset voltage and to obtain 4-20 mA response, the design, fabrication and testing of PCB were carried out. The operation of this circuit was demonstrated using a commercial pressure sensor which was not having its own signal conditioning circuit. The performance investigation of fabricated pressure sensors is discussed in the next Chapter.

Chapter 5. PERFORMANCE INVESTIGATION OF PIEZORESISTIVE PRESSURE SENSORS

5.1 INTRODUCTION

The performance of pressure sensors fabricated in this work in terms of sensitivity, offset voltage, offset drift, linearity, and hysteresis was investigated. The effect of operating temperature on the sensitivity was also studied. The fabrication process was first optimized for diffused resistor pressure sensors as there were many process steps which were common with the SOI technology based sensors. Using the optimized process steps, the fabrication process for SOI based sensors was further optimized. The details of various measurements are presented in this Chapter.

5.2 CHARACTERISATION SETUP

In order to investigate the performance of the pressure sensors, a characterisation setup comprising the following units was built:

- a. Pneumatic pressure pump and pressure hose in order to apply the pressure.
- b. Multipurpose calibrator with a reference pressure sensor, power supply and recording instrument to calibrate the pressure sensor under investigation.
- c. Digital multi-meter for the measurement of the resistance of piezoresistors.
- d. Temperature environment chamber with a temperature controller to perform the experiment under elevated temperatures.

The multipurpose calibrator was used as a data logger and calibrator for pressure sensor response. The calibrator was also used to power up the pressure sensor. A pneumatic pressure pump was used to pressurise the pressure sensor under test. The pneumatic type

of pressure was selected in order to keep the chip isolated from the moisture and vapour particles, which can come from the hydraulic kind of the pressure pump. This was required as the packaging of the developed prototype of pressure sensors did not have stainless steel diaphragm for isolation in between the sensor chip and pressure media. In addition, a high-resolution multimeter was used to precisely measure the bridge resistance of the pressure sensor. Moreover, an in-house designed and developed temperature chamber with the controller was utilised in order to investigate the effect of temperature on the pressure response. The schematic and actual photograph of pressure sensor characterisation setup is presented in Figure 5.1 (a) and (b) respectively.

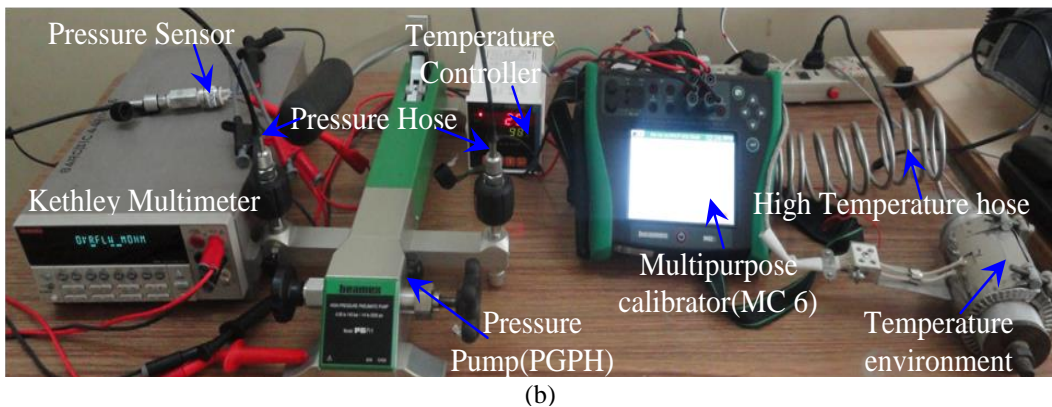
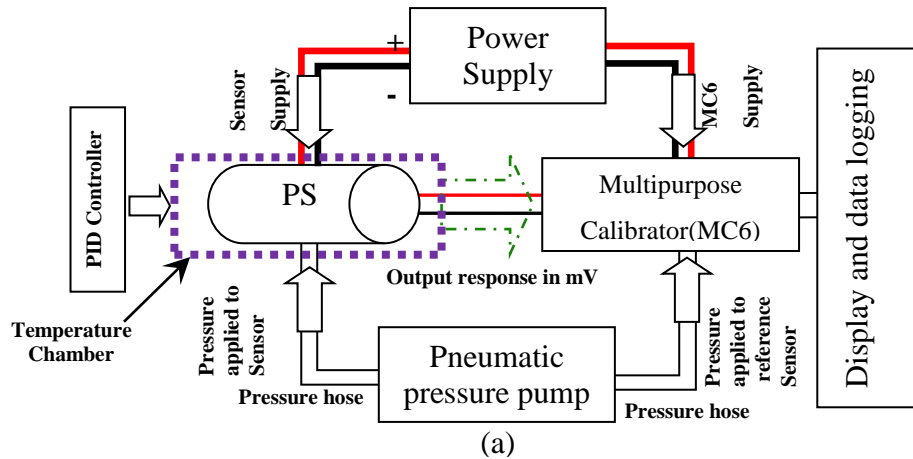


Figure 5.1: (a) Schematic of the pressure sensor characterisation setup, (b) Photograph of experimental setup.

5.3 PERFORMANCE STUDY OF PRESSURE SENSORS FABRICATED DURING PROCESS DEVELOPMENT

The typical performance results for diffused resistor (SNO2) and SOI technology (SLNO5) based piezoresistive pressure sensors at different temperatures are presented in this section.

5.3.1 Pressure response with Offset

The pressure response of diffused resistor and SOI based fabricated piezoresistive pressure sensors was measured at different temperatures and analysed. The temperature induced variation in the response was obtained after subtracting the offset of the pressure sensors. The response of the pressure sensor is shown for diffused and SOI technology based pressure sensor in Figure 5.2 (a) and (b). Since all resistors were not identical, it resulted in a considerable output voltage at no pressure conditions i.e. offset voltage

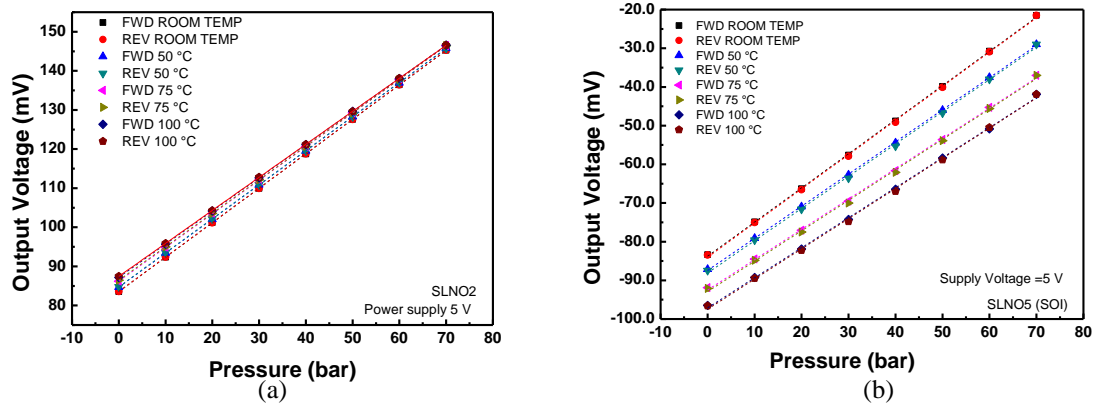


Figure 5.2: Pressure response under the elevated temperatures for (a) Passivated and diffused (SLNO2) and (b) SOI technology based (SLNO5) based pressure sensor with 150 μm diaphragm thickness and 100 bar pressure range.

It is observed that the change in the sensitivity of diffused technology based pressure sensor is less as compared to the SOI technology based pressure sensor. It can be attributed to the higher doping concentration of boron in piezoresistors of diffused type as compared to SOI technology based pressure sensors.

5.3.2 Sensitivity

The sensitivity is defined the slope of the plot between output voltage vs input pressure. Sensitivity of the pressure sensor was observed to degrade by $\sim 4.5\%$ and $\sim 14\%$ for diffused and SOI technology based pressure sensors at $100\text{ }^\circ\text{C}$. The measured and calculated sensitivities using a linear curve fitting (slope) are identical and are 0.088 mV/bar at 5 V supply. The doping concentration of piezoresistors was higher for diffused piezoresistor based sensors than for the SOI wafer based sensors. Hence a lower change ($\sim 4.5\%$) is observed for diffused piezoresistor based pressure sensor compared to SOI wafer based sensor ($\sim 14\%$). The degradation in the sensitivity under temperature for diffused and SOI technology based pressure sensor is depicted in Figure 5.3 (a) and (b) (measured) and Figure 5.4 (a) and (b) (linear fit).

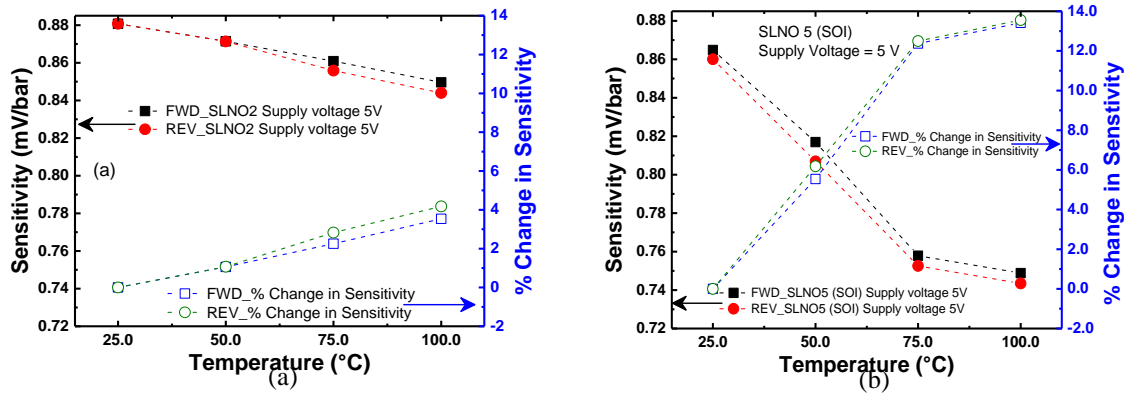


Figure 5.3: Sensitivity and % degradation of sensitivity for pressure sensors (a) Diffused resistor based, and (b) SOI technology based.

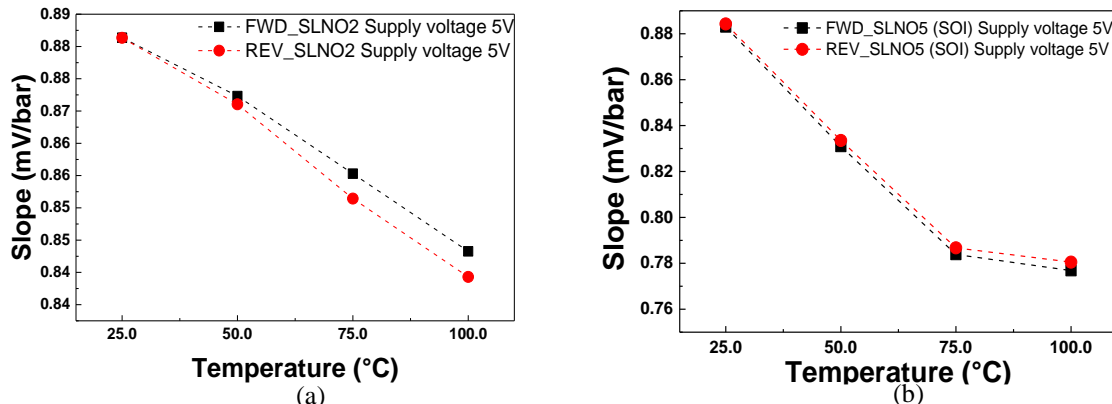


Figure 5.4: Calculated sensitivity (slope fitting) under elevated temperatures from the linear curve for (a) Diffused resistor based and (b) SOI technology based sensor respectively.

SOI wafer based sensors have piezoresistors isolated from the diaphragm by SiO₂ layer. However, since piezoresistive coefficient decreases with increase of temperature, the sensitivity is observed to decrease. Due to hysteresis, the sensitivities are different in forward and reverse characterization for both types of sensors.

5.3.3 Offset voltage

The offset voltage of both pressure sensors was recorded under elevated temperature environments. The maximum degradation was observed as ~5 % and 16 % for diffused and SOI technology based pressure sensors respectively (Figure 5.5 (a) and (b)). Moreover, the offset voltage obtained after linear fitting of the data is plotted as shown in Figure 5.6 (a) and (b).

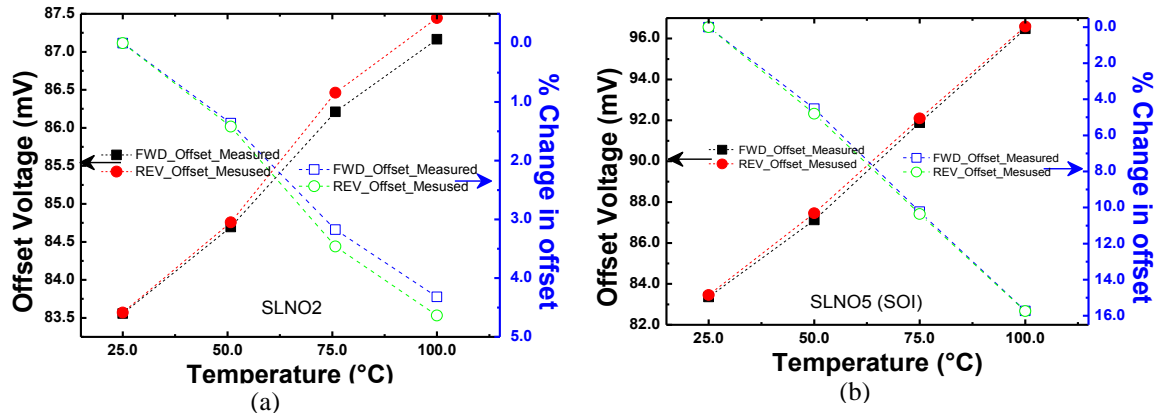


Figure 5.5: Variation in the offset voltage under elevated temperatures for (a) Diffused resistor, and (b) SOI technology based pressure sensor.

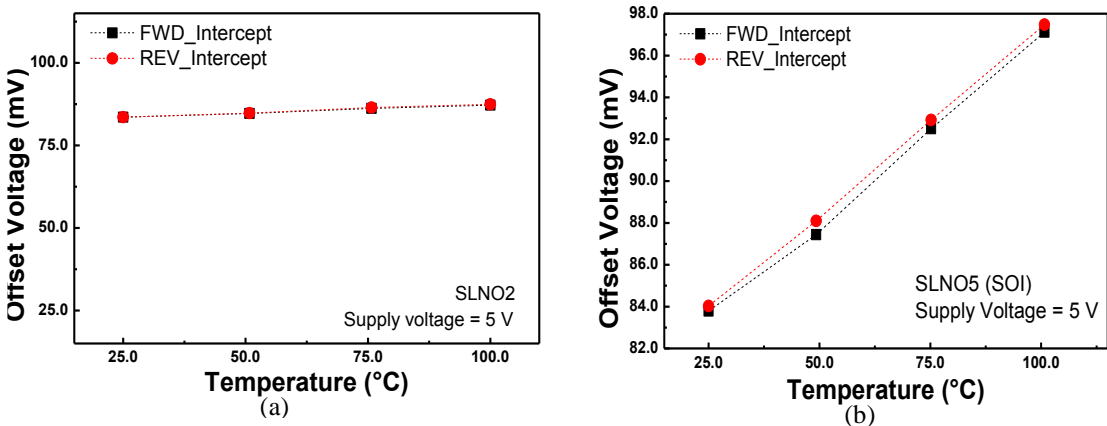


Figure 5.6: Variation in offset voltage under elevated temperatures for (a) Diffused resistor, and (b) SOI technology based pressure sensors using a linear curve fitting.

5.3.4 Offset voltage drift

The drift in offset voltage was also recorded in order to know the stability of the offset voltage at the room temperatures. Offset voltage drift was observed to be maximum of 200 μV . Offset voltage drift is presented in Figure 5.7 (a) and (b) for diffused and SOI technology based pressure sensor respectively.

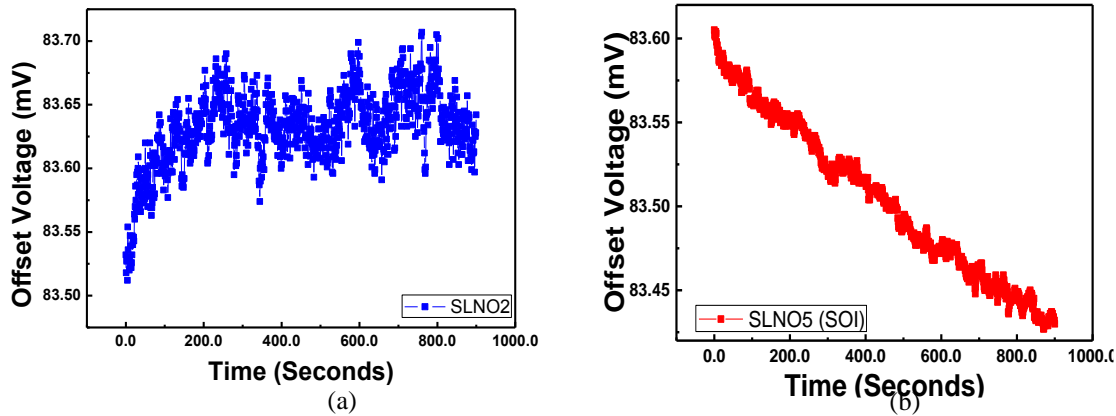


Figure 5.7: Offset voltage drift at room temperatures for 900 seconds for (a) Diffused resistor based, and (b) SOI technology based pressure sensor.

5.3.5 Linearity

R square values obtained by linear curve fitting is a measure of the linearity. The linearity of pressure response was very good i. e. $R^2 \sim 1$. The variation in the linearity under the elevated temperatures was found to be insignificant. The Figure 5.8 (a) and (b) shows the linearity (R^2) for diffused resistor based and SOI technology based pressure sensors.

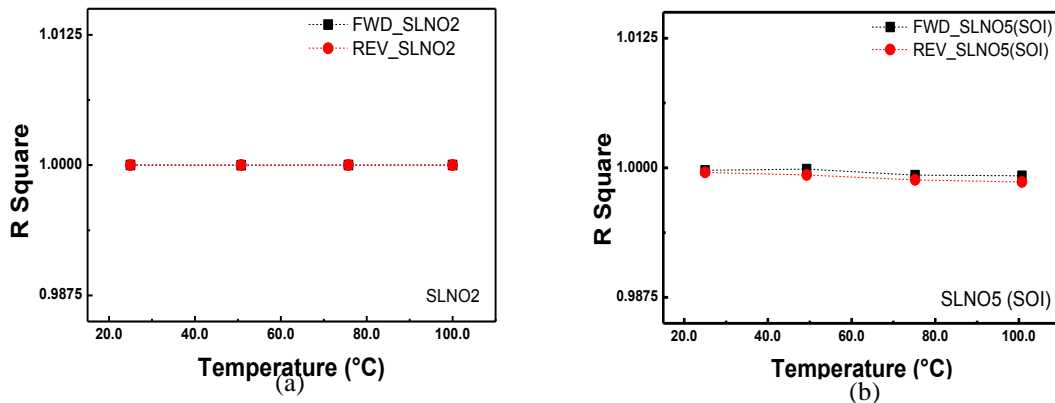


Figure 5.8: Variation in linearity under the elevated temperatures for (a) Diffused, and (b) SOI technology based pressure sensors.

5.3.6 Hysteresis

Hysteresis of the piezoresistive pressure sensors was calculated using the forward and backward pressure response. For each temperature, a forward and backward pressure scan is taken and the hysteresis is calculated from this data. Figure 5.9 (a) and (b) show variation in hysteresis under high temperatures for diffused and SOI technology based pressure sensor respectively.

5.3.7 Resistance vs temperature

The gradual increase in the resistance of the piezoresistors was observed with temperature. The summarised results of change in the resistance under high temperature are presented in Figure 5.10 (a) and (b) for diffused and SOI technology based pressure sensors. The change in the resistance was ~ 6 % and 1.4 % for diffused piezoresistors and SOI technology based piezoresistors respectively.

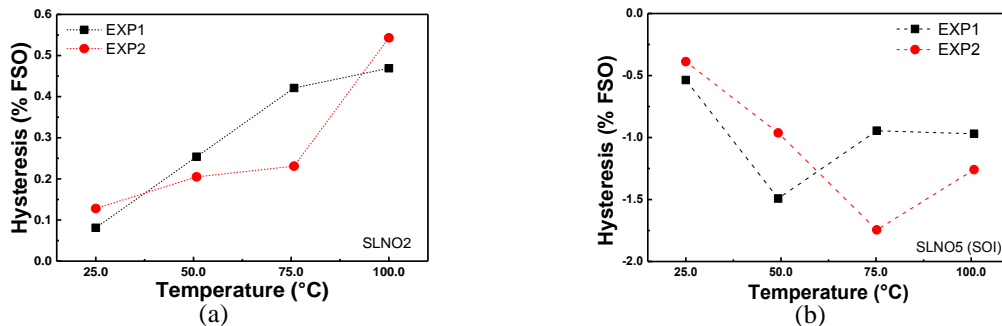


Figure 5.9: Variation of hysteresis under elevated temperatures for (a) Diffused resistor based and (b) SOI technology based pressure sensors.

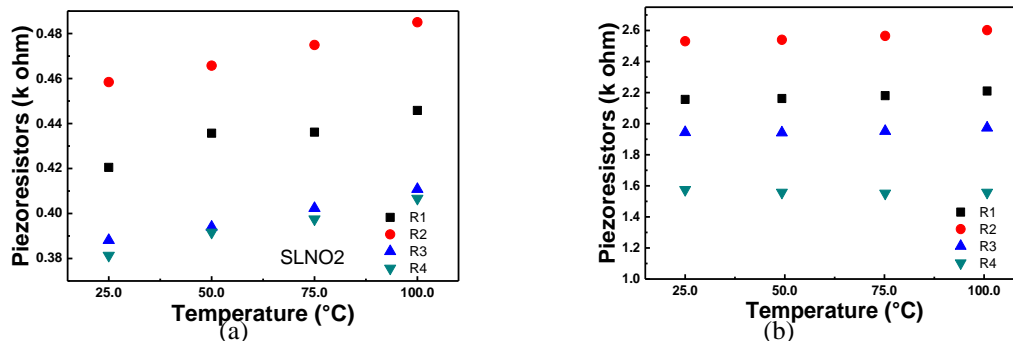


Figure 5.10: Resistance of piezoresistors vs temperature for (a) Diffused piezoresistor, and (b) SOI technology based pressure sensors.

5.4 DIFFUSED AND SOI TECHNOLOGY BASED PRESSURE SENSOR (PRODUCTION BATCH)

The final performance achieved for the production batch of sensors is summarised in this section. For these measurements the diffused resistor based and SOI technology based pressure sensors were characterised from 27 °C to 100 °C (failed after this temperature) and 200 °C respectively. The results are presented in Figure 5.11 and Figure 5.12 respectively.

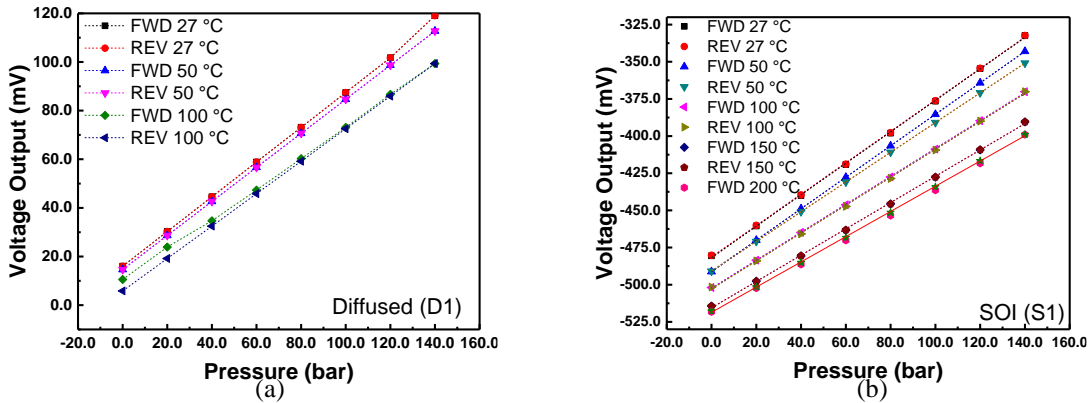


Figure 5.11: (a) Diffused resistor pressure sensor response under elevated temperature up to 100 °C (b) SOI technology based pressure sensor response under elevated temperature up to 200 °C.

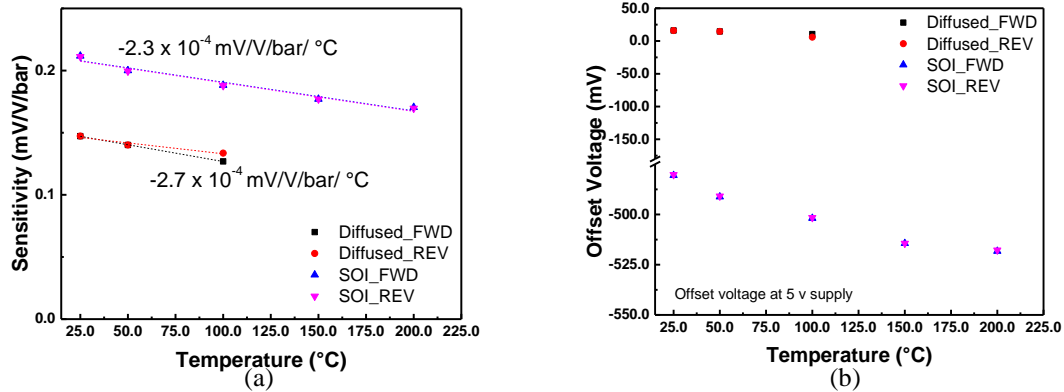


Figure 5.12: (a) Sensitivity and (b) offset voltage under varying temperature for diffused and SOI technology based pressure sensors.

5.5 COMPARISON OF SIMULATION AND EXPERIMENTAL RESULTS

The comparison between simulation results (as presented in Chapter 3) and experimentally obtained pressure response at room temperature and at elevated

temperatures is presented in this Section. At room temperatures, the deviation in the experimentally obtained sensitivity from that obtained through simulation was observed as 13.72 % and 20.94 % respectively for SOI and diffused pressure sensors (Figure 5.13 (a)). The temperature induced degradation in simulated and experimental sensitivities is showing similar trend (Figure 5.13 (a)). The decrease of sensitivity is calculated with respect to sensitivity at room temperatures. For SOI pressure sensor, from 25 °C to 200 °C, the decrease in the pressure sensor sensitivity is observed to be 21% by theoretical simulations and 19% from experimental data (Figure 5.13 (b)). Similarly for diffused piezoresistor based pressure sensors, from 25 °C to 100 °C, the decrease in the pressure sensor sensitivity is observed to be 10 % by theoretical simulations and 14% from experimental data (Figure 5.13 (b)).

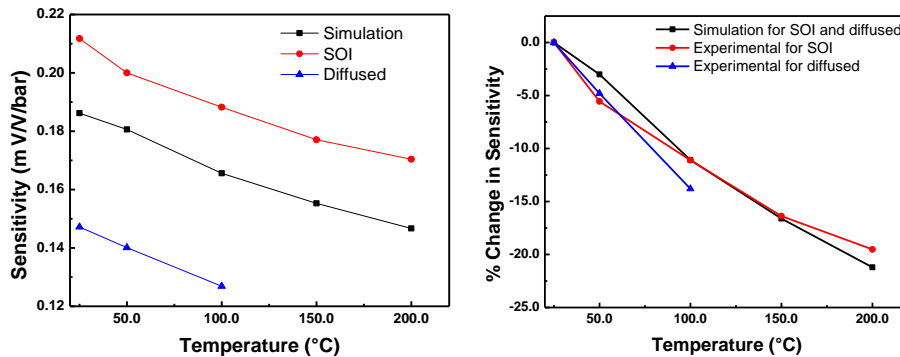


Figure 5.13: (a) Comparison of theoretical (simulated) and experimentally calculated sensitivity of piezoresistive pressure sensors, (b) The % change of the experimentally calculated sensitivity and theoretical sensitivity at various temperatures.

Table 5.1 summarizes the parameters of the pressure sensors obtained at different temperatures based on experimental data and simulated data. It is to be noted that for simulation, the diaphragm and piezoresistor parameters were identical for the diffused and SOI technology based sensors and it was assumed that the thin oxide layer in SOI technology based sensors does not cause any change in the stress distribution. The deviation of the data obtained from simulations to that obtained from experiments is mainly because of variation in the concentration of piezoresistors during fabrication to-

-that assumed for the simulations.

Table 5.1: Summary of performance parameters of production batch of piezoresistive pressure sensors.

Type \longrightarrow	Diffused PZR (D1)		SOI (S1)		Simulated for SOI technology based sensor	
	25 °C	100 °C	25 °C	200 °C	25 °C	200 °C
Sensitivity (mV/V/bar)	0.147	0.127	0.212	0.170	0.186	0.147
Offset (mV)	-16.024	-10.543	-480.56	-518.27		
Hysteresis (% FSO)	0.0543	5.342	0.3089	1.92		
Linearity (R^2)	0.9998	0.999	0.999	0.999		
Range (bar)	200		200		200	200

5.6 SUMMARY

The performance investigation of the prototypes and production batch of designed and developed MEMS based pressure sensors using i) diffused resistor and ii) SOI technology is presented based on the one sample of each types. The performance parameters are investigated in terms of the sensitivity, offset voltage, offset drift, linearity and hysteresis. The developed sensors showed very good linearity, low offset voltage drift and low hysteresis. The effect of elevated temperatures on these parameters was also studied. The pressure sensor sensitivity showed reduction of 13.80 % at 100 °C for diffused piezoresistors and reduction of 19.51 % at 200 °C for SOI technology based pressure sensor. The standard diffused resistor pressure sensor could operate up to maximum temperature of 100 °C, while pressure sensors based on SOI technology could operate at even 200 °C. It can be clearly seen that the SOI technology based process has a clear advantage for extending the operating range beyond that for commercial standard sensors. The investigation of gamma radiation induced degradation of pressure sensors is presented in the next Chapter.

Chapter 6. EXPERIMENTAL INVESTIGATION OF GAMMA RADIATION-INDUCED DEGRADATION OF PIEZORESISTIVE PRESSURE SENSORS

6.1 INTRODUCTION

In the previous chapter, the experimental performance investigation of in-house designed and developed pressure sensors at elevated temperature environment is presented. Several applications demand pressure sensors capable of operating under ionizing radiation environment. A series of experimental investigations were carried out to understand the performance degradation of pressure sensors under the ^{60}Co gamma radiation environment. To study the degradation of pressure sensors due to gamma radiation, various types of sensors were used. The experiments were carried out as given below.

- a. Case I: Pressure sensor packaged with silicone oil and SS diaphragm (developed at an Indian foundry).
- b. Case II: Commercial pressure sensor packaged without silicone oil (part no 13A-250G, Measurement Specialties).
- c. Case III: In-house designed and developed piezoresistive pressure sensors.
- d. Case IV: Irradiation study of pressure sensor chips.

The pressure sensors used for industrial applications are fabricated with a thin SS diaphragm for media isolation. The chip is isolated from the process media by silicone oil and SS diaphragm. Since silicon oil is the most likely part to degrade, the sensors with and without oil were used.

6.2 SCHEMATIC DIAGRAMS OF PACKAGED PRESSURE SENSORS

The gamma radiation-induced degradation of the piezoresistive pressure sensor was investigated by exposing the sensor to gamma radiation in a ^{60}Co chamber. The schematic diagrams of the pressure sensor chip and packaged sensors used for this study are given in (Figure 6.1 (a)-(b)) and (Figure 6.1 (c)-(d)) respectively. In one type of packaging, the sensor comprised of stainless steel (SS) housing with silicone oil filled and thin SS diaphragm in order to isolate silicon chip from the external sensing medium. The details of chip design and packaging such as silicon diaphragm geometry, piezoresistor geometry and doping, SS diaphragm thickness and silicone oil, etc., were not known from the manufacturer for commercial sensor. The second type of packaging was without silicone oil and package housing was made using nickel alloy material. The pressure sensor chip was directly exposed to the pressurising media. The radiation induced degradation of the in-house designed and developed piezoresistive pressure sensor was also studied which had a package without oil filling. To understand the radiation hardness of the fabricated chips, this study was carried out. Additional results are also obtained by studying the radiation hardness of fabricated packaged sensors.

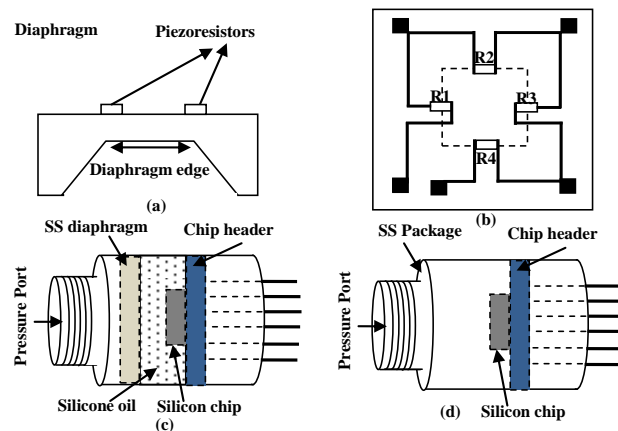


Figure 6.1: Schematic diagram of the pressure sensor; (a) Cross section of the sensor chip, (b) Top view showing piezoresistors over the diaphragm, (c) Packaged sensor-Case I and (d) Packaged sensor-Case II.

Prior to gamma exposure, pressure response of the sensor was measured using the experimental setup the details of which are already presented in the previous Chapter. For studying the gamma radiation effect, the pressure sensor was kept in a ^{60}Co chamber for specific durations corresponding to the required dose. Since, in-situ characterisation was not feasible, the sensor was taken out from the irradiation chamber for characterisation of pressure response in between the irradiations. The characterisation results are summarised in subsequent sections.

6.3 RESULTS AND DISCUSSION

6.3.1 Case I: Commercial packaged pressure sensor with silicone oil

The pressure sensor response was evaluated in terms of sensitivity, offset voltages, linearity and hysteresis for various total doses of gamma radiation. In addition, the bridge resistances were measured for various total dose exposures in order to verify if there is any change in the resistor values. The measurements with gamma radiation exposure were carried out up to the total dose of 40 Mrads at which the permanent failure of the pressure sensor was observed. The results are presented and discussed in next subsection.

6.3.1.1 Response of pressure sensor after irradiation under increasing and decreasing pressure

The pressure sensor response in terms of output voltage for various input pressures was measured using pressure sweep measurements. The pressure was increased from zero to 50 bar (forward sweep) and then decreased from 50 bar to zero again (backward sweep). The data recorded is plotted in Figure 6.2 and Figure 6.3 respectively.

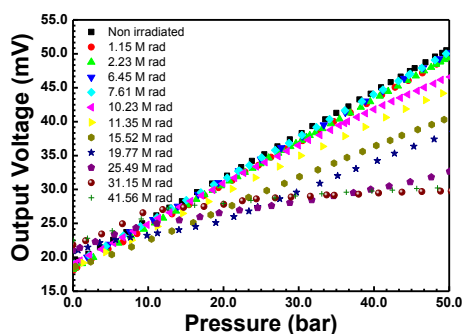


Figure 6.2: Forward sweep measurements showing pressure sensor performance with total gamma dose.

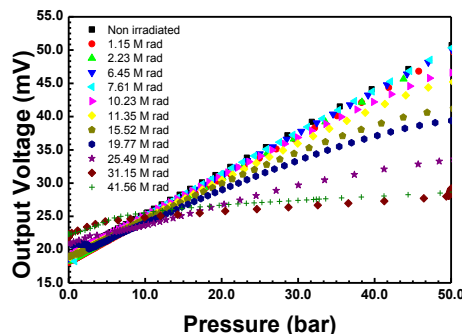


Figure 6.3: Backward sweep measurements showing pressure response with total gamma dose.

The plots obtained at various total dose exposures show that there is a significant decrease in output response (voltage) with an accumulated dose of gamma radiation for forward and the backward sweep measurements. It can be seen that the degradation of pressure sensor response is significant after total dose exposure of 10 Mrads. Moreover, a small increase in the offset voltage with the increase of accumulated gamma dose is also observed for the forward and backward sweeps. The comparison of the data presented in Figure 6.2 and Figure 6.3 indicate that after gamma radiation exposure, the response of pressure sensor for increasing pressures and decreasing pressures is not identical due to hysteresis. Using data plotted in Figure 6.2 and Figure 6.3, the pressure sensor response for various total doses of gamma radiation was examined at a 50 bar applied pressure (Figure 6.4). The reported literature shows that the observed degradation is sample dependent. It is observed that there is no significant decrease in the output voltage up to a total dose of 10 Mrads and subsequently the pressure sensor demonstrate a rapid degradation. Beyond total dose exposure of 30 Mrads, the percentage decrease in the pressure sensor output voltage is about 75 %. The sensitivity of the pressure sensor was calculated by fitting a straight line to the output voltage vs pressure plot at different gamma doses. The sensitivities obtained at various total doses are plotted in Figure 6.5 for forward pressure scans.

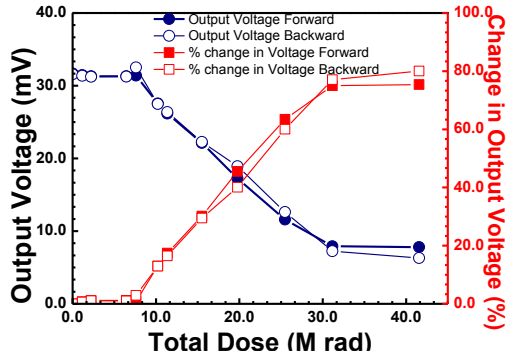


Figure 6.4: The output voltage response at 50 bar and the percentage change in the output voltage of the piezoresistive pressure sensor due to total gamma dose.

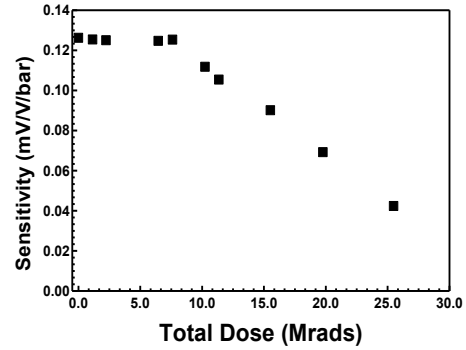


Figure 6.5: Changes in the sensitivity of the piezoresistive pressure sensor (in mV/V/bar) with total gamma dose.

The pressure sensor sensitivity decreased for the non-irradiated sensor from ~ 0.125 mV/V/bar to ~ 0.05 mV/V/bar for the 25 Mrad irradiated sensor. For total doses higher than 25 Mrad, the output voltage vs pressure plot was highly nonlinear. Hence, sensitivity is not be extracted using straight line fitting for higher total doses exceeding 25 Mrads.

6.3.1.2 Linearity of response

As the response of the pressure sensor is theoretically expected to be linear with the input pressure, the data plotted in Figure 6.2 was fitted using a linear fitting. The obtained R^2 values (a measure of linearity) were in the range of 0.98 to 1.0 for total doses up to 25 Mrads. However, for total doses exceeding this dose, the pressure sensor response could not be fitted to a straight line. For lower gamma doses up to 30 Mrads, the pressure sensor shows nonlinear behaviour in terms of reduced output voltage for higher input pressures exceeding about 40 bar and for lower input pressures, the response was linear. However, for total doses exceeding 30 Mrads, the pressure sensor shows drastic reduction in output voltage with a highly non-linear response.

6.3.1.3 Offset voltage

The offset voltages obtained from the data presented in Figure 6.2 and Figure 6.3 at different gamma doses are plotted in Figure 6.6. The plot shows a trend of increasing

offset voltage after exposure to a total dose of 15 Mrads.

6.3.1.4 Hysteresis loop

Due to gamma radiation exposure, the pressure sensor shows hysteresis of pressure response, i.e. the output at a specific applied pressure is not identical for increasing and decreasing applied pressures. It was observed that prior to irradiation the pressure sensor did not exhibit any hysteresis. However, as shown in Figure 6.7, the hysteresis increases with total dose exposure.

6.3.1.5 Wheatstone bridge resistance measurement

In order to study if there is any variation of the magnitude of bridge piezoresistors, the piezoresistors were measured using a digital multimeter. The measured values of piezoresistors for various total dose exposures are presented in Figure 6.8. The average magnitudes and standard deviation of four piezoresistors from the data plotted in Figure 6.8 were calculated. The piezoresistors do not show any significant change due to gamma exposure and the standard deviations are within 1%.

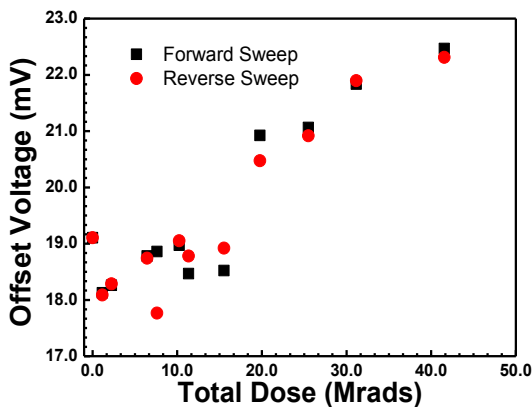


Figure 6.6: Offset voltage variation as a function of total gamma dose.

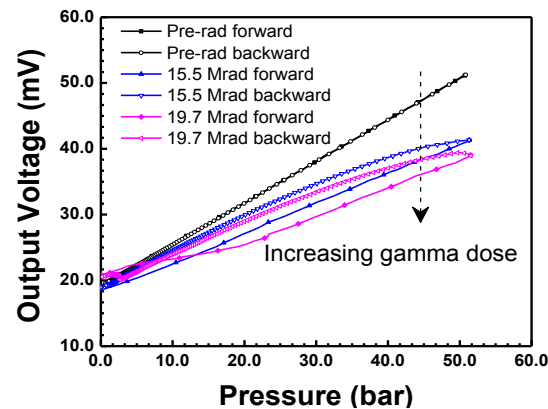


Figure 6.7: The hysteresis observed in the pressure response due to total gamma dose.

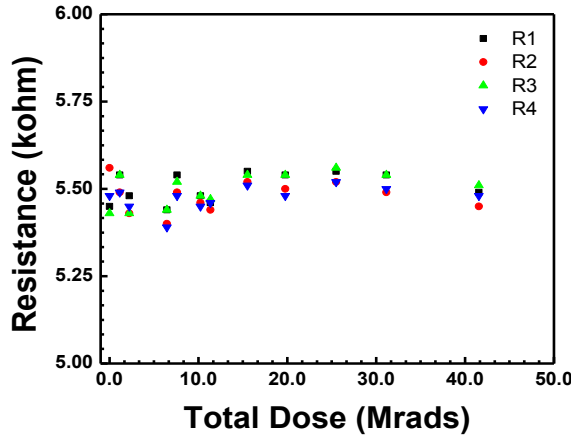


Figure 6.8: The variation of Wheatstone bridge resistances with total gamma dose.

The packaged piezoresistive pressure sensor used in this study can be considered as a complex system comprising SS housing, SS diaphragm, silicone oil, and a pressure sensor chip. Since the piezoresistors did not show significant degradation up to studied dose of 40 Mrads, the observed degradation of the sensor could be attributed to the degradation of the silicone oil which is used as a pressure transmitting media.

6.3.2 Case II: Commercial pressure sensor without silicone oil

In order to understand, further, the mechanism of the sensor failure, a packaged piezoresistive pressure sensor without silicone oil and SS diaphragm with operating range up to 17 bar was selected for the study. In this case, pressure sensor chip is directly exposed to the pressure media. The results of this study are presented in this subsections.

The change in the response of pressure sensor is mainly observed due to offset voltage changes under the increased total dose of the gamma radiation (Figure 6.9). The offset of the pressure sensor increased with increasing cumulative dose of ^{60}Co . The change in the offset is observed to be about 26 % and 139 % at a gamma irradiation dose of 3.83 Mrad and 27.92 Mrad respectively (Figure 6.10). Under the influence of gamma radiation, ionization takes place led to charge separation near the junction and hence change in thickness of the piezoresistors led to change in the offset voltage [55].

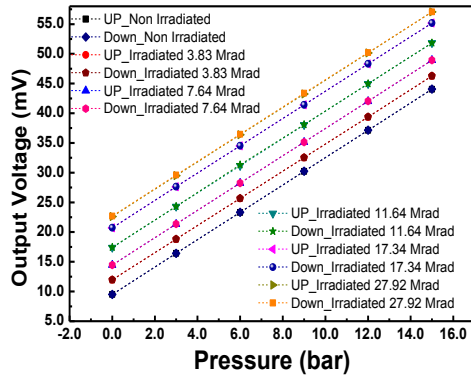


Figure 6.9: Output voltage vs applied pressure with varying irradiation dose.

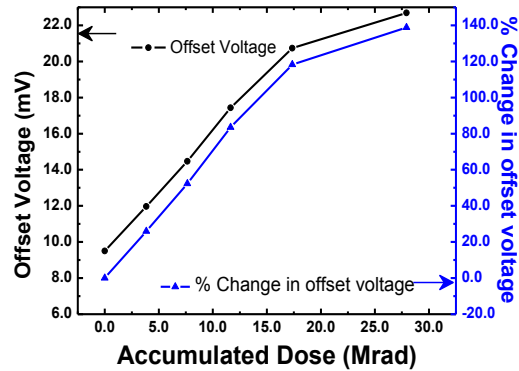


Figure 6.10: Change in offset voltage as a function of accumulated gamma dose.

The sensitivity and hysteresis of the sensors response was examined at various total doses. The hysteresis was negligible (Figure 6.11) and the sensitivity did not show significant degradation (Figure 6.12). Mechanical material properties of silicon are not expected to degrade at this dose and there is no significant change in resistance recorded with gamma exposure, therefore no effect in the sensitivity and hysteresis were observed.

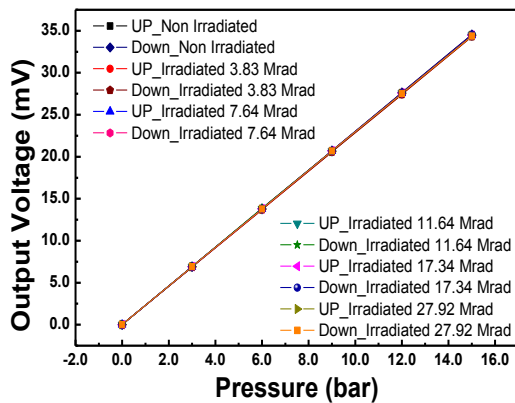


Figure 6.11: Output voltage vs applied pressure with varying irradiation dose without offset.

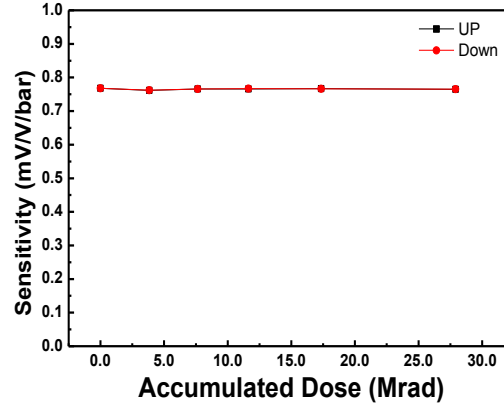


Figure 6.12: Sensitivity vs accumulated dose for commercial pressure sensor.

The resistance of all piezoresistors were obtained by measuring the IV characteristics. The summarised IV response is plotted in Figure 6.13.

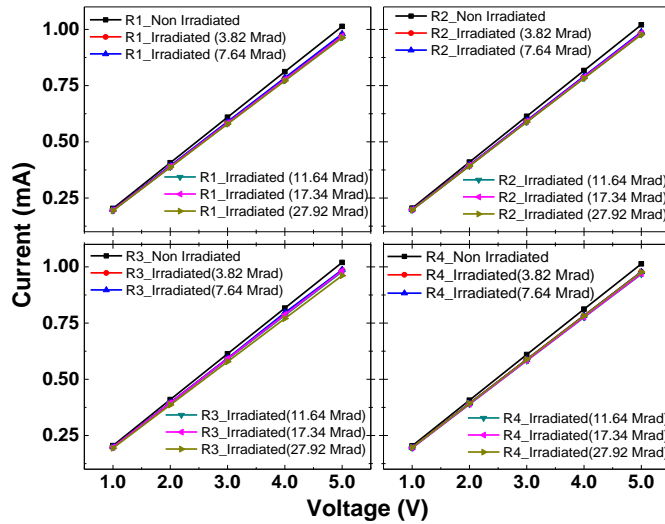


Figure 6.13: Measured IV characteristics of piezoresistors at different total doses.

The change in the resistance of piezoresistor is calculated with increasing cumulative dose of ^{60}Co radiation shown in Figure 6.14. The change in the resistance of piezoresistors is observed to about 3.5 % and 5 % at 3.38 Mrad dose and 27.92 Mrad respectively.

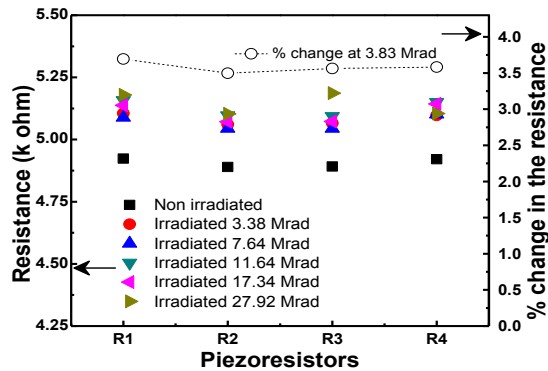


Figure 6.14: Change in the resistance with increasing cumulative dose of the ^{60}Co radiation.

6.3.3 Case III: Irradiation of in-house designed and developed pressure sensors

The experimental investigation of gamma radiation-induced degradations of in-house designed and developed piezoresistive pressure sensors is presented in this section. The sensors were irradiated in a ^{60}Co radiation chamber with a dose rate of 162 krad/hr. As

the in-situ characterization of piezoresistive pressure sensors under gamma exposure was not feasible, the sensors were irradiated for a pre-determined time interval and were then subsequently taken out of the chamber for the measurements. The performance of the sensors in terms of sensitivity, offset voltage and hysteresis was measured after successive total dose exposures. The pressure response of all three types (i.e. diffused piezoresistors, poly silicon and SOI technology) of sensors up to a maximum pressure of 100 bar is plotted in Figure 6.15.

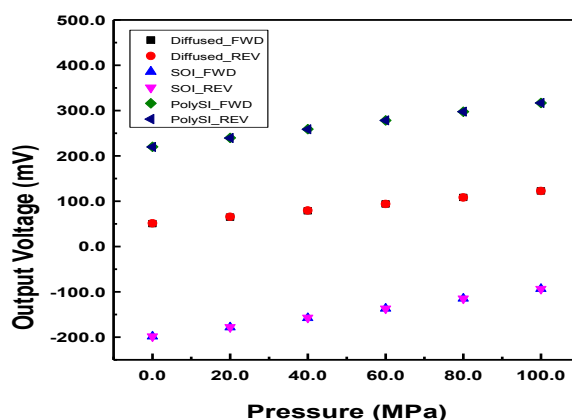


Figure 6.15: Pressure response of all types of pressure sensors measured at room temperature up to 100 bar. In the case of diffused resistor based and polysilicon piezoresistor based sensor, diffusion process was used for doping the resistors. This process causes more nonuniformity of doping compared to the process of ion implantation. Also wet etching was used for defining the resistors. Hence the four resistors were not very uniform in magnitudes resulting in higher offset voltages. However, the linearity of the response as measured from the coefficient of determination (R^2) was very good. The performance parameters of these pressure sensors calculated from the data presented in Figure 4 are summarized in Table. Though the geometrical parameters of the diaphragms were the same for diffused piezoresistor and SOI wafer based sensors, the sensitivities are different due to the differences in the doping concentration of the piezoresistors.

Table 6.1: Performance parameters of the pressure sensors of different types

Type of pressure sensor	Sensitivity (mV/V/bar)	Linearity (R ²)	Offset voltage (mV)	Hysteresis (%)
Diffused piezoresistor based	0.143	0.999	50.53	0.051
SOI wafer based	0.209	1.0	-198.40	0.0057
Polysilicon piezoresistor based	0.193	1.0	220.24	0.614

All three types of pressure sensors withstood the total gamma dose of 30 Mrad (Si) without exhibiting failure.

The variation of pressure response with gamma dose for diffused piezoresistor based pressure sensor is shown in Figure 6.16.

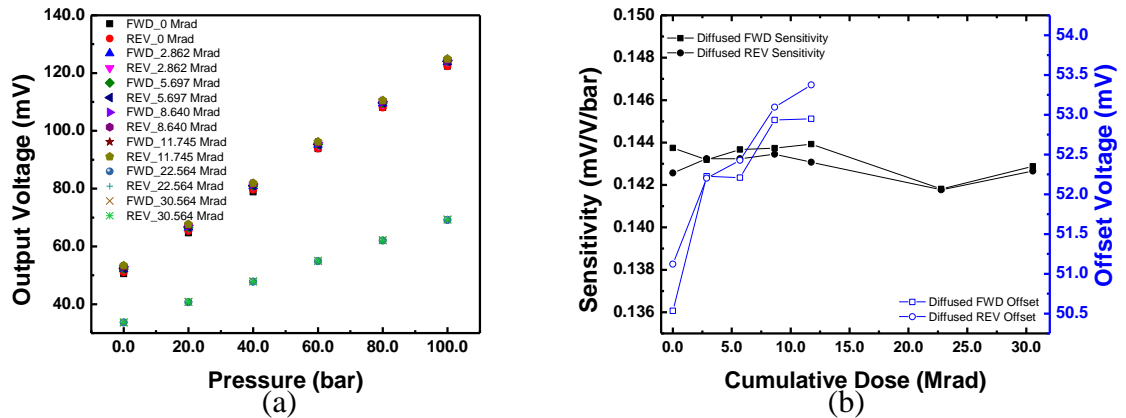


Figure 6.16: (a) Response of diffused piezoresistor based pressure sensor after various gamma dose exposures. The data points for total dose irradiation of 22.56 Mrad(Si) and 30.56 Mrad(Si) (indicated as 'half bridge output') were obtained by measuring the half bridge output. The half bridge output data was doubled for comparison with output voltage data for irradiation up to the total dose of 11.74 Mrad(Si) (b) Sensitivity and offset voltage variation for diffused piezoresistor based pressure sensor after various gamma dose exposures.

One of the leads of the pressure sensor was accidentally broken during connections in the experimentation. Hence, instead of full bridge output, the half bridge output was measured. The sensitivity was calculated by doubling the half bridge output. However, the offset voltage variation could not be recorded beyond the cumulative dose of 11.75 Mrad(Si). As can be observed from Figure 6.16 (a), the diffused piezoresistor based pressure sensor shows a small change in the sensitivity with increased exposure of

cumulative gamma dose. The sensitivity and offset voltage were estimated using the data presented in Figure 6.16 (a) for a quantitative estimation of the changes of these parameters with gamma dose. This analysis is summarized in Figure 6.16 (b). Under the cumulative exposure of gamma dose up to 30 Mrad(Si), the change in the sensitivity was observed to be 0.6%. The change of offset voltage was about 5% after cumulative gamma exposure up to 11.75 Mrad(Si). However, the linearity was not affected by the gamma irradiation and the coefficient of determination R^2 obtained after linear fitting, was found to be ~ 1 , for all doses of gamma exposure.

The response of the SOI wafer based pressure sensor after various gamma dose exposures is shown in Figure 6.17 (a). The changes in sensitivity and offset voltage at different total dose gamma exposures are plotted in Figure 6.17 (a). Contrary to diffused piezoresistor based sensor, the SOI wafer based pressure sensor shows an increase in the sensitivity of about 13% at 30 Mrad(Si) exposure (Figure 6.17 (a)). As can be seen from Fig. 8, the changes in the sensitivity are gradual up to the exposure of 10 Mrad(Si) and are rapid for higher doses.

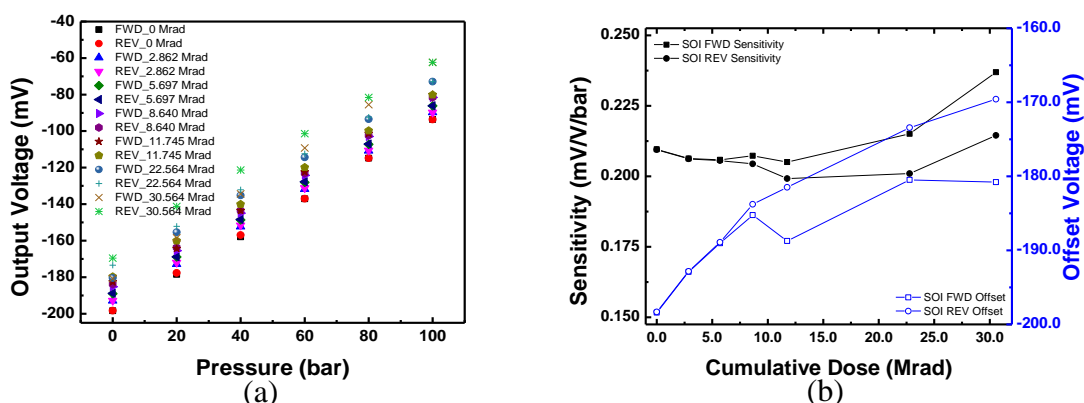


Figure 6.17: (a) Response of SOI wafer based pressure sensor after various gamma dose exposures. The plots indicate observable changes in sensitivity and offset voltage due to gamma irradiation (b) Sensitivity and offset voltage variation of the SOI wafer based piezoresistive pressure sensor after various gamma dose exposures. The plots indicate that degradation of sensor is rapid after total dose exposure of 10 Mrad(Si).

The polycrystalline piezoresistor based pressure sensor showed the best performance in terms of gamma radiation hardness. As depicted in Figure 6.18 (a), the pressure response

shows an insignificant change after total gamma dose exposure of 30 Mrad(Si). Based on the data plotted in Figure 6.18 (a), the estimated change in the sensitivity and offset voltage are plotted in Figure 6.18 (b). For the gamma exposure up to 30 Mrad(Si), the observed change in the sensitivity is about 0.56%. The offset voltage shows a small decrease of 0.5% at 30 Mrad(Si) (Figure 6.18 (b)).

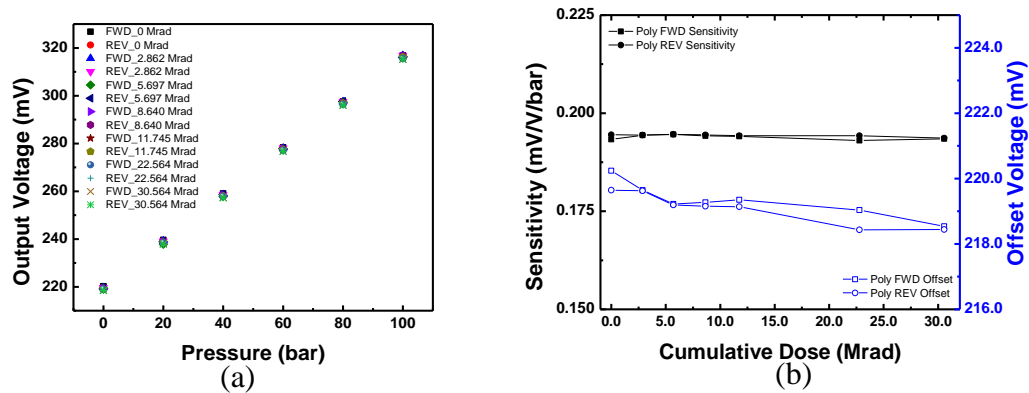


Figure 6.18: (a) Response of the polysilicon piezoresistor based pressure sensor after various gamma dose exposures. All data points for total dose irradiation up to 30.56 Mrad(Si) overlap indicating a negligible change in the sensor response (b) Sensitivity and offset voltage variation for the polysilicon piezoresistor based pressure sensor after various gamma dose exposures. The plots indicate that there is negligible change in the sensitivity and a small change in the offset voltage

The comparison of the performance of three types of pressure sensors in terms of the variation of sensitivity, offset voltage and hysteresis is presented in Figure 6.19 (a), (b) and (c) respectively. The variation of sensitivity, offset voltage and hysteresis after the total dose exposure of 30 Mrad(Si) for the three types of sensors is presented which shows that the diffused piezoresistor based sensor and polysilicon piezoresistor based sensor exhibit about 0.6% of degradation in the sensitivity while the degradation for SOI wafer based sensor was much higher i.e.13%. Considering all performance parameters, the polysilicon piezoresistor based sensor demonstrates the best radiation hardness.

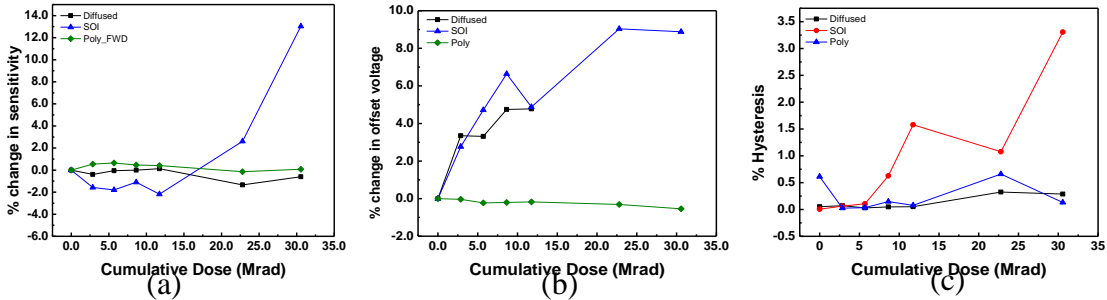


Figure 6.19: (a) Comparison of the variation in the sensitivity of pressure sensors as a function of gamma dose exposure (b) Comparison of the offset voltage variation of pressure sensors as a function of gamma dose exposure (c) Comparison of the hysteresis variation of pressure sensors as a function of gamma dose exposure.

6.3.4 Case IV: Irradiation study of piezoresistors under ⁶⁰Co exposure

In order to observe the effect of radiation, the preliminary characterisation study was done under the varying radiation dose on the pressure sensor dies. The bare chip degradation was studied to see if there is any change in the resistance of piezoresistors. It is found that there is no significant change in the resistance of Wheatstone bridge resistors due to total dose of 2.5 Mrad, shown Figure 6.20 and Figure 6.21.

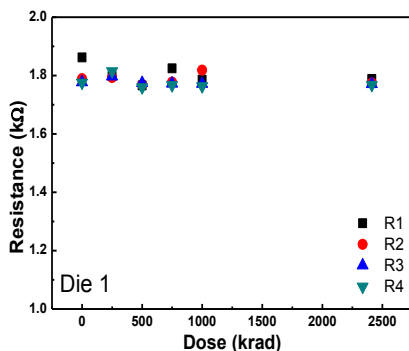


Figure 6.20: Resistance variation with irradiation dose for Die 1.

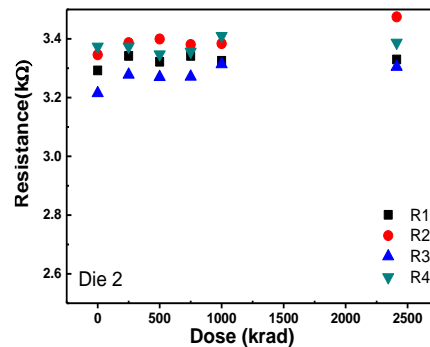


Figure 6.21: Resistance variation with irradiation dose for Die 2.

6.4 SUMMARY

The effect of gamma radiation on the piezoresistive pressure sensors was experimentally investigated for various types of packaged pressure sensors and chips. The radiation-induced degradation of the properties of individual elements and their combined effect would govern the total degradation of the pressure sensor. An abrupt failure of the

pressure sensor was not observed. There was a gradual degradation with total gamma dose and there was no significant change of the piezoresistors resistance magnitude. The sensor packaged with silicone oil and a thin SS diaphragm as isolation media is a very complex system involving mechanical, microelectronics and fluidic parts [110]. The pressure is applied to the SS diaphragm and is transmitted to the silicon membrane through the silicone oil. Hence, the changes in the sensor performance in terms of sensitivity, offset voltage and hysteresis observed could be attributed to a combined effect of the degradation of i) mechanical properties of the silicon diaphragm, ii) electronic properties of piezoresistors, iii) compressibility of the silicone oil medium and iv) mechanical properties of SS isolation diaphragm. For a sensor without silicone oil, the change in the offset voltage is observed. However, the change of the sensitivity of pressure sensor is insignificant under the high cumulative dose. Therefore, it can be concluded that degradation in the sensitivity of case I sensor is due to degradation in material properties of the silicone oil. This has been concluded from the two sets of experiments which were carried out using sensors packaged with and without silicone oil. To know the degradation of silicone oil properties, further studies would be required.

Three types of pressure sensors were fabricated using different processes. The SOI wafer based and polysilicon piezoresistor based pressure sensors incorporated a silicon dioxide layer for isolation of piezoresistors from the bulk diaphragm. These device structures were selected for enhancing the operating temperature beyond 125°C which is the limit for diffused piezoresistor based pressure sensors. The effect of gamma radiation on these sensors was experimentally investigated using ^{60}Co radiation up to a total dose of 30 Mrad(Si). A small change (insignificant) in the sensitivity was observed for the diffused and polysilicon based pressure sensors. Comparatively, the SOI wafer based pressure

sensor showed higher degradation in the sensitivity. This experimental analyses are presented based on the one sample of each type pressure sensors. Moreover, the resistance variation with gamma dose was not observed significantly for separately irradiated piezoresistor chips. This indicates that the packaging of the sensor needs to be further studied.

Chapter 7. CONCLUSIONS

Piezoresistive pressure sensors find broad applications in various fields such as process control, automotive, aviation & aerospace, medical, nuclear power plant etc. Due to junction leakage, the operating temperature of commercial sensors is limited to 125 °C. Several applications of these sensors in industries such as oil, automotive, space, nuclear reactors, etc., demand pressure sensors operating at higher temperatures. In addition, sensors used in ionising radiation environment such as that of a nuclear reactor needs to have required radiation hardness. Hence, research efforts are required to extend the operating temperature of piezoresistive pressure sensors beyond 125 °C and to understand ionising radiation effect on the sensors. The work carried out in this thesis involved design, optimisation and fabrication of the piezoresistive pressure sensor with a focus on high-temperature operation and gamma radiation effect study. The outcome of research is summarised below.

7.1 SUMMARY OF RESEARCH WORK

The effect of various design parameters on the mechanical and electrical response of piezoresistive pressure sensors was studied using FEM simulations. The variation of the deflection and induced stress as a function of thickness or diaphragm size were observed to be as expected. The location of the piezoresistors on the diaphragms was optimised to obtain a maximum sensitivity of pressure response. The change of pressure response at different temperatures was investigated by providing temperature variation of mobility in the doped piezoresistors and change of piezoresistive coefficient with temperature as input parameters to the simulator. Moreover, a quantitative analysis of the temperature effect on piezoresistive pressure sensor response for operation at 200 bar, 200 °C was

presented. A quantitative study of the response of pressure sensors based on high band gap materials such as SiC and diamond has been carried out

Based on the FEM simulation study, the mask design of the pressure sensor was finalized in order to fabricate the mask for processing of wafers for piezoresistive pressure sensors. Two processing options i.e. diffused piezoresistors and SOI technology based, were used for the fabrication. Since the SOI based process incorporates piezoresistors above the insulating oxide layers, the problem of junction leakage as observed for diffused piezoresistor based sensors at higher operating temperatures is overcome in this process. For processing the output of Wheatstone Stone bridge circuit, a suitable signal condition circuit was also designed and fabricated. The circuit compensates offset voltage and provides 4-20 mA response. The performance of this circuit was validated with a commercial pressure sensor.

The performance investigation of the designed and developed MEMS technology based pressure sensors with diffused piezoresistors and SOI technology was presented. The performance parameters were investigated in terms of the sensitivity, offset voltage, offset drift, linearity and hysteresis. The developed sensors showed very good linearity ($R^2 \sim 1$), low hysteresis ($< 0.5\%$ FSO). The effect of the temperature on the sensitivity of pressure sensors was also studied. SOI technology based sensors were demonstrated to operate at temperature of 200 °C. The experimental and simulation studies under the elevated temperature were carried out and comparisons were made between the data obtained through simulations and through experiments. The experimental sensitivities of SOI and diffused pressure sensors showed deviation of 13.72 % and 20.94 % from the theoretically estimated sensitivities respectively. This is mainly because the doping concentration of piezoresistor in the fabricated sensors was not the same as was assumed

for theoretical simulation study. For SOI pressure sensor, it was observed that the change in the sensitivity from 25 °C to 200 °C obtained from simulation data was 21 % and from experimental data was 19%.

The ionising radiation-induced effects on piezoresistive pressure sensors were studied by irradiating the sensors with ^{60}Co gamma radiation for various total doses. This study was performed with different type sensors i.e. sensors without or with oil as an isolation medium. Only dies of pressure sensor chips were also irradiated in order to see if there is any degradation in the electrical parameters. The commercial pressure sensor with oil isolation medium showed an insignificant change in the performance up to total gamma doses of 10 Mrads. However, beyond this dose, the sensor exhibited degradation of various parameters such as decrease of sensitivity, increased hysteresis, increased non-linearity of response and a marginal increase of offset voltage. The study of commercial pressure sensor without silicone oil isolation media did not show significant degradation. From these studies, it was concluded that the degradation of the commercial pressure sensors is mainly due to degradation in the material properties of the silicone oil. A study was also carried out to investigate the irradiation effect on the in-house designed & developed piezoresistive pressure sensors, which are fabricated in the initial batches in the present work. A significant change in the sensitivity and offset 1.93 mV (~12.47 %) were observed for the diffused pressure sensors for a total dose of 27.92 Mrad. The results indicated that further studies would be required for understanding the radiation effect on these sensors.

7.2 HIGHLIGHTS OF THE RESEARCH WORK

The main contributions of this thesis are summarized below:

- a. An extensive simulation study for the optimisation of the diaphragm and piezoresistor design parameters for pressure sensor has been presented.
- b. A quantitative simulation study of the piezoresistive pressure sensors using the wide bandgap materials such as diamond and SiC is presented for estimating the response of the piezoresistive pressure sensors based on these materials. Such sensors would be suitable for high temperature and high radiation environments.
- c. Complete mask design, fabrication process and performance evaluation of fabricated sensors based on diffused piezoresistor and SOI technology based pressure sensors have been presented. Temperature response of the fabricated pressure sensors has been evaluated.
- d. A signal conditioning circuit has been designed and developed for processing of the Wheatstone bridge circuit output into 4-10 mA current output.
- e. Ionizing radiation-induced degradation of sensor chips and packaged sensors with or without isolation oil medium were studied using ^{60}Co gamma.

7.3 FUTURE SCOPE

- a. Fabrication of pressure sensors using diamond or SiC as piezoresistor and diaphragm materials can be done based on the quantitative analysis presented in this work.
- b. The radiation-induced degradation mechanisms in diffused resistor and SOI based pressure sensors can be studied in detail. The degradation due to isolation medium such as silicone oil needs to be separately investigated to identify the mechanism of degradation.
- c. The digital compensation technique can be adopted to balance the offset voltage and sensitivity changes due to elevated temperatures.

- d. The SOI wafer based and polysilicon piezoresistor based pressure sensors developed in the present work showed operation without failure up to the studied temperature of 200 °C. The main problem observed during fabrication was the uniformity of piezoresistors which resulted in a large offset. A ion implantation based process and good dimensional conformance of piezoresistor would be required for reducing this offset. The technology developed will be utilized for commercialization using a suitable industrial foundry in India.

Appendix A. MATHEMATICAL MODELLING OF PRESSURE SENSORS

In this section, the mathematical modelling of piezoresistive pressure sensors is explained using the theory of thin plates as published in the literature. The mathematical modelling of diaphragms of different geometries such as rectangular and square are considered. In addition, the theory of piezoresistivity in silicon and polysilicon, temperature effects on piezoresistivity of a single crystalline silicon are also discussed. The theory for the electrical response of piezoresistive pressure sensors based on Wheatstone bridge configuration is presented.

A.1 BASICS OF APPLIED PRESSURE

Prehistorically, the pressure sensors were known as strain gauges for several decades. Thereafter, the era of micromachined sensors was started for sensor developments based on various transduction techniques. The piezoresistive pressure sensors are among the first MEMS devices based on the silicon material. The pressure is a physical quantity which is defined in terms of force applied perpendicular to the unit area. Mathematically, pressure is defined as in equation (A.1),

$$P = F/A \quad (\text{A.1})$$

Where F is a force applied and A is cross-section area.

The static pressure is defined as in equation (A.2),

$$P_S = P_a + \rho_d gh \quad (\text{A.2})$$

Where P_a is atmospheric pressure, $\rho_d gh$ is hydrostatic pressure, ρ_d is the density of the fluid/gas, h is height, g is an acceleration due gravity at the place of measurement.

Total pressure is the summation of static and dynamic pressure given as in equation (A.3),

$$P_T = P_S + P_D = P_S + \frac{1}{2}\rho_d V_l^2 \quad (\text{A.3})$$

Where, P_T is total pressure, P_S is static pressure, P_D is dynamic pressure, ρ_d is density and V_l is velocity of pressure media.

Pressure sensors are utilised to measure the pressure of gases or liquids, which is a very crucial physical parameter for industrial applications. In addition, measured pressure can be used to derive other parameter indirectly such as fluid/gas flow, water level, altitude, force, etc. The pressure sensor design optimisation is dependent on the type of transduction mechanism and application requirements. A piezoresistive pressure sensor consists of a thin diaphragm and implanted/diffused piezoresistors integrated with the thin diaphragm. The electrical output of piezoresistive pressure sensor is governed by mechanical response of diaphragm (deflection or induced stress). Therefore, thin plate theory and piezoresistivity are discussed in details in the next sections.

A.2 THIN PLATE THEORY

A piezoresistive pressure sensor operates on the principle of converting the induced stresses into the desired electrical signal by means of Wheatstone bridge configuration of piezoresistors. The thin diaphragm with square or rectangular geometries are adopted for most of the applications. The deflection and induced stresses of diaphragm under the applied pressure is modelled using thin plate theory. A thin plate is a uniform flat structure that is confined by two parallel horizontal planes, called faces. Four vertical planes called edge or boundary define confinement for rectangular or square diaphragm. The gap between two parallel planes is called thickness (h), whereas distance between vertical planes is length (a) and width (b) of a thin plate.

The following fundamental assumptions are taken to solve mathematical equations analytically for bending of thin plates based on small deflection theory [111].

- i. The material of the plate is assumed to be elastic, homogeneous, and isotropic.
- ii. The plate is assumed to be flat initially.
- iii. Deflection of mid-plane is small as compared to thickness of the plate. The slope of deflected surface is assumed to be very small, and its square is negligible. The middle surface is supposed to be unstained after bending.
- iv. The straight line which is initially normal to the middle plane before bending, remain straight and normal to the central/middle surface during the deformation, and the length of such elements is not altered. It means that the vertical shear strains γ_{xz} and γ_{yz} are negligible and the normal strain ϵ_z may also be omitted.
- v. The stress normal to the middle plane (σ_z) is small compared with the other stress components and may be neglected in the stress-strain relations.

These assumptions are known as Kirchhoff's hypotheses [111]. Thin plate bending theory based on these assumptions is known as classical or Kirchhoff's plate theory.

A.2.1 State of stress at a point

The cartesian coordinate system is used to analyse the theory of thin plate. The origin is assumed in the middle/neutral surface of a diaphragm, x-axis and y-axis are in the middle/neutral surface and the z-axis is perpendicular to the middle/neutral surface. A distributed pressure is applied on the top of diaphragm for a small deflection. Hence, the induced stress components into x-direction are (stress), (shear stress) and (shear stress). Similarly, the induced stress components in other directions are presented in Figure A.1. The first subscript indicates the direction of an outer normal to the face on which the stress component acts; the second subscript relates to the direction of stress itself. These are represented together in the form of the stress tensor in equation (A.4) [111].

$$T_s = \begin{pmatrix} \sigma_{xx} & \tau_{xy} & \tau_{xz} \\ \tau_{yx} & \sigma_{yy} & \tau_{yz} \\ \tau_{zx} & \tau_{zy} & \sigma_{zz} \end{pmatrix} \quad (\text{A.4})$$

By symmetry, the shear stresses can be expressed as, $\tau_{xy} = \tau_{yx}$, $\tau_{yz} = \tau_{zy}$ and $\tau_{xz} = \tau_{zx}$.

Therefore, six stress components are independent stress tensor equation (A.4). The stress tensor, T_s , for thin plate is presented after neglecting z-axis direction stress components i.e

$\sigma_z = \tau_{yz} = \tau_{zy} = 0$. Therefore, equation 2.4 is rewritten as in equation (A.5),

$$T_s = \begin{pmatrix} \sigma_x & \tau_{xy} \\ \tau_{yx} & \sigma_y \end{pmatrix}, \text{ where } \tau_{xy} = \tau_{yx} \quad (\text{A.5})$$

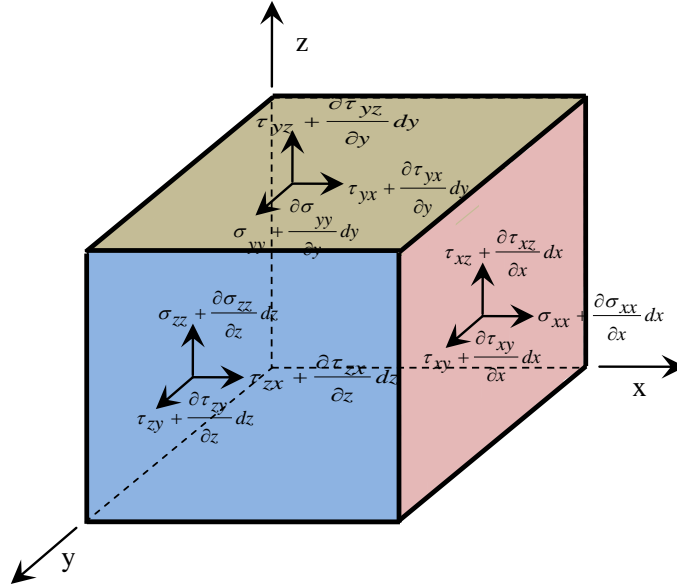


Figure A.1: Pictorial representation of stress components at a point of interest.

A.2.2 State of strain at a point

In order to compute the stress and strain relationship, the strain due to applied pressure for 3D structures is analysed. Strain is defined as the fractional change in the length divided by the actual length. Mathematically, for three-dimensional structure strain is defined along the x, y and z-axis respectively as in equation (A.6),

$$\varepsilon_x = \frac{\partial dx}{dx}, \varepsilon_y = \frac{\partial dy}{dy} \text{ and } \varepsilon_z = \frac{\partial dz}{dz} \quad (\text{A.6})$$

These parameters are known as linear or normal strain. The increment ∂dx can be expressed by the second term in the Taylor series, e.g. $\partial dx = \frac{\partial u}{\partial x} dx$, etc. Hence, the normal strain is written along the x, y and z axis respectively in equation (A.7) as,

$$\varepsilon_x = \frac{\partial u}{\partial x}, \varepsilon_y = \frac{\partial v}{\partial y} \text{ and } \varepsilon_z = \frac{\partial w}{\partial z} \quad (\text{A.7})$$

Where, $u = x' - x$, $v = y' - y$ and $w = z' - z$.

For thin plate u , v and w are functions of x, y . A pictorial representation of normal strain due to elongation/contraction is given in Figure A.2 (a), (b) and (c) for ε_x , ε_y and ε_z respectively. Other three deformations are known as shear deformation/shear strain (Figure A.2 (d), (e) and (f)) and are denoted by γ_{xy} , γ_{yz} and γ_{zx} respectively.

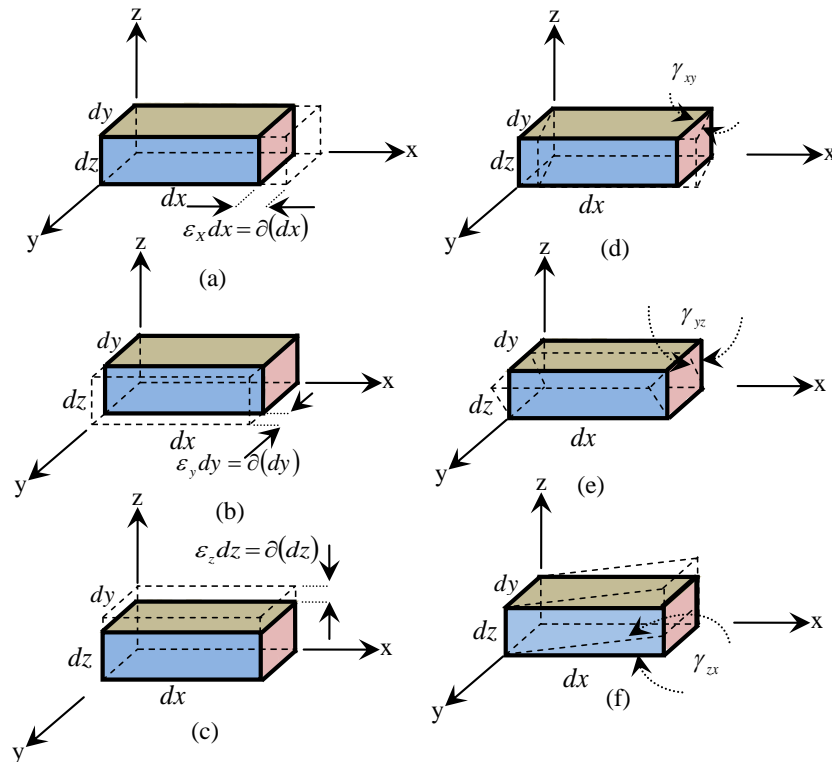


Figure A.2: Strain elongation and shear [111].

As shown in Figure A.3, if we consider a body denoted as A B C D, after deformation, the shape of the body changes to A' B' C' D'. The angle BAD deforms as B' A' D', therefore, shear strain can be calculated as in equation (A.8),

$$\gamma_{xy} = \gamma' + \gamma'' \quad (\text{A.8})$$

Or this can be determined in terms of the in-plane displacements, u and v , as,

$$\gamma_{xy} = \frac{\frac{\partial v}{\partial x} dx}{dx + \frac{\partial u}{\partial x} dx} + \frac{\frac{\partial u}{\partial y} dy}{dy + \frac{\partial v}{\partial y} dy} = \frac{\frac{\partial v}{\partial x}}{1 + \frac{\partial u}{\partial x}} + \frac{\frac{\partial u}{\partial y}}{1 + \frac{\partial v}{\partial y}} = \frac{\partial v}{\partial x} + \frac{\partial u}{\partial y} \quad (\text{A.9})$$

Similarly, other shear strains i.e. γ_{xz} and γ_{yz} . can be calculated as in equation (A.10),

$$\gamma_{xz} = \frac{\partial u}{\partial z} + \frac{\partial w}{\partial x} \text{ and } \gamma_{yz} = \frac{\partial v}{\partial z} + \frac{\partial w}{\partial y} \quad (\text{A.10})$$

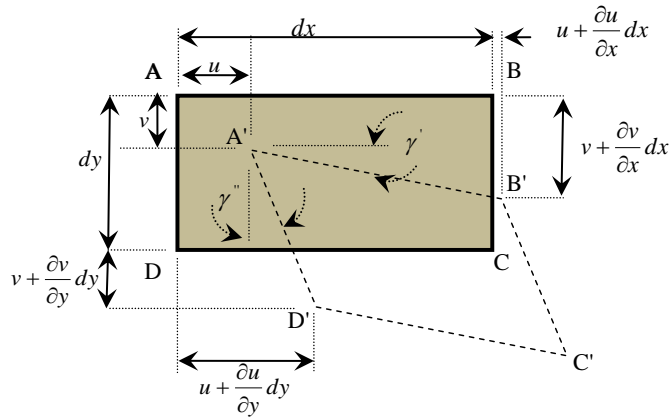


Figure A.3: Shear strain representation [111].

Also similarly, strain tensor is defined at single point of state as in equation (A.11),

$$T_D = \begin{pmatrix} \epsilon_x & \frac{1}{2}\gamma_{xy} & \frac{1}{2}\gamma_{xz} \\ \frac{1}{2}\gamma_{yx} & \epsilon_y & \frac{1}{2}\gamma_{yz} \\ \frac{1}{2}\gamma_{zx} & \frac{1}{2}\gamma_{zy} & \epsilon_z \end{pmatrix} \quad (\text{A.11})$$

Strain tensor is symmetric, therefore shear strain components are equivalent i.e. $\gamma_{xy} =$

γ_{yx} , $\gamma_{yz} = \gamma_{zy}$ and $\gamma_{xz} = \gamma_{zx}$. Also, z-axis strain is neglected based on thin plate theory.

A.2.3 Hooke's law

The relation between stress and strain is defined using Hooke's law, also known as a Constitutive equation. The relationship between the stress and strain for a three-dimensional isotropic body for linear strain is given as in equation (A.12),

$$\varepsilon_x = \frac{1}{E} [\sigma_x - \nu(\sigma_y + \sigma_z)], \quad \varepsilon_y = \frac{1}{E} [\sigma_y - \nu(\sigma_x + \sigma_z)], \quad \varepsilon_z = \frac{1}{E} [\sigma_z - \nu(\sigma_x + \sigma_y)] \quad (\text{A.12})$$

and for shear strain it is expressed as in equation (A.13),

$$\gamma_{xy} = \frac{1}{G} \tau_{xy}, \quad \gamma_{xz} = \frac{1}{G} \tau_{xz}, \quad \gamma_{yz} = \frac{1}{G} \tau_{yz} \quad (\text{A.13})$$

Moreover, shear modulus (G) is related to Young's modulus (E) as in equation (A.14),

$$G = \frac{E}{2(1+\nu)} \quad (\text{A.14})$$

Where, E is modulus of elasticity, ν is Poisson's ratio, and G is shear modulus.

A.2.4 Equilibrium equations

The stress components introduced previously must satisfy the following differential equations of equilibrium given as in equations (A.15) (A.16) and (A.17),

$$\frac{\partial \sigma_x}{\partial x} + \frac{\partial \tau_{xy}}{\partial y} + \frac{\partial \tau_{xz}}{\partial z} + F_x = 0 \quad (\text{A.15})$$

$$\frac{\partial \sigma_y}{\partial y} + \frac{\partial \tau_{yx}}{\partial x} + \frac{\partial \tau_{yz}}{\partial z} + F_y = 0 \quad (\text{A.16})$$

$$\frac{\partial \sigma_z}{\partial z} + \frac{\partial \tau_{zx}}{\partial x} + \frac{\partial \tau_{zy}}{\partial y} + F_z = 0 \quad (\text{A.17})$$

Where F_x , F_y and F_z are the body forces i.e. force per volume due to gravitational, magnetic or any applied force.

A.2.5 Compatibility equations

The solution of the three equilibrium equations is complex because these equations contain six unknown quantities. The compatibility equations are obtained to express the continuity of a body as the additional equations. The six strain components are related with three displacement components for the isotropic 3D structure. The compatibility equations are obtained by 2nd order successive differentiation of equation (A.18), (A.19), (A.20), (A.21), (A.22) and (A.23) respectively,

$$\frac{\partial^2 \varepsilon_x}{\partial y^2} + \frac{\partial^2 \varepsilon_y}{\partial x^2} = \frac{\partial^2 \gamma_{xy}}{\partial x \partial y} \quad (\text{A.18})$$

$$\frac{\partial^2 \varepsilon_y}{\partial z^2} + \frac{\partial^2 \varepsilon_z}{\partial y^2} = \frac{\partial^2 \gamma_{yz}}{\partial y \partial z} \quad (\text{A.19})$$

$$\frac{\partial^2 \varepsilon_z}{\partial x^2} + \frac{\partial^2 \varepsilon_x}{\partial z^2} = \frac{\partial^2 \gamma_{xz}}{\partial x \partial z} \quad (\text{A.20})$$

$$\frac{\partial}{\partial z} \left[\frac{\partial \gamma_{yz}}{\partial x} + \frac{\partial \gamma_{xz}}{\partial y} - \frac{\partial \gamma_{xy}}{\partial z} \right] = 2 \frac{\partial^2 \varepsilon_z}{\partial x \partial y} \quad (\text{A.21})$$

$$\frac{\partial}{\partial x} \left[\frac{\partial \gamma_{xz}}{\partial y} + \frac{\partial \gamma_{xy}}{\partial z} - \frac{\partial \gamma_{yz}}{\partial x} \right] = 2 \frac{\partial^2 \varepsilon_x}{\partial y \partial z} \quad (\text{A.22})$$

$$\frac{\partial}{\partial y} \left[\frac{\partial \gamma_{xz}}{\partial z} + \frac{\partial \gamma_{yz}}{\partial x} - \frac{\partial \gamma_{xz}}{\partial y} \right] = 2 \frac{\partial^2 \varepsilon_y}{\partial x \partial z} \quad (\text{A.23})$$

For a two-dimensional state of stress, the stress components along the z-axis are assumed to be zero i.e. $\sigma_z = \tau_{xz} = \tau_{yz} = 0$. Therefore, the modified equilibrium equations are shown in equations (A.24) and (A.25) from equations (A.15), (A.16) and (A.17),

$$\frac{\partial \sigma_x}{\partial x} + \frac{\partial \tau_{xy}}{\partial y} + F_x = 0 \quad (\text{A.24})$$

$$\frac{\partial \sigma_y}{\partial y} + \frac{\partial \tau_{yx}}{\partial x} + F_y = 0 \quad (\text{A.25})$$

In addition, the compatibility equations are simplified for two dimensions from (A.18), (A.19) and (A.20) and shown in equation (A.26),

$$\frac{\partial^2 \varepsilon_x}{\partial y^2} + \frac{\partial^2 \varepsilon_y}{\partial x^2} = \frac{\partial^2 \gamma_{xy}}{\partial x \partial y}, \quad \text{where, } (\gamma_{xz} = \gamma_{yz} = \varepsilon_z = 0) \quad (\text{A.26})$$

It can be rewritten as in equation (A.27),

$$\left(\frac{\partial^2}{\partial y^2} + \frac{\partial^2}{\partial x^2} \right) (\sigma_x + \sigma_y) = 0 \quad (\text{A.27})$$

This equation is called Levy's equation. Using Airy's stress function $\phi(x, y)$ in eq (A.28),

$$\sigma_x = \frac{\partial^2 \phi}{\partial y^2}, \quad \sigma_y = \frac{\partial^2 \phi}{\partial x^2}, \quad \tau_{xy} = \frac{\partial^2 \phi}{\partial x \partial y} \quad (\text{A.28})$$

the above equation can be written as,

$$\nabla^2 \nabla^2 \phi = 0 \quad (\text{A.29})$$

Where, ∇ is the two-dimensional Laplace operator as, $\nabla^2 = \frac{\partial^2}{\partial x^2} + \frac{\partial^2}{\partial y^2}$.

The small deflection theory is based on the assumption as explained below.

A.2.5.1 Consideration 1

Normal strain, vertical to the neutral surface of the diaphragm is to be neglected i.e. $\varepsilon_z = 0$. It signifies that differentiation of w with respect to z is zero i.e. $\varepsilon_z = \frac{\partial w}{\partial z} = 0$, Therefore, w is a function of x and y $w = w(x, y)$.

A.2.5.2 Consideration 2

The stress components τ_{zx} , τ_{zy} and σ_z are far smaller than the other stress components, thus the strain caused by these can be neglected, $\gamma_{zx} = 0$, $\gamma_{zy} = 0$ and $\varepsilon_x = 0$. According to the geometric equations,

$$\gamma_{zx} = \frac{\partial u}{\partial z} + \frac{\partial w}{\partial x} \text{ and } \gamma_{zy} = \frac{\partial v}{\partial z} + \frac{\partial w}{\partial y} \quad (\text{A.30})$$

$$\frac{\partial u}{\partial z} = -\frac{\partial w}{\partial x} \text{ and } \frac{\partial v}{\partial z} = -\frac{\partial w}{\partial y} \quad (\text{A.31})$$

Neglecting the strains caused by σ_z strain can be written as,

$$\varepsilon_x = \frac{1}{E} [\sigma_x - \vartheta \sigma_y] \quad (\text{A.32})$$

$$\varepsilon_y = \frac{1}{E} [\sigma_y - \vartheta \sigma_x] \quad (\text{A.33})$$

$$\gamma_{xy} = \frac{1}{G} \tau_{xy} \text{ Where; } G = \frac{E}{2(1+\vartheta)} \quad (\text{A.34})$$

Where E , ϑ and G are the modulus of elasticity, Poisson's ratio, and the shear modulus, respectively and the relationship between E and G is presented in equation 2.34.

The above equations can be rewritten as,

$$\sigma_x = \frac{E}{(1+\vartheta)} [\varepsilon_x + \vartheta \varepsilon_y] \quad (\text{A.35})$$

$$\sigma_y = \frac{E}{(1+\vartheta)} [\varepsilon_y + \vartheta \varepsilon_x] \quad (\text{A.36})$$

$$\tau_{xy} = \frac{E}{2(1+\vartheta)} \gamma_{xy} \quad (\text{A.37})$$

A.2.5.3 Consideration 3

The zero displacement is assumed at the point on the neutral surface of diaphragm i.e.

$u_{z=0} = 0, v_{z=0} = 0$ because of $\varepsilon_x = \frac{\partial u}{\partial x}$, $\varepsilon_y = \frac{\partial v}{\partial y}$ and $\gamma_{xy} = \frac{\partial v}{\partial x} + \frac{\partial u}{\partial y}$. Therefore, strain at z-axis direction becomes zero i.e. $\varepsilon_x|_{z=0} = 0$, $\varepsilon_y|_{z=0} = 0$ and $\gamma_{xy}|_{z=0} = 0$. The u^z and v^z are written by integrating the equations,

$$u^z = -z \frac{\partial w}{\partial x} + u(x, y), v^z = -z \frac{\partial w}{\partial y} + v(x, y) \quad (\text{A.38})$$

Where w^z, u^z and v^z are displacement points at a distance z from the middle surface.

$u(x, y) = 0$ and $v(x, y) = 0$ because they are constant with respect to z . Hence, strain can be calculated as in equations (2.39)-(2.41).

$$\varepsilon_x = \frac{\partial u}{\partial x} = -z \frac{\partial^2 w}{\partial x^2} \quad (\text{A.39})$$

$$\varepsilon_y = \frac{\partial v}{\partial y} = -z \frac{\partial^2 w}{\partial y^2} \quad (\text{A.40})$$

$$\gamma_{xy} = \frac{\partial v}{\partial x} + \frac{\partial u}{\partial y} = -2z \frac{\partial^2 w}{\partial x \partial y} \quad (\text{A.41})$$

Substituting strain equations (2.39)-(2.41) in stress equations (2.35)-(2.37),

$$\sigma_x = \frac{E}{(1+\vartheta)} [\varepsilon_x + \vartheta \varepsilon_y] = -\frac{Ez}{(1+\vartheta)} \left[\frac{\partial^2 w}{\partial x^2} + \vartheta \frac{\partial^2 w}{\partial y^2} \right] \quad (\text{A.42})$$

$$\sigma_y = \frac{E}{(1+\vartheta)} [\varepsilon_y + \vartheta \varepsilon_x] = -\frac{Ez}{(1+\vartheta)} \left[\frac{\partial^2 w}{\partial y^2} + \vartheta \frac{\partial^2 w}{\partial x^2} \right] \quad (\text{A.43})$$

$$\tau_{xy} = \frac{E}{2(1+\vartheta)} \gamma_{xy} = \frac{Ez}{(1+\vartheta)} \frac{\partial^2 w}{\partial x \partial y} \quad (\text{A.44})$$

A.2.6 Bending and shear moment of plate

Uniform load is applied on the top of the plate/diaphragm in the z -direction (Figure A.4 (a) and (b)). The stress components are integrated along the thickness of plate/diaphragm, in order to calculate the bending moment of plate. The normal stress components (i.e. σ_x and σ_y) are integrated along the thickness of the plate to obtain the bending moment (i.e. M_x , and M_y) and shear stress (τ_{xy}) is integrated along the thickness to obtain the bending moment (M_{xy}). Similarly, other shear components i.e. τ_{xz} and τ_{yz} are integrated along the thickness of plate to obtain transversal shear, Q_x and Q_y respectively.

$$\begin{Bmatrix} M_x \\ M_y \\ M_{xy} \end{Bmatrix} = \int_{-h/2}^{h/2} \begin{Bmatrix} \sigma_x \\ \sigma_y \\ \tau_{xy} \end{Bmatrix} z dz \quad (\text{A.45})$$

$$\text{and, } \begin{Bmatrix} Q_x \\ Q_y \end{Bmatrix} = \int_{-h/2}^{h/2} \begin{Bmatrix} \tau_{xz} \\ \tau_{yz} \end{Bmatrix} dz \quad (\text{A.46})$$

Substituting values and integrating over the plate's thickness as,

$$M_x = -D \left(\frac{\partial^2 w}{\partial x^2} + \vartheta \frac{\partial^2 w}{\partial y^2} \right) \quad (\text{A.47})$$

$$M_y = -D \left(\frac{\partial^2 w}{\partial y^2} + \vartheta \frac{\partial^2 w}{\partial x^2} \right) \quad (\text{A.48})$$

$$M_{xy} = -D(1 - \vartheta) \frac{\partial^2 w}{\partial x \partial y} \quad (\text{A.49})$$

Where, $D = \frac{Eh^2}{12(1-\vartheta^2)}$ is flexural rigidity of plate. It is same role as flexural rigidity EI .

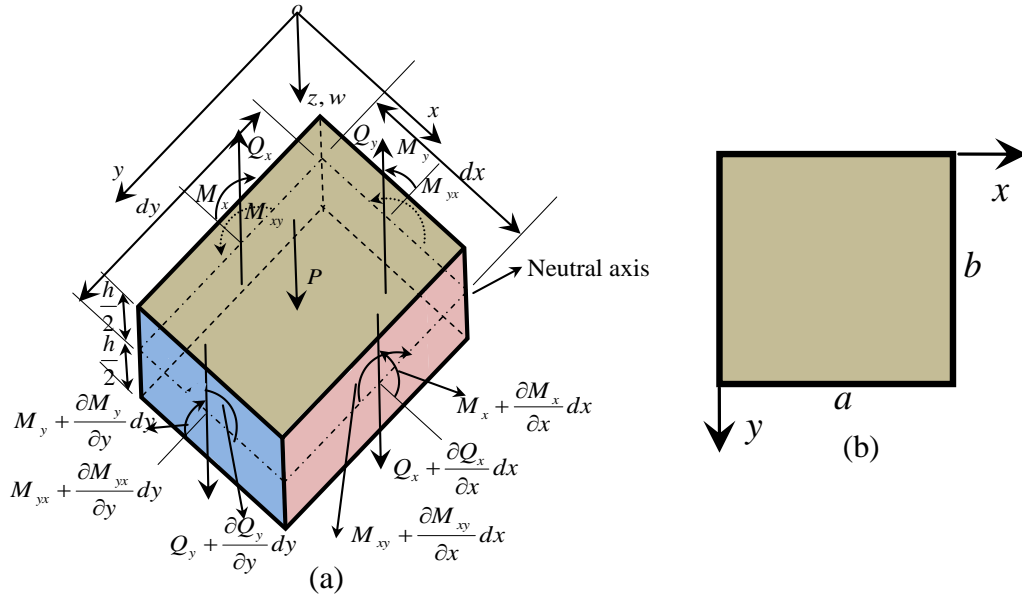


Figure A.4: (a) Mechanical analysis of micro unit of diaphragm [111] (b) Simplified top view of a thin plate.

According to the equilibrium conditions of thin plate are,

$$\sum M_x = 0, \sum M_y = 0, \sum F_z = 0 \quad (\text{A.50})$$

The moment summation about y-axis result in $\sum M_y = 0$. Hence, it is written as,

$$\frac{\partial M_{yx}}{\partial y} dx dy + \frac{\partial M_x}{\partial x} dx dy - Q_x dx dy = 0 \quad (\text{A.51})$$

Neglecting higher order terms, it can be written as,

$$Q_x = \frac{\partial M_{yx}}{\partial y} + \frac{\partial M_x}{\partial x} \quad (\text{A.52})$$

The moment summation about x-axis leads to $\sum M_x = 0$. Hence,

$$Q_y = \frac{\partial M_{xy}}{\partial x} + \frac{\partial M_y}{\partial y} \quad (\text{A.53})$$

The force summation in z-axis gives, $\sum F_z = 0$. Hence, it can be written as,

$$\frac{\partial Q_x}{\partial x} dx dy + \frac{\partial Q_y}{\partial y} dx dy + P dx dy = 0 \text{ or } -P = \frac{\partial Q_x}{\partial x} + \frac{\partial Q_y}{\partial y} \quad (\text{A.54})$$

From equation (2.52), (2.53) and (2.54), it is written as,

$$\frac{\partial^2 M_x}{\partial x^2} + 2 \frac{\partial^2 M_{xy}}{\partial x \partial y} + \frac{\partial^2 M_y}{\partial y^2} = -P(x, y) \quad (\text{A.55})$$

Substituting equation (2.47)-(2.49) in (2.55),

$$\frac{\partial^4 w}{\partial x^4} + 2 \frac{\partial^4 w}{\partial x^2 \partial y^2} + \frac{\partial^4 w}{\partial y^4} = -\frac{P}{D} \quad (\text{A.56})$$

The equation (2.56) is the governing equation for the thin plate.

A.2.7 Solution of the governing equation

As a general case, let us assume that applied pressure P is [69],

$$P = P_0 \sin \frac{\pi x}{a} \sin \frac{\pi y}{b} \quad (\text{A.57})$$

Assumed pressure input (equation (2.57)) is substituted in equation (2.56) to obtain,

$$\frac{\partial^4 w}{\partial x^4} + 2 \frac{\partial^4 w}{\partial x^2 \partial y^2} + \frac{\partial^4 w}{\partial y^4} = -\frac{P_0}{D} \sin \frac{\pi x}{a} \sin \frac{\pi y}{b} \quad (\text{A.58})$$

A.2.7.1 Boundary conditions

The boundary conditions are taken such that deflection of thin plate/diaphragm at edge is zero i.e. $w = 0$ and $M_y = 0$; for $x = 0$ & $x = a$ and $w = 0$ and $M_x = 0$; for $y =$

0 & $y = b$. The boundary conditions become;

- $w = 0$ at $x = 0$ & $x = a$
- $\frac{\partial^2 w}{\partial x^2} = 0$
- $w = 0$ at $y = 0$ & $y = b$
- $\frac{\partial^2 w}{\partial y^2} = 0$

Let us suppose that deflection w is given as;

$$w = C \sin \frac{\pi x}{a} \sin \frac{\pi y}{b} \quad (\text{A.59})$$

Where C is constant and must be selected such that it satisfies the following equation,

$$\frac{\partial^4 w}{\partial x^4} + 2 \frac{\partial^4 w}{\partial x^2 \partial y^2} + \frac{\partial^4 w}{\partial y^4} = -\frac{P_0}{D} \sin \frac{\pi x}{a} \sin \frac{\pi y}{b} \quad (\text{A.60})$$

By substituting the value of w in the above equation,

$$\frac{\partial^4}{\partial x^4} \left[C \sin \frac{\pi x}{a} \sin \frac{\pi y}{b} \right] = C \sin \frac{\pi y}{b} \frac{\partial^4}{\partial x^4} \left[\sin \frac{\pi x}{a} \right] = \frac{C \pi^4}{a^4} \sin \frac{\pi y}{b} \sin \frac{\pi x}{a} \quad (\text{A.61})$$

$$\text{Similarly, } \frac{\partial^4}{\partial y^4} \left[C \sin \frac{\pi x}{a} \sin \frac{\pi y}{b} \right] = C \sin \frac{\pi x}{a} \frac{\partial^4}{\partial y^4} \left[\sin \frac{\pi y}{b} \right] = \frac{C \pi^4}{b^4} \sin \frac{\pi x}{a} \sin \frac{\pi y}{b} \quad (\text{A.62})$$

$$\text{and, } 2 \frac{\partial^4}{\partial x^2 \partial y^2} \left[C \sin \frac{\pi x}{a} \sin \frac{\pi y}{b} \right] = \frac{2C \pi^4}{a^2 b^2} \sin \frac{\pi x}{a} \sin \frac{\pi y}{b} \quad (\text{A.63})$$

By adding all three terms and calculating the value of C ,

$$C = -\frac{P_0}{D \pi^4 \left(\frac{1}{a^2} + \frac{1}{b^2} \right)^2} \quad (\text{A.64})$$

$$\text{Therefore, } w = -\frac{P_0}{D \pi^4 \left(\frac{1}{a^2} + \frac{1}{b^2} \right)^2} \sin \frac{\pi x}{a} \sin \frac{\pi y}{b} \quad (\text{A.65})$$

Putting w in expression M_x , M_y and M_{xy} ,

$$M_x = -D \left(\frac{\partial^2 w}{\partial x^2} + \vartheta \frac{\partial^2 w}{\partial y^2} \right) = \nabla^2 \left[\frac{D P_0}{D \pi^4 \left(\frac{1}{a^2} + \frac{1}{b^2} \right)^2} \sin \frac{\pi x}{a} \sin \frac{\pi y}{b} \right] \text{ or} \\ M_x = \frac{P_0}{\pi^2 \left(\frac{1}{a^2} + \frac{1}{b^2} \right)^2} \left[\frac{1}{a^2} + \frac{\vartheta}{b^2} \right] \sin \frac{\pi x}{a} \sin \frac{\pi y}{b} \quad (\text{A.66})$$

$$\text{Similarly, } M_y = \frac{P_0}{\pi^2 \left(\frac{1}{a^2} + \frac{1}{b^2} \right)^2} \left[\frac{\vartheta}{a^2} + \frac{1}{b^2} \right] \sin \frac{\pi x}{a} \sin \frac{\pi y}{b} \quad (\text{A.67})$$

$$\text{and } M_{xy} = \frac{P_0(1-\vartheta)}{\pi^2 \left(\frac{1}{a^2} + \frac{1}{b^2} \right)^2 ab} \cos \frac{\pi x}{a} \cos \frac{\pi y}{b} \quad (\text{A.68})$$

Since, the maximum deflection and maximum bending are at the centre of the plate,

$$\text{Putting } x = a/2 \text{ \& } y = b/2, w_{max} = -\frac{P_0}{D \pi^4 \left(\frac{1}{a^2} + \frac{1}{b^2} \right)^2} \sin \frac{\pi a}{2a} \sin \frac{\pi b}{2b}$$

$$w_{max} = -\frac{P_0}{D \pi^4 \left(\frac{1}{a^2} + \frac{1}{b^2} \right)^2}; \text{ Where } D = \frac{E h^2}{12(1-\vartheta^2)}$$

$$w_{max} = -\frac{12(1-\vartheta^2)P_0}{E h^2 \pi^4 \left(\frac{1}{a^2} + \frac{1}{b^2} \right)^2} \quad (\text{A.69})$$

$$M_x = \frac{P_0}{\pi^2 \left(\frac{1}{a^2} + \frac{1}{b^2} \right)^2} \left[\frac{1}{a^2} + \frac{\vartheta}{b^2} \right] \sin \frac{\pi a}{2a} \sin \frac{\pi b}{2b} \quad (\text{A.70})$$

$$(M_x)_{max} = \frac{P_0}{\pi^2 \left(\frac{1}{a^2} + \frac{1}{b^2}\right)^2} \left[\frac{1}{a^2} + \frac{\vartheta}{b^2} \right] \quad (\text{A.71})$$

$$\text{Similarly, } (M_y)_{max} = \frac{P_0}{\pi^2 \left(\frac{1}{a^2} + \frac{1}{b^2}\right)^2} \left[\frac{\vartheta}{a^2} + \frac{1}{b^2} \right] \quad (\text{A.72})$$

$$\text{and, } (M_{xy})_{max} = 0 \quad (\text{A.73})$$

The condition for square plate is $a = b$,

$$w_{max} = -\frac{12(1-\vartheta^2)P_0a^4}{4Eh^3\pi^4}, \text{ Where, } \alpha = -\frac{3(1-\vartheta^2)}{\pi^4} \quad (\text{A.74})$$

$$(M_x)_{max} = (M_y)_{max} = \frac{P_0}{\pi^2 \left(\frac{1}{a^2} + \frac{1}{a^2}\right)^2} \left[\frac{\vartheta}{a^2} + \frac{1}{a^2} \right] = \frac{(1+\vartheta)P_0a^2}{4\pi^2} \quad (\text{A.75})$$

$$(\sigma_x)_{max} = (\sigma_y)_{max} = \frac{6(M_y)_{max}}{h^2} = \frac{6(1+\vartheta)P_0a^2}{4\pi^2h^2} \quad (\text{A.76})$$

$$(\sigma_x)_{max} = (\sigma_y)_{max} = \beta \frac{P_0a^2}{h^2}, \text{ Where } \beta = \frac{6(1+\vartheta)}{4\pi^2}$$

A.2.7.2 Simplified equation for rectangular plates with all edges fixed

A closed form solution for deflection of plate is available in Timoshenko [69], [112].

$$(\sigma_x)_{max} = (\sigma_y)_{max} = \beta \frac{P_0a^2}{h^2} \quad (\text{A.77})$$

and the maximum deflection of the plate occurs at the centre,

$$w_{max} = \alpha \frac{P_0b^2}{Eh^3} \quad (\text{A.78})$$

A.2.7.3 Square plates of silicon with edges fixed

The square diaphragm geometry is common in MEMS pressure sensors due to generation of maximum stress and maximum output compared to other geometry of diaphragms with the same plate area. Maximum stress occurs at the middle of etched edges [112];

$$\sigma_{max} = \frac{0.308Pa^2}{h^2} \quad (\text{A.79})$$

and the maximum deflection of the plate occurs at the centre of the plate,

$$w_{max} = -\frac{0.0138Pa^4}{Eh^3} \quad (\text{A.80})$$

The coefficients for maximum stress and deflection for plates with varying aspect ratios are given in Table A.1.

Table A.1: Coefficients for maximum stress and deflection in rectangular plates [33].

a/b	1	1.2	1.4	1.6	1.8	2.0	Infinity
α	0.0138	0.0188	0.0226	0.0251	0.0267	0.0277	0.0284
β	0.3078	0.3834	0.4356	0.4680	0.4872	0.4974	0.5000

Appendix B. PIEZORESISTIVE EFFECT: AN INTRODUCTION

A piezoresistive pressure sensor operates on the principle of converting the induced stress into a change in resistance and hence, in analogous electrical voltage. Therefore, the sensitivity of piezoresistive pressure sensor is governed by the location of piezoresistors at the maximum stress concentration regions on the diaphragm. The piezoresistors are implanted / diffused in higher stress concentration regions to maximise the sensitivity. In current section, first focus is to analyse various parameters which are responsible for the relative change in resistance ($\Delta R/R$) under induced strain/stress. The change in the resistance per unit strain is defined as gauge factor and it is written as in equation (B.1),

$$G = \frac{\Delta R}{R\varepsilon} \quad (\text{B.1})$$

Where, $\Delta R/R$ is the relative change in the resistance and ε is subjected strain on resistors.

The relative change in the resistance is not only the function of change in the resistivity but also a function of the geometrical dimension of resistors. The change in the resistance due to geometrical dimensions is insignificant in the case of semiconductor based resistors compared to the change in the resistance due to the change of resistivity. In order to understand the piezoresistivity in details for semiconductors, discussion on the crystallographic orientation, dopant concentration, strain and stress tensor and further effect of temperature on piezoresistivity is presented in the subsequent sections.

B.1 ELECTRICAL RESISTANCE OF A HOMOGENEOUS RESISTOR WITH A RECTANGULAR SHAPE

A homogeneous resistor is considered with a rectangular shape having thickness t , width w , and length l (Figure B.1 (a) and (b)). The electrical resistance of the homogeneous rectangular bar is given as in equation (B.2),

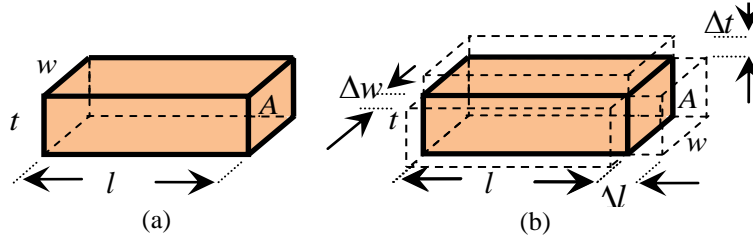


Figure B.1: (a) Electrical resistance of a homogeneous bar with dimensions of length (l) \times width (w) \times thickness (t) and resistivity (ρ), b) When subjected to loading, all three can potentially change, leading to a change in the measured electrical resistance [94].

$$R = \frac{\rho l}{A} = \frac{\rho l}{wt} \quad (\text{B.2})$$

by taking natural log and partial derivatives to equation (B.2),

$$\frac{\Delta R}{R} = \frac{\Delta l}{l} - \frac{\Delta w}{w} - \frac{\Delta t}{t} + \frac{\Delta \rho}{\rho} \quad (\text{B.3})$$

Where, Δl , Δw , Δt , and $\Delta \rho$ are the change in parameters i.e. the length, width and thickness respectively due to the strain/stress. If the resistors experience the tensile stress along their length, thickness and width of the resistors will decrease whereas length will increase. The change in length (Δl) is correlated to the change in width (Δw) and the change in thickness (Δt) of the piezoresistors using the Poisson's ratio, ν as explained in equation (B.4) and gauge factor can be rewritten as in equation (B.5),

$$\frac{\Delta w}{w} = \frac{\Delta t}{t} = -\nu \frac{\Delta l}{l} \quad (\text{B.4})$$

$$GF = \frac{\Delta R}{R \varepsilon} = 1 + 2\nu + \frac{\Delta \rho}{\rho \varepsilon} \quad (\text{B.5})$$

Where G is gauge factor, $\varepsilon = \frac{\Delta l}{l}$ is strain.

The first two terms in equation (B.5) are due to geometrical changes which are more significant in metal strain gauges, while the last term is due to a change in resistivity which is dominant in the case of the semiconductors. The range of the gauge factor for various materials is listed in Table B.1.

Under applied strain/stress, the gauge factor of metals is dependent on the resistance change due to geometrical variation, whereas resistance change in the semiconductors is

mainly dependent on the variation in the resistivity. However, change in the resistivity ($\Delta\rho / \rho$) is 50 to 100 times larger than the geometric term in the case of semiconductors (e.g. Si and Ge) due to piezoresistive effect. Hence, a mathematical calculation for piezoresistive coefficients and a gauge factor of silicon is discussed in next section as a first step towards design of piezoresistive sensors.

Table B.1: Gauge factors of different types of strain gauges [113].

Type of Strain Gauge	Gauge Factor (GF)
Metal foil	1 to 5
Thin film metal	$\cong 2$
Diffused Si and Ge	80 to 200
Polycrystalline silicon	$\cong 30$
Polycrystalline SiC	3 to 5
Single crystal SiC	10 to 30
Carbon Nanotube	200 to 1000

B.2 THEORY OF PIEZORESISTIVITY IN SILICON

The piezoresistivity in silicon is explained by the change in the energy band structure under the applied pressure/stress. It is a resultant change in the effective mass and consequently the change in mobility of electrons and holes. Hence, the resistivity is altered when semiconductor resistors are subjected to a longitudinal or compressive stress. The scattering effect due to change in the mean path is liable for the change in the mobility of current carriers [113]. The change in the resistance is observed in p-type semiconductor resistor when it is subjected to a longitudinal pressure/stress. The hole transport mechanism in a p-type semiconductor is by the hopping movement of electrons from an occupied state to a nearby vacant state of the lattice atom. The distance between the lattice atoms increases by a small extent when the lattice is subjected to an elongation of the longitudinal stress [113]. Hence, this results in more difficulty in the hopping of the electron to the nearby

lattice. Therefore, the mobility of the hole is reduced and this appears as an increase in its effective mass. It leads to an increase in the resistivity of the p-type resistors. The resistivity of p-type semiconductors decreases under compressive stress loading. However, an opposite effect is seen in the n-type semiconductors [113]. A simplified resistivity relation of p and n-type semiconductor is given by equations (B.6) and (B.7).

$$\rho_p = \frac{1}{q\mu_p p} \quad (\text{B.6})$$

$$\rho_n = \frac{1}{q\mu_n n} \quad (\text{B.7})$$

Where, q is the electron charge, n and p are concentrations of electron and hole respectively, μ_n and μ_p are mobilities of the electron and hole respectively. The crystal structure of silicon needs to be studied in order to understand the theory of piezoresistivity. In next subsection, the crystal structure of silicon is explained in details.

B.3 CRYSTAL STRUCTURE OF SILICON

Crystals are ordered arrangement of atoms with a periodic fashion in one of 14 lattice types. The smallest group of atoms in a material, which is known as a unit cell of structure repeats periodically. The Miller indices are used to specify the crystal orientations by means of vectors and planes in a crystal lattice. The direction index $[hkl]$ denotes a vector normal to a plane described by (hkl) . Angle bracketed indices, i.e. $\langle hkl \rangle$ represent a group of all directions equivalent to $[hkl]$ by symmetry. The family of planes, which are normal to $[hkl]$ are denoted with curly brackets as $\{hkl\}$. The crystalline silicon is formed by a covalent bonded diamond-cubic structure with a lattice constant $a_c = 5.43 \text{ \AA}$. The diamond-cubic structure is two interpenetrating face centred cubic (FCC) lattice with basis atom offset by $\frac{1}{4}a_c$ in three orthogonal directions. The crystal planes, diamond cubic lattice of silicon and schematic of wafer are shown in Figure B.2 (a)-(e).

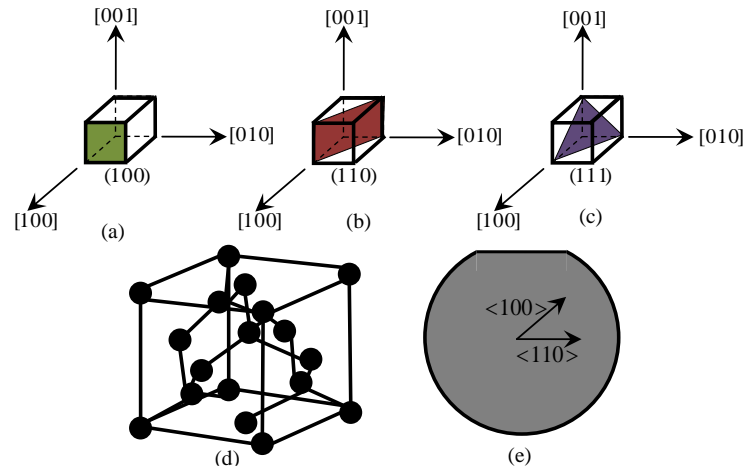


Figure B.2: Crystal planes of silicon (a) (100), (b) (110), (c) (111) planes, (d) Diamond cubic lattice of single crystal silicon with each atom covalently bonded to its four neighbours, (e) Wafers smaller than 200 mm in diameter have flat that indicates the $\langle 110 \rangle$ direction, whereas larger wafers have a notch [94].

Generally, the silicon wafers used for micromachining have a surface orientation (100), (111), and (110). The $\{111\}$ planes are the most densely packed and oriented 54.74° from $\{100\}$ planes. The magnitude of the piezoresistive effect is dependent on the crystal orientation of the resistor. Piezoresistors are oriented in the $\langle 100 \rangle$ and $\langle 110 \rangle$ directions for n-type and p-type doping respectively to take benefit of maximum sensitivity [94].

B.4 STRESS, STRAIN AND TENSORS FOR SILICON

The state of stresses for a unit element (nine stress components (σ_{ij})) is required to begin the discussion about the piezoresistivity as in Figure B.3. Stress components are defined by tensor as per equation (B.8) given below.

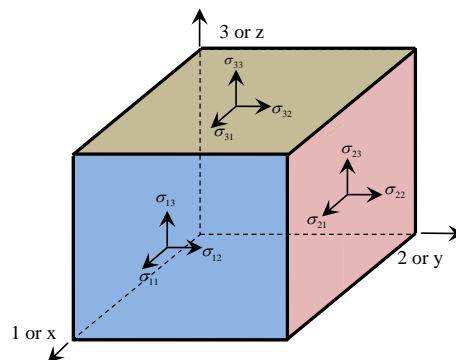


Figure B.3: The stress components σ_{ij} represents the stress on face i in direction j . When $i = j$ and $i \neq j$ represents normal and shear stress components respectively [94].

$$T_s = \begin{pmatrix} \sigma_{11} & \sigma_{12} & \sigma_{13} \\ \sigma_{21} & \sigma_{22} & \sigma_{23} \\ \sigma_{31} & \sigma_{32} & \sigma_{33} \end{pmatrix} \quad (\text{B.8})$$

Where $\sigma_{12} = \sigma_{21}$, $\sigma_{13} = \sigma_{31}$ and $\sigma_{23} = \sigma_{32}$ by symmetry. The number space i.e. 1, 2 and 3 are x,y and z directions in space respectively.

The stress tensor T_s is symmetric and has only six independent components. Therefore, the stress components are denoted by a simplified notation system as,

$$\sigma_{11} = \sigma_1, \sigma_{22} = \sigma_2, \sigma_{33} = \sigma_3, \sigma_{23} = \sigma_4, \sigma_{13} = \sigma_5, \sigma_{12} = \sigma_6$$

The indices used to define the stress components denote the direction of the vector normal to the surface at which stress is applied (first index, i), while second index is used to define direction of the force or stress (second index, j). If the indices are equal i.e. $i = j$, the stress components are normal to the specified surface, while indices are not equal i.e. $i \neq j$, it indicates a shear stress on face i . The stress tensor is always symmetric i.e. $\sigma_{ij} = \sigma_{ji}$ under the assumption of static equilibrium. Thus, the stress tensor contains only six independent components. Strain, ε_{ij} also follows the symmetric relation. For an isotropic, homogeneous material, stress is related to strain by Hooke's Law, $\sigma = \varepsilon E$. However, a tensor is required to describe the full mechanics of the anisotropic material such as for silicon. Generally, the effective values of Young's modulus and Poisson's ratio for a single direction is used for simple loading situations [94]. The relationship between stress and strain are correlated by the elastic stiffness matrix (C_{ijkl}), as $\sigma_{ij} = C_{ijkl}\varepsilon_{kl}$, whereas, by the compliance matrix S_{ijkl} , as $\varepsilon_{ij} = S_{ijkl}E\sigma_{kl}$. For simplicity, tensor components are often used as collapsed notation. The collapsed notation facilitates to reduce each pair of subscripts to one number i.e. $11 \rightarrow 1, 22 \rightarrow 2, 33 \rightarrow 3, 23 \rightarrow 4, 13 \rightarrow 5, 12 \rightarrow 6$. Examples are σ_{11} becomes σ_1 , ε_{12} becomes ε_6 , C_{1111} becomes C_{11} and S_{2323} becomes S_{44} [94]. Mathematically, stress and strain relationship is explained by means elastic stiffness matrix, C_{ijkl} (equation (B.9)).

$$\begin{pmatrix} \sigma_{11} \\ \sigma_{22} \\ \sigma_{33} \\ \sigma_{23} \\ \sigma_{13} \\ \sigma_{12} \end{pmatrix} = \begin{pmatrix} C_{11} & C_{12} & C_{13} & C_{14} & C_{15} & C_{16} \\ C_{21} & C_{22} & C_{23} & C_{24} & C_{25} & C_{26} \\ C_{31} & C_{32} & C_{33} & C_{34} & C_{35} & C_{36} \\ C_{41} & C_{42} & C_{43} & C_{44} & C_{45} & C_{46} \\ C_{51} & C_{52} & C_{53} & C_{54} & C_{55} & C_{56} \\ C_{61} & C_{62} & C_{63} & C_{64} & C_{65} & C_{66} \end{pmatrix} \begin{pmatrix} \varepsilon_{11} \\ \varepsilon_{22} \\ \varepsilon_{33} \\ 2\varepsilon_{23} \\ 2\varepsilon_{13} \\ 2\varepsilon_{12} \end{pmatrix} \quad (\text{B.9})$$

The calculation of resistance change is done based on piezoresistive coefficients using the induced stress in response to applied pressure. Hence, a detailed explanation of the piezoresistive coefficient is presented for silicon in the next section.

B.5 PIEZORESISTIVITY IN SINGLE CRYSTAL SILICON AND EFFECT OF CRYSTALLOGRAPHIC ORIENTATION ON THE PIEZORESISTIVE COEFFICIENT

Single crystalline silicon and germanium are foremost materials of choice as piezoresistors. Smith in 1954 has reported first measurement of high value of piezoresistive coefficients in silicon and germanium [7]. Smith applied Bridgman's tensor notation to define piezoresistive coefficients. The schematic of Smith's test setup for experimental calculation of piezoresistive coefficients is presented in Figure B.4.

Lightly doped p and n-type samples of Si and Ge were characterised by applying uniaxial stress (σ) with hanging weights on the sample bars of silicon. The longitudinal and piezoresistive coefficients were measured in both the $\langle 100 \rangle$ and $\langle 110 \rangle$ directions and hence piezoresistive coefficients as π_{11} , π_{12} and π_{44} were obtained. The piezoresistive coefficient (π) is a tensor quantity because it relates two second order tensors, i.e. stress and resistivity as explained as in equation (B.10).

$$\frac{\Delta\rho_{\omega}}{\rho} = \sum_{\lambda=1}^6 \pi_{\omega\lambda} \sigma_{\lambda} \text{ or } (\Delta) = (\pi)(\sigma) \quad (\text{B.10})$$

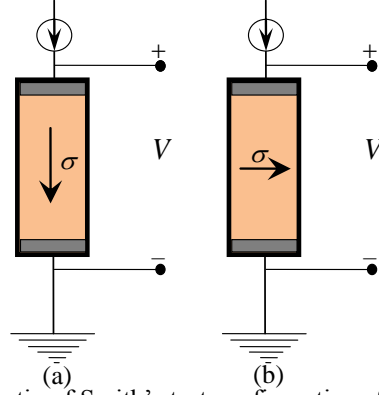


Figure B.4: Schematic of Smith's test configurations for calculating a) Longitudinal and b) Transverse piezoresistive coefficients.

To obtain the piezoresistive coefficients, the measured voltage drop in one direction, electrical current flow in another direction and stress applied in a third arbitrary direction are applied across the piezoresistor. The first subscript refers direction in which electrical potential is measured, current flow is represented by second subscript and the third and four subscripts stand for representing the stress because stress has two directional components. Therefore, piezoresistance coefficients are represented as $\pi_{1111} \rightarrow \pi_{11}$, $\pi_{1122} \rightarrow \pi_{12}$ and $\pi_{2323} \rightarrow \pi_{44}$, etc. explained as in equation (B.11). Later on Kanda, generalised these relations for a fixed voltage and current orientation (ω) as a function of stress direction (λ) [94].

$$\begin{pmatrix} \Delta_1 \\ \Delta_2 \\ \Delta_3 \\ \Delta_4 \\ \Delta_5 \\ \Delta_6 \end{pmatrix} = \begin{pmatrix} \pi_{12} & \pi_{12} & \pi_{13} & \pi_{14} & \pi_{15} & \pi_{61} \\ \pi_{21} & \pi_{22} & \pi_{23} & \pi_{24} & \pi_{25} & \pi_{62} \\ \pi_{31} & \pi_{32} & \pi_{33} & \pi_{34} & \pi_{35} & \pi_{63} \\ \pi_{41} & \pi_{42} & \pi_{43} & \pi_{44} & \pi_{45} & \pi_{64} \\ \pi_{51} & \pi_{52} & \pi_{53} & \pi_{54} & \pi_{55} & \pi_{65} \\ \pi_{61} & \pi_{62} & \pi_{63} & \pi_{64} & \pi_{65} & \pi_{66} \end{pmatrix} \begin{pmatrix} \sigma_1 \\ \sigma_2 \\ \sigma_3 \\ \sigma_4 \\ \sigma_5 \\ \sigma_6 \end{pmatrix} \quad (\text{B.11})$$

Where, Δ is known as a relative change in the resistivity, σ is stress consisting of three normal and three shear stress components.

The change in resistance/resistivity is because of applied stress in a semiconductor resistor.

The stress components in semiconductor resistor are expressed in the form of a 2nd rank

tensor with nine components (three normal and six shear components). These are simplified into six independent components using the symmetric condition. The resistivity of single crystalline material, i.e. silicon is expressed as a 2nd rank tensor with six independent tensors. Hence, 36 coefficients are required to establish relationship with stress and resistivity tensors referred as piezoresistive coefficient [94]. The piezoresistive coefficient tensor is further simplified for silicon by symmetric condition. Only three non-zero independent components remain in the simplified piezoresistive coefficient tensor for single crystalline silicon is written as in equation (B.12),

$$\pi = \begin{pmatrix} \pi_{11} & \pi_{12} & \pi_{12} & 0 & 0 & 0 \\ \pi_{12} & \pi_{11} & \pi_{12} & 0 & 0 & 0 \\ \pi_{12} & \pi_{12} & \pi_{11} & 0 & 0 & 0 \\ 0 & 0 & 0 & \pi_{44} & 0 & 0 \\ 0 & 0 & 0 & 0 & \pi_{44} & 0 \\ 0 & 0 & 0 & 0 & 0 & \pi_{44} \end{pmatrix} \quad (\text{B.12})$$

Smith in 1954 determined these coefficients for relatively lightly doped silicon samples with resistivity ranging from 1.5 to 22.7 $\Omega\text{-cm}$. The measured piezoresistive coefficients for (100) samples along the $\langle 100 \rangle$ and $\langle 110 \rangle$ crystal directions are reported in a reputed journal. Smith C.S. characterised piezoresistive coefficient of 7.8 $\Omega\text{-cm}$ p-type Si is $\pi_{11} = 6.6 \times 10^{-11}$, $\pi_{12} = -1.1 \times 10^{-11}$ and $\pi_{44} = 138.1 \times 10^{-11}$ 1/Pa [7].

It is assumed that the thickness of a piezoresistor is insignificant as compared to other two lateral geometrical dimensions. Therefore, stress components along the normal to the plane of piezoresistors are neglected. Hence, the simplified relationship for the relative change in the resistance is written as in equation (B.13) and (B.14),

$$\frac{\Delta R}{R} = \pi_l \sigma_l + \pi_t \sigma_t + \pi_s \tau_s \quad (\text{B.13})$$

The net effective relative resistivity change is usually written as a sum of the longitudinal and transverse effects as in equation (B.14),

$$\frac{\Delta R}{R} = \sigma_l \pi_l + \sigma_t \pi_t = \pi_l \sigma_x + \pi_t \sigma_y \quad (\text{B.14})$$

Where π_l , π_t and π_s are the longitudinal, transverse and shear piezoresistive coefficients respectively. σ_l , σ_t and τ_s are longitudinal, transverse and shear stress respectively. The relationship between π_l , π_t and fundamental piezoresistive coefficients depends on the crystallographic orientation of the resistor.

In the $\langle 100 \rangle$ direction, the relationships are given as in equation (B.15),

$$\pi_l = \pi_{11} \text{ and } \pi_t = \pi_{12} \quad (\text{B.15})$$

While in the $\langle 110 \rangle$ direction relationships are given as in equations (B.16) and (B.17)

$$\pi_l = \frac{1}{2}(\pi_{11} + \pi_{12} + \pi_{44}) \quad (\text{B.16})$$

$$\pi_t = \frac{1}{2}(\pi_{11} + \pi_{12} - \pi_{44}) \quad (\text{B.17})$$

Piezoresistive coefficients for lightly doped (10^{16} cm^{-3}) at room temperature single crystal silicon are given below in Table B.2. The piezoresistive coefficients π_{11} and π_{44} are dominant in n-type and p-type semiconductor respectively. The longitudinal and transverse piezoresistive coefficient in $\langle 100 \rangle$ and $\langle 110 \rangle$ directions are listed in Table B.3.

The p-type and n-type piezoresistors are oriented along the $\langle 110 \rangle$ and $\langle 100 \rangle$ directions with longitudinal tensile and compressive stresses respectively in order to achieve a higher resistivity change by the mobility enhancement. The magnitude of the piezoresistive coefficients decides the specific orientation of piezoresistors i.e. n-type and p-type resistors are oriented in $\langle 100 \rangle$ and $\langle 110 \rangle$ direction respectively for maximisation of the pressure response. It is observed that $\pi_l \approx -\pi_t$ for p-type resistors while $\pi_l \approx -2\pi_t$ for n-type piezoresistors. Longitudinal and transverse piezoresistive coefficients are calculated for arbitrary directions given in equation (B.18) and (B.19) [35],

Table B.2: Piezoresistive tensor components for lightly doped (10^{16} cm^{-3}) silicon in the (100) plane near room temperature [113].

Doping type	Piezoresistive Coefficients		
	$\pi_{11}(\text{Pa}^{-1})$	$\pi_{12}(\text{Pa}^{-1})$	$\pi_{44}(\text{Pa}^{-1})$
n-type	-102.2×10^{-11}	53.4×10^{-11}	-13.6×10^{-11}
p-type	6.6×10^{-11}	-1.1×10^{-11}	138.1×10^{-11}

Table B.3: Piezoresistive coefficients for (100) Si and doping less than 10^{18} cm^{-3} [113].

Silicon Type	Orientation of resistor	Piezoresistive coefficients	
		π_l (Longitudinal)	π_t (Transverse)
p-type	In <100>Direction	$6.6 \times 10^{-11}\text{Pa}^{-1}$	$-1.1 \times 10^{-11}\text{Pa}^{-1}$
p-type	In <110>Direction	$71.8 \times 10^{-11}\text{Pa}^{-1}$	$-66.3 \times 10^{-11}\text{Pa}^{-1}$
n-type	In <100>Direction	$-102.2 \times 10^{-11}\text{Pa}^{-1}$	$53.4 \times 10^{-11}\text{Pa}^{-1}$
n-type	In <110>Direction	$-31.6 \times 10^{-11}\text{Pa}^{-1}$	$-17.6 \times 10^{-11}\text{Pa}^{-1}$

$$\pi_l = \pi_{11} - 2(\pi_{11} - \pi_{12} - \pi_{44})(l_1^2 m_1^2 + m_1^2 n_1^2 + n_1^2 l_1^2) \quad (\text{B.18})$$

$$\pi_t = \frac{1}{2}(\pi_{11} + \pi_{12} - \pi_{44})(l_1^2 l_2^2 + m_1^2 m_2^2 + n_1^2 n_2^2) \quad (\text{B.19})$$

Where, l_i , m_i and n_i are direction cosines along the crystallographic coordinate system, direction of current flow and stress respectively. Generally, the (100) plane wafers are used in various sensors and actuators application, hence for (100) plane, direction cosines are given in equation (B.20),

$$\begin{pmatrix} l_1 & m_1 & n_1 \\ l_2 & m_2 & n_2 \\ l_3 & m_3 & n_3 \end{pmatrix} = \begin{pmatrix} \cos(\varnothing) & \sin(\varnothing) & 0 \\ -\sin(\varnothing) & \cos(\varnothing) & 0 \\ 0 & 0 & 1 \end{pmatrix} \quad (\text{B.20})$$

Where, \varnothing is the angle between current flow direction in piezoresistor and <100> direction. The best orientation that matches the most of the application is either in <100> or <110> direction to maximise the piezoresistive coefficient. If the placement of piezoresistors is in off-axis orientations, the generated stresses are calculated using the graphical representation as shown in Figure B.5.

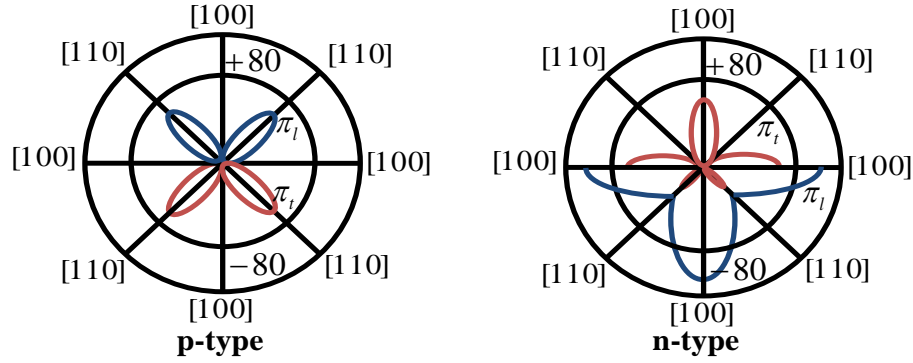


Figure B.5: Orientation dependency of the piezoresistive coefficient for p-type and n-type semiconductor resistors for lightly doped silicon in the (100) plane [94].

There are two common arrangements for measuring piezoresistive coefficients. These piezoresistive coefficients are dependent on doping and temperature. Hence, in the next section, the effect of temperature and doping concentration on piezoresistive coefficients is discussed.

B.6 TEMPERATURE AND CONCENTRATION DEPENDENCY FOR PIEZORESISTANCE FACTORS

Piezoresistivity in silicon as a function of operating temperature and dopant concentration is explained by Kanda's theoretical model [71]. As per Kanda's model, the piezoresistive coefficient at varying temperature and concentration is related by a piezoresistance factor with piezoresistive coefficients as given in equation (B.21),

$$\pi(N, T) = P(N, T)\pi^{ref} \quad (\text{B.21})$$

Where, π^{ref} is piezoresistive coefficient at 300 K for lightly doped material (10^{16}cm^{-3}) and $P(N, T)$ is a piezoresistance factor which is a function of doping and temperature.

Piezoresistive coefficients (π_{11} , π_{12} , π_{44} , π_l and π_t) can be scaled linearly using $P(N, T)$. The piezoresistance factor with doping and temperature is calculated as in eq.(B.22),

$$P = \frac{300 F'_{s+(1/2)}}{T F_{s+(1/2)}} \quad (\text{B.22})$$

Where F_s and F'_s are the Fermi integral and their derivatives with respect to the Fermi energy, E_F . Kanda considered that carriers are mainly scattered by phonons rather than ionised impurities. Hence, a scattering of impurity is important at high concentrations of order of $> 10^{19} \text{cm}^{-3}$. Phonons limited scattering corresponds to $s = -1/2$. In general, Fermi integral is given as in equation (B.23),

$$F_{s+(1/2)} = (k_b T)^{s+3/2} \int_0^\infty \frac{E^{s+(1/2)}}{1+\exp(\frac{E-E_F}{k_b T})} dE \quad (\text{B.23})$$

for density of states available for conduction, Fermi level is calculated.

$$n = v\sqrt{2} \left(\frac{m_d^* k_b T}{\pi h_c} \right)^{3/2} F_{s+(1/2)} \left(\frac{E_F}{k_b T} \right) \text{ and } \frac{E_F}{k_b T} = \frac{\ln(u)}{1-u^2} + \vartheta - \frac{v}{1+(0.24+1.08\vartheta)^2} \quad (\text{B.24})$$

$$u = \frac{\pi^2 N_d}{v\sqrt{2}} \left(\frac{m_d^* k_b T}{h_c} \right)^{-3/2} \text{ and } v = \left(\frac{3\sqrt{\pi}u}{4} \right)^{2/3} \quad (\text{B.25})$$

Where, k_b is Boltzmann constant, n is carrier concentration, h_c is Planck's constant, v is number of carrier valleys, and m_d^* is density of states effective mass. There are six valleys for both n-type and p-type silicon, while m_d^* is 1.08 or 0.49 for electrons (n-type) or holes (p-type) respectively. Analytical approximations for inverse Fermi integral is derived by Nilsson method, which is accurate to within 0.5 % for $-10 < \frac{E_F}{k_b T} < 20$ [114].

Piezoresistance depends on the doping concentration of material and operating temperature. The piezoresistance coefficient decreases appreciably with the increase of doping concentration and temperature. A systematic experimental study of piezoresistivity vs temperature and doping level was carried out by Tufte and Stelzer [115] in 1960's. The study was extended by Kanda [71]. Trends of piezoresistive factor with temperature and doping for p and n-Si are shown in Figure B.6 (a) and (b) respectively.

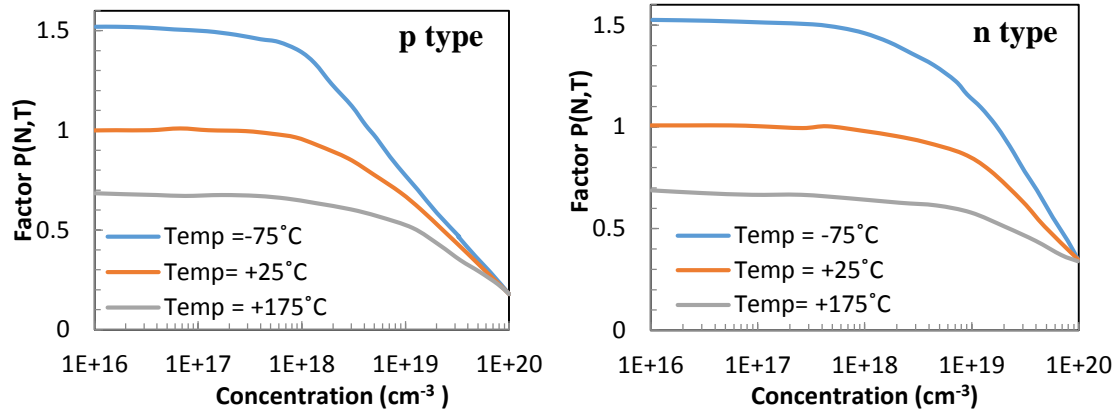


Figure B.6: Piezoresistance factor $P(N, T)$ as a function of impurity concentration and temperature for (a) p-type, and (b) n-type Si. The plots are based on the data presented by Kanda [71].

In Figure B.6, the data is reported by Kanda [71]. It is claimed that the disagreement between the theoretical results and the experimental results is within 15% for a temperature range of -50°C to $+175^\circ\text{C}$ and a doping level up to $5 \times 10^{18} \text{ cm}^{-3}$ [71].

Appendix C. ANALYSIS OF WHEATSTONE BRIDGE CONFIGURATIONS FOR PIEZORESISTIVE PRESSURE SENSORS

The schematic of placements of the piezoresistors on the diaphragms is shown in Figure C.1 (a) and (b). The resistors are placed in high stress concentration regions, in order to obtain higher sensitivity and connected in the form of a Wheatstone bridge as shown in Figure C.1 (c). All the four piezoresistors are placed on the thin diaphragm with elongation and compression arrangements. The two resistors of opposite arm exhibit the same change due to the induced stresses. The remaining two resistors in the other opposite arm exhibit the same but opposite change in their resistance, i.e. two piezoresistors show increase and other two show a decrease of resistance.

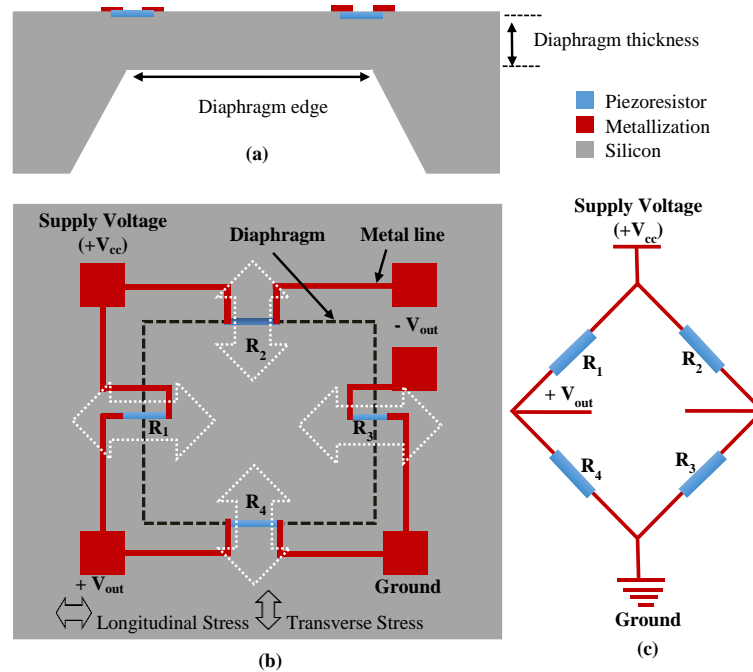


Figure C.1: Schematic representation of a piezoresistive pressure sensor; (a) Cross section view, (b) Top view of diaphragm, and (c) Wheatstone bridge configuration.

In addition to full bridge configuration, the Wheatstone bridge configurations of a quarter bridge or half bridge can also be used. In the quarter bridge configuration, Wheatstone

bridge utilises single sensing piezoresistive element and in half bridge configuration, uses two sensing piezoresistive elements. These configurations are discussed in next section.

C.1 QUARTER-BRIDGE

Single active element is used in a quarter bridge configuration. In Figure C.1 (c), R_2 is the piezoresistive sensing element and it changes by $\pm\Delta R$ by the induced stress on the resistor due to applied pressure. It is assumed that all four resistors have the same value without stress, i.e. $R_1=R_2=R_3=R_4=R$. The bridge is excited by $+V$, supply voltage and it results in an output voltage as in equation (C.1),

$$V_0 = \left[\frac{R_4}{R_1+R_4} - \frac{R_3}{R_3+R_2} \right] V \quad (C.1)$$

Assuming $R_1=R_2=R_3=R_4=R$ and sensing resistor is R_2 with a change $\pm\Delta R$ depending on the stress region, above equation is rewritten as in equations (C.2),

$$V_0 = \frac{1}{2} \left[1 - \left(1 \pm \frac{\Delta R}{2R} \right)^{-1} \right] V = \frac{1}{2} \left[\pm \frac{\Delta R}{2R} \right] V = \pm \frac{\Delta R}{4R} V \quad (C.2)$$

C.2 HALF-BRIDGE

Similarly half bridge is analysed as in equation (C.3),

$$V_0 = \left[\frac{R}{R+R+\Delta R} - \frac{R+\Delta R}{R+R+\Delta R} \right] V = \pm \frac{\Delta R}{2R} V \quad (C.3)$$

C.3 FULL-BRIDGE

In full bridge configuration, all the piezoresistors are used as sensing elements. Hence, the output response is higher than the other two types of configurations resulting in the higher sensitivity of the sensor (equation (C.4)).

$$V_0 = \left[\frac{R+\Delta R}{R+R} - \frac{R-\Delta R}{R+R} \right] V = \frac{\Delta R}{R} V \quad (C.4)$$

The comparison of sensitivity with various configurations is listed in Table C.1.

Table C.1: Comparison of the sensitivity for various configurations of Wheatstone bridge.

Type of configuration	Quarter-bridge	Half-bridge	Full-bridge
Sensitivity	S	$2S$	$4S$

C.4 CALCULATION OF THE OUTPUT VOLTAGE DUE TO APPLIED PRESSURE

All resistors are placed along the $\langle 110 \rangle$ direction at the middle of the edge of diaphragm.

These resistors experience longitudinal (R_1 and R_3) and transverse (R_2 and R_4) stress that results in the change in the resistance of the piezoresistors. Mathematically, changes

in resistance of piezoresistors are described in equations (C.5) and (C.6) [116].

$$\alpha_l = \frac{\Delta R_1}{R_0} = \frac{\Delta R_3}{R_0} = \pi_l \sigma_l + \pi_t \sigma_t \quad (C.5)$$

Where, π_l and π_t are longitudinal and transverse piezoresistive coefficients.

$$\pi_l = \frac{1}{2}(\pi_{11} + \pi_{12} + \pi_{44}) \text{ and } \pi_t = \frac{1}{2}(\pi_{11} + \pi_{12} - \pi_{44}) \quad (C.6)$$

Since, $\sigma_t = \vartheta \sigma_l$ then α_l is rewritten as in equation (C.7),

$$\alpha_l = \frac{\Delta R_{1 \text{ or } 3}}{R_0} = (\pi_l + \vartheta \pi_t) \sigma_l \text{ and } \alpha_t = \frac{\Delta R_{2 \text{ or } 4}}{R_0} = (\vartheta \pi_l + \pi_t) \sigma_l \quad (C.7)$$

C.4.1 Calculation of output voltage

The output voltage is calculated as per following relation as in eq.(C.8) ,

$$V_0 = \left[\frac{R_3}{R_2 + R_3} - \frac{R_4}{R_1 + R_4} \right] V = \left[\frac{R_1 R_3 - R_2 R_4}{(R_2 + R_3)(R_1 + R_4)} \right] V \quad (C.8)$$

Substituting value of α_1 and $-\alpha_2$ in equation (C.9) and neglecting higher order terms,

$$V_0 = \left[\frac{\alpha_l + \alpha_t}{2(1 + \alpha_l - \alpha_t)} \right] V \cong \frac{\alpha_l + \alpha_t}{2} V = \frac{(1 - \vartheta)\pi_l + (\vartheta - 1)\pi_t}{2} \sigma_l V \quad (C.9)$$

The piezoresistive coefficients are strongly dependent on π_{44} . Therefore, longitudinal and transverse piezoresistive coefficient rewritten as in equations (C.10) and (C.11),

$$\pi_l = \frac{1}{2}\pi_{44} \text{ and } \pi_t = -\frac{1}{2}\pi_{44} \quad (\text{C.10})$$

$$V_0 = \frac{[(1-\vartheta)-(\vartheta-1)]\pi_{44}}{4}\sigma_l V = (1-\vartheta)\frac{\pi_{44}}{2}\sigma_l V = \frac{\pi_{44}}{2}(\sigma_l - \sigma_t)V \quad (\text{C.11})$$

C.4.2 Calculation of sensitivity

The sensitivity of the piezoresistive pressure sensor is described by substituting the value of $\sigma_{max} = \sigma_l = \frac{0.308Pa^2}{h^2}$ in the equations (C.11) and rewritten as in equation (C.12).

$$\text{Sensitivity } (S_p) = \frac{V_0/V}{P} = 0.308(1-\vartheta)\frac{\pi_{44}}{2}\frac{a^2}{h^2} \quad (\text{C.12})$$

C.4.3 Calculation of nonlinearity

The non-linearity is calculated at maximum operating pressure and hence at the corresponding maximum output voltage. The nonlinearity is expressed as in eq. (C.13),

$$NL_i = \frac{V_0(P_i) - \frac{V_0(P_m)P_i}{P_m}}{V_0(P_m)} \times 100\% \quad (\text{C.13})$$

Where, $V_0(P_i)$ is voltage output at a pressure P_i , $V_0(P_m)$ is voltage output at pressure P_m and P_m is the maximum pressure range of pressure sensor.

REFERENCES

- [1] A. A. Barlian, W. T. Park, J. R. Mallon, A. J. Rastegar, and B. L. Pruitt, "Review: Semiconductor piezoresistance for microsystems," *Proc. IEEE*, vol. 97, no. 3, pp. 513–552, 2009.
- [2] J. W. Judy, "Microelectromechanical systems (MEMS): fabrication , design and applications," *Smart Mater. Struct.*, vol. 10, no. 6, pp. 1115–1134, 2001.
- [3] W. Eaton and J. Smith, "Characterization of a surface micromachined pressure sensor array," in *Proceedings of SPIE, Micromachining and Microfabrication Symposium*, 1995, vol. 2642, pp. 256–264.
- [4] E. Mounier, "Status of the MEMS industry 2015," *Technology and Market report, Villeurbanne*, 2015.
- [5] J. C. Eloy and E. Mounier, "Status of the MEMS industry: In MEMS/MOEMS Components and Their Applications II," *Eur. Semicond.*, vol. 5717, pp. 43–50, 2005.
- [6] M. J. Madou, *Fundamentals of microfabrication: the science of miniaturization*. CRC press, 2002.
- [7] C. S. Smith, "Piezoresistance effect in germanium and silicon," *Phys. Rev.*, vol. 94, no. 1, pp. 42–49, 1954.
- [8] A. Uhlir, "Electrolytic shaping of germanium and silicon," *Bell Syst. Tech. J.*, vol. 35, no. 2, pp. 333–347, 1956.
- [9] M. J. Madou, *Solid-State Physics, Fluidics, and Analytical Techniques in Micro-and Nanotechnology*, vol. 1. CRC Press, 2011.
- [10] K. E. Petersen, "Silicon as a mechanical material," *Proc. IEEE*, vol. 70, no. 5, pp. 420–457, 1982.
- [11] R. T. Howe and R. S. Muller, "Resonant-microbridge vapor sensor," *Electron Devices, IEEE Trans.*, vol. 33, no. 4, pp. 499–506, 1986.
- [12] R. P. Feynman, "There's plenty of room at the bottom," *Eng. Sci.*, vol. 23, no. 5, pp. 22–36, 1960.
- [13] R. P. Feynman, "There's plenty of room at the bottom [data storage]," *J. microelectromechanical Syst.*, vol. 1, no. 1, pp. 60–66, 1992.
- [14] G. T. A. Kovacs, N. I. Maluf, and K. E. Petersen, "Bulk micromachining of silicon," *Proc. IEEE*, vol. 86, no. 8, pp. 1536–1551, 1998.
- [15] H. Kahn, A. H. Heuer, and S. J. Jacobs, "Materials issues in MEMS," *Mater. Today*, vol. 2, no. 2, pp. 3–7, 1999.
- [16] H. A. Waggener, R. C. Kragness, and A. L. Tyler, "Anisotropic etching for forming isolation slots in silicon beam leaded integrated circuits," in *Electron Devices Meeting, 1967 International*, 1967, p. 68.
- [17] K. R. Williams, K. Gupta, and M. Wasilik, "Etch rates for micromachining processing - Part II," *J. Microelectromechanical Syst.*, vol. 12, no. 6, pp. 761–778, 2003.
- [18] R. M. Finne and D. L. Klein, "A water-amine-complexing agent system for etching silicon," *J. Electrochem. Soc.*, vol. 114, no. 9, p. 965, 1967.
- [19] M. Shikida, K. Tokoro, D. Uchikawa, and K. Sato, "Surface morphology of anisotropically etched single-crystal silicon," *J. Micromechanics Microengineering*, vol. 10, no. 4, pp. 522–

- 527, 2000.
- [20] H. C. Nathanson, W. E. Newell, R. A. Wickstrom, and J. R. Davis, "The resonant gate transistor," *IEEE Trans. Electron Devices*, vol. 14, no. 3, pp. 117–133, 1967.
- [21] J. M. Bustillo, R. T. Howe, and R. S. Muller, "Surface micromachining for microelectromechanical systems," *Proc. IEEE*, vol. 86, no. 8, pp. 1552–1574, 1998.
- [22] W. Ehrfeld *et al.*, "Fabrication of microstructures using the LIGA process," in *Proc. IEEE Micro Robots and Teleoperators Workshop*, 1987, vol. 160, p. 87–TH.
- [23] P. Bley *et al.*, "The LIGA Process for the fabrication of micromechanical and microoptical components," in *Proc. Micro System Technol. '91, 2nd Int. conf. Micro, Electro, Opto, Mechanic Systems and Components*, 1991.
- [24] P. Bley *et al.*, "Application of the LIGA process in fabrication of three-dimensional mechanical microstructures: micro/nanofabrication and devices," *JJAP Ser.*, vol. 5, pp. 384–389, 1992.
- [25] E. W. Backer *et al.*, "Production of separation-nozzle systems for uranium enrichment by a combination of X-ray lithography and galvanoplastics," *Naturwissenschaften*, vol. 69, no. 11, pp. 520–523, 1982.
- [26] H. Lorenz, M. Despont, N. Fahrni, N. LaBianca, P. Renaud, and P. Vettiger, "SU-8: a low-cost negative resist for MEMS," *J. Micromechanics Microengineering*, vol. 7, no. 3, p. 121, 1997.
- [27] Y. Xia and G. M. Whitesides, "Soft lithography," *Annu. Rev. Mater. Sci.*, vol. 28, no. 1, pp. 153–184, 1998.
- [28] G. Wallis, "Field assisted glass-metal sealing," *J. Appl. Phys.*, vol. 40, no. 10, pp. 3946–3949, 1969.
- [29] M. Shimbo, K. Furukawa, K. Fukuda, and K. Tanzawa, "Silicon-to-silicon direct bonding method," *J. Appl. Phys.*, vol. 60, no. 8, pp. 2987–2989, 1986.
- [30] P. W. Barth, "Silicon fusion bonding for fabrication of sensors, actuators and microstructures," *Sensors Actuators A Phys.*, vol. 23, no. 1–3, pp. 919–926, Apr. 1990.
- [31] M. B. Cohn and R. T. Howe, "Wafer-to-wafer transfer of microstructures using break-away tethers," 6,142,358, 07-Nov-2000.
- [32] D. Maas *et al.*, "Fabrication of microcomponents using adhesive bonding techniques," *Proc. Ninth Int. Work. Micro Electromechanical Syst.*, pp. 331–336, 1996.
- [33] T. R. Hsu, *MEMS & microsystems: design, manufacture, and nanoscale engineering*. John Wiley & Sons, 2008.
- [34] K. N. Bhat and M. M. Nayak, "MEMS pressure sensors- an overview of challenges in technology and packaging," *Inst. Smart Struct. Syst.*, vol. 2, no. 1, pp. 39–71, 2013.
- [35] M. Bao, *Analysis and design principles of MEMS devices*. Elsevier, 2005.
- [36] T. Dinh, H. P. Phan, A. Qamar, P. Woodfield, N. T. Nguyen, and D. V. Dao, "Thermoresistive effect for advanced thermal sensors: fundamentals, design considerations, and applications," *J. Microelectromechanical Syst.*, vol. 26, no. 5, pp. 966–986, 2017.
- [37] W. H. Ko, M. H. Bao, and Y. D. Hong, "A high-sensitivity integrated-circuit capacitive pressure transducer," *IEEE Trans. Electron Devices*, vol. 29, no. 1, pp. 48–56, 1982.
- [38] M.-X. Zhou, Q.-A. Huang, and M. Qin, "Modeling, design and fabrication of a triple-layered capacitive pressure sensor," *Sensors Actuators A Phys.*, vol. 117, no. 1, pp. 71–81,

- 2005.
- [39] Z. Tang, S. Fan, and C. Cai, "A silicon micromachined resonant pressure sensor," in *Journal of Physics: Conference Series*, 2009, vol. 188.
- [40] P. French, G. Krijnen, and F. Roozeboom, "Precision in harsh environments," *Microsystems Nanoeng.*, vol. 2, no. May, p. 16048, 2016.
- [41] S. Sundaram *et al.*, "Vibration and shock reliability of MEMS: modeling and experimental validation," *J. Micromechanics Microengineering*, vol. 21, no. 4, 2011.
- [42] J. R. Srour, C. J. Marshall, and P. W. Marshall, "Review of displacement damage effects in silicon devices," *IEEE Trans. Nucl. Sci.*, vol. 50, no. 3, pp. 653–670, 2003.
- [43] P. V. Ma, T.P. and Dressendorfer, T.-P. Ma, and P. V Dressendorfer, *Ionizing radiation effects in MOS devices and circuits*. John Wiley & Sons, 1989.
- [44] F. Faccio and G. Cervelli, "Radiation-induced edge effects in deep submicron CMOS transistors," *IEEE Trans. Nucl. Sci.*, vol. 52, no. 6, pp. 2413–2420, 2005.
- [45] H. R. Shea, "Radiation sensitivity of microelectromechanical system devices," *J. Micro/Nanolithography, MEMS, MOEMS*, vol. 8, no. 3, pp. 31303–31311, 2009.
- [46] C. N. Arutt *et al.*, "The study of radiation effects in emerging micro and nano electro mechanical systems (M and NEMs)," *Semicond. Sci. Technol.*, vol. 32, no. 1, 2017.
- [47] A. R. Knudson *et al.*, "The effects of radiation on MEMS accelerometers," *IEEE Trans. Nucl. Sci.*, vol. 43, no. 6, pp. 3122–3126, 1996.
- [48] C. I. Lee, A. H. Johnston, W. C. Tang, C. E. Barnes, and J. Lyke, "Total dose effects on microelectromechanical systems (MEMS): accelerometers," *IEEE Trans. Nucl. Sci.*, vol. 43, no. 6, pp. 3127–3132, 1996.
- [49] L. D. Edmonds, G. M. Swift, and C. I. Lee, "Radiation response of a MEMS accelerometer: an electrostatic force," *IEEE Trans. Nucl. Sci.*, vol. 45, no. 6, pp. 2779–2788, 1998.
- [50] E. B. Pitt *et al.*, "Radiation response and adaptive control-based degradation mitigation of MEMS accelerometers in ionizing dose environments," *IEEE Sens. J.*, vol. 17, no. 4, pp. 1132–1143, 2017.
- [51] T. F. Miyahira, H. N. Becker, S. S. McClure, L. D. Edmonds, A. H. Johnson, and Y. Hishinuma, "Total dose degradation of MEMS optical mirrors," *IEEE Trans. Nucl. Sci.*, vol. 50, no. 6 I, pp. 1860–1866, 2003.
- [52] S. S. McClure *et al.*, "Radiation effects in micro-electromechanical systems (MEMS): RF relays," *IEEE Trans. Nucl. Sci.*, vol. 49 I, no. 6, pp. 3197–3202, 2002.
- [53] L. Wang, J. Tang, and Q. A. Huang, "Gamma irradiation effects on surface-micromachined polysilicon resonators," *J. Microelectromechanical Syst.*, vol. 20, no. 5, pp. 1071–1073, 2011.
- [54] D. G. Marinaro, P. McMahon, and A. Wilson, "Proton radiation effects on MEMS silicon strain gauges," in *IEEE Transactions on Nuclear Science*, 2008, vol. 55, no. 3, pp. 1714–1718.
- [55] K. E. Holbert, J. A. Nessel, S. S. McCready, A. S. Heger, and T. H. Harlow, "Response of piezoresistive MEMS accelerometers and pressure transducers to high gamma dose," *IEEE Trans. Nucl. Sci.*, vol. 50, no. 6, pp. 1852–1859, 2003.
- [56] G. M. Wells, H. T. H. Chen, J. P. Wallace, R. L. Engelstad, and F. Cerrina, "Radiation damage-induced changes in silicon nitride membrane mechanical properties," *J. Vac. Sci. Technol. B Microelectron. Nanom. Struct. Process. Meas. Phenom.*, vol. 13, no. 6, pp.

- 3075–3077, 1995.
- [57] S. S. McCready, T. H. Harlow, A. S. Heger, and K. E. Holbert, “Piezoresistive micromechanical transducer operation in a pulsed neutron and gamma ray environment,” *IEEE Radiat. Eff. Data Work.*, vol. 2002–Janua, pp. 181–186, 2002.
- [58] I. Obieta, E. Castano, and F. J. Gracia, “High-temperature polysilicon pressure sensor,” *Sensors Actuators A Phys.*, vol. 46, no. 1, pp. 161–165, 1995.
- [59] X. Li, Q. Liu, S. Pang, K. Xu, H. Tang, and C. Sun, “High-temperature piezoresistive pressure sensor based on implantation of oxygen into silicon wafer,” *Sensors Actuators A Phys.*, vol. 179, pp. 277–282, 2012.
- [60] S. Guo, H. Eriksen, K. Childress, A. Fink, and M. Hoffman, “High temperature smart-cut SOI pressure sensor,” *Sensors Actuators A Phys.*, vol. 154, no. 2, pp. 255–260, 2009.
- [61] Z. Niu, Y. Zhao, and B. Tian, “Design optimization of high pressure and high temperature piezoresistive pressure sensor for high sensitivity,” *Rev. Sci. Instrum.*, vol. 85, no. 1, p. 015001 1-8, 2014.
- [62] M. A. Fraga, H. Furlan, R. S. Pessoa, L. A. Rasia, and C. F. R. Mateus, “Studies on SiC, DLC and TiO₂ thin films as piezoresistive sensor materials for high temperature application,” *Microsyst. Technol.*, vol. 18, no. 7–8, pp. 1027–1033, Jan. 2012.
- [63] M. A. Fraga, H. Furlan, R. S. Pessoa, and M. Massi, “Wide bandgap semiconductor thin films for piezoelectric and piezoresistive MEMS sensors applied at high temperatures: an overview,” *Microsyst. Technol.*, vol. 20, no. 1, pp. 9–21, 2013.
- [64] H.-P. P. Phan, D. V. Dao, K. Nakamura, S. Dimitrijevic, and N.-T. T. Nguyen, “The piezoresistive effect of SiC for MEMS sensors at high temperatures: a review,” *J. Microelectromechanical Syst.*, vol. 24, no. 6, pp. 1663–1677, 2015.
- [65] S. S. Kumar, A. K. Ojha, and B. D. Pant, “Experimental evaluation of sensitivity and non-linearity in polysilicon piezoresistive pressure sensors with different diaphragm sizes,” *Microsyst. Technol.*, vol. 22, no. 1, pp. 83–91, 2016.
- [66] S. S. Kumar and B. D. Pant, “Polysilicon thin film piezoresistive pressure microsensor: design, fabrication and characterization,” *Microsyst. Technol.*, vol. 21, no. 9, pp. 1949–1958, 2015.
- [67] K. Singh, R. Joyce, S. Varghese, and J. Akhtar, “Fabrication of electron beam physical vapor deposited polysilicon piezoresistive MEMS pressure sensor,” *Sensors Actuators A Phys.*, vol. 223, pp. 151–158, 2015.
- [68] H.-D. Ngo, B. Mukhopadhyay, O. Ehrmann, and K.-D. Lang, “Advanced Liquid-Free, Piezoresistive, SOI-Based Pressure Sensors for Measurements in Harsh Environments,” *Sensors*, vol. 15, no. 8, pp. 20305–20315, 2015.
- [69] S. P. Timoshenko and S. Woinowsky Krieger, *Theory of plates and shells*. McGraw-hill, 1959.
- [70] U. Aljancic, D. Resnik, D. Vrtacnik, M. Mozek, and S. Amon, “Temperature effects modeling in silicon piezoresistive pressure sensor,” in *Electrotechnical Conference, 2002. MELECON 2002. 11th Mediterranean*, 2002, pp. 36–40.
- [71] Y. Kanda, “A graphical representation of the piezoresistance coefficients in silicon,” *IEEE Trans. Electron Devices*, vol. 29, no. 1, pp. 64–70, 1982.
- [72] C. H. Cho, R. C. Jaeger, and J. C. Suhling, “Characterization of the temperature dependence of the piezoresistive coefficients of silicon from -150 °C to +125 °C,” *IEEE Sens. J.*, vol. 8, no. 8, pp. 1455–1468, 2008.

- [73] S. M. Sze and K. K. Ng, *Physics of semiconductor devices*. John Wiley & Sons, Inc, 2007.
- [74] R. Hull, *Properties of crystalline silicon*, no. 20. IET, 1999.
- [75] S. Guo, H. Eriksen, K. Childress, A. Fink, and M. Hoffman, “High temperature smart-cut SOI pressure sensor,” *Sensors Actuators, A Phys.*, vol. 154, pp. 255–260, 2009.
- [76] J. Akhtar, B. B. Dixit, B. D. Pant, and V. P. Deshwal, “Polysilicon piezoresistive pressure sensors based on MEMS technology,” *IETE J. Res.*, vol. 49, no. 6, pp. 365–377, Nov. 2003.
- [77] M. R. Werner and W. R. Fahrner, “Review on materials, microsensors, systems, and devices for high-temperature and harsh-environment applications,” *IEEE Trans. Ind. Electron.*, vol. 48, no. 2, pp. 249–257, 2001.
- [78] M. Werner, P. Gluche, M. Adamschik, E. Kohn, and H.-J. Fecht, “Review on diamond based piezoresistive sensors,” in *IEEE International Symposium on Industrial Electronics. Proceedings. ISIE '98 (Cat. No.98TH8357)*, 1998, vol. 1, pp. 147–152.
- [79] J. Dzuba *et al.*, “AlGaN/GaN diaphragm-based pressure sensor with direct high performance piezoelectric transduction mechanism,” *Appl. Phys. Lett.*, vol. 107, no. 12, p. 122102 1-4, 2015.
- [80] O. Kordina and S. E. Saddow, *Silicon carbide overview*, vol. 1. Boston, MA, USA: Artech House, Inc, 2004.
- [81] M. Mehregany and C. A. Zorman, “SiC MEMS: Opportunities and challenges for applications in harsh environments,” *Thin Solid Films*, vol. 355, pp. 518–524, 1999.
- [82] M. Mehregany, C. A. Zorman, N. Rajan, and C. H. Wu, “Silicon carbide MEMS for harsh environments,” *Proc. IEEE*, vol. 86, no. 8, pp. 1594–1609, 1998.
- [83] C. S. Roper, V. Radmilovic, R. T. Howe, and R. Maboudian, “Single-source chemical vapor deposition of SiC films in a large-scale low-pressure CVD growth, chemical, and mechanical characterization reactor,” *J. Electrochem. Soc.*, vol. 153, no. 8, pp. C562–C566, 2006.
- [84] J. Zhang, C. Carraro, R. T. Howe, and R. Maboudian, “Electrical, mechanical and metal contact properties of polycrystalline 3C-SiC films for MEMS in harsh environments,” *Surf. Coatings Technol.*, vol. 201, no. 22–23 SPEC. ISS., pp. 8893–8898, 2007.
- [85] P. M. Sarro, “Silicon carbide as a new MEMS technology,” *Sensors Actuators, A Phys.*, vol. 82, no. 1, pp. 210–218, 2000.
- [86] F. Xiao-An, T. Jacob, M. Mehran, and A. Z. Christian, “Doped polycrystalline 3C-SiC films with low stress for MEMS: part I. Deposition conditions and film properties,” *J. Micromechanics Microengineering*, vol. 24, no. 3, p. 35013, 2014.
- [87] P. Cong and D. J. Young, “Single crystal 6H-SiC MEMS fabrication based on smart-cut technique,” *J. Micromechanics Microengineering*, vol. 15, no. 12, pp. 2243–2248, 2005.
- [88] C. Wu, C. A. Zorman, M. Mehregany, and S. Member, “Fabrication and testing of bulk micromachined silicon carbide piezoresistive pressure sensors for high temperature applications,” vol. 6, no. 2, pp. 316–324, 2006.
- [89] A. Yamamoto, N. Nawachi, T. Tsutsumoto, and A. Terayama, “Pressure sensor using p-type polycrystalline diamond piezoresistors,” *Diam. Relat. Mater.*, vol. 14, no. 3–7, pp. 657–660, 2005.
- [90] A. Yamamoto and T. Tsutsumoto, “Piezoresistive effect of CVD polycrystalline diamond films,” *Diam. Relat. Mater.*, vol. 13, no. 4–8, pp. 863–866, 2004.
- [91] J. L. Davidson, D. R. Wur, W. P. Kang, D. L. Kinser, and D. V. Kerns, “Polycrystalline

- diamond pressure microsensor,” *Diam. Relat. Mater.*, vol. 5, no. 1, pp. 86–92, 1996.
- [92] A. Yamamoto, N. Norio, and T. Takahiro, “Evaluation of diamond gauge factor up to 500°C,” *Diam. Relat. Mater.*, vol. 16, no. 8, pp. 1670–1675, 2007.
- [93] J.-C. Pu, S.-F. Wang, and J. C. Sung, “High-temperature oxidation behaviors of CVD diamond films,” *Appl. Surf. Sci.*, vol. 256, no. 3, pp. 668–673, 2009.
- [94] J. C. Doll and B. L. Pruitt, *Piezoresistor design and applications*. Springer, 2013.
- [95] J. S. Shor, D. Goldstein, and A. D. Kurtz, “Characterization of n-type beta-SiC as a piezoresistor,” *IEEE Trans. Electron Devices*, vol. 40, no. 6, pp. 1093–1099, 1993.
- [96] J. S. Shor, L. Bemis, and A. D. Kurtz, “Characterization of monolithic n-type 6H-SiC piezoresistive sensing elements,” *IEEE Trans. Electron Devices*, vol. 41, no. 5, pp. 661–665, 1994.
- [97] R. Ziermann, J. von Berg, W. Reichert, E. Obermeier, M. Eickhoff, and G. Krotz, “A high temperature pressure sensor with β -SiC piezoresistors on SOI substrates,” in *Solid State Sensors and Actuators, 1997. TRANSDUCERS '97 Chicago., 1997 International Conference on, 1997*, vol. 2, pp. 1411–1414 vol.2.
- [98] Y. Tang, D. M. Aslam, J. Wang, and K. D. Wise, “Study of polycrystalline diamond piezoresistive position sensors for application in cochlear implant probe,” *Diam. Relat. Mater.*, vol. 15, no. 2–3, pp. 199–202, 2006.
- [99] P. Kulha *et al.*, “Nanocrystalline diamond piezoresistive sensor,” *Vacuum*, vol. 84, no. 1, pp. 53–56, 2009.
- [100] S. D. Janssens, S. Drijkoningen, and K. Haenen, “Ultra-thin nanocrystalline diamond membranes as pressure sensors for harsh environments,” *Appl. Phys. Lett.*, vol. 104, no. 7, p. 073107 1-4, 2014.
- [101] M. a. Hopcroft, W. D. Nix, and T. W. Kenny, “What is the Young’s modulus of silicon?,” *J. Microelectromechanical Syst.*, vol. 19, no. 2, pp. 229–238, Apr. 2010.
- [102] K. Sato, T. Yoshioka, T. Ando, M. Shikida, and T. Kawabata, “Tensile testing of silicon film having different crystallographic orientations carried out on a silicon chip,” *Sensors Actuators A Phys.*, vol. 70, no. 1–2, pp. 148–152, 1998.
- [103] V. Mosser, J. Suski, J. Goss, and E. Obermeier, “Piezoresistive pressure sensors based on polycrystalline silicon,” *Sensors Actuators A Phys.*, vol. 28, no. 2, pp. 113–132, 1991.
- [104] E. Obermeier and P. Kopystynski, “Polysilicon as a material for microsensor applications,” *Sensors Actuators A Phys.*, vol. 30, no. 1–2, pp. 149–155, 1992.
- [105] X. Liu, X. Lu, R. Chuai, C. Shi, M. Huo, and W. Chen, “Gauge factor and nonlinearity of p-type polysilicon nanofilms,” *Adv. Mater. Res.*, vol. 60, pp. 84–88, 2009.
- [106] H. P. Phan *et al.*, “Piezoresistive effect of p-type single crystalline 3C-SiC thin film,” *IEEE Electron Device Lett.*, vol. 35, no. 3, pp. 399–401, 2014.
- [107] V. A. Gridchin, V. M. Lubimsky, and M. P. Sarina, “Piezoresistive properties of polysilicon films,” *Sensors Actuators A Phys.*, vol. 49, no. 1–2, pp. 67–72, 1995.
- [108] W. N. Sharpe, B. Yuan, R. Vaidyanathan, and R. L. Edwards, “Measurements of Young’s modulus, Poisson’s ratio, and tensile strength of polysilicon,” in *Micro Electro Mechanical Systems, 1997. MEMS'97, Proceedings, IEEE., Tenth Annual International Workshop on, 1997*, pp. 424–429.
- [109] J. Suski, V. Mosser, and J. Goss, “Polysilicon SOI pressure sensor,” *Sensors and actuators*, vol. 17, no. 3–4, pp. 405–414, 1989.

-
- [110] Y. Chuan and L. Chen, "The compensation for hysteresis of silicon piezoresistive pressure sensor," *IEEE Sens. J.*, vol. 11, no. 9, pp. 2016–2021, 2011.
- [111] E. Ventsel, T. Krauthammer, and E. Carrera, *Thin plates and shells: theory, analysis, and applications*. New York: Marcel Dekker, 2002.
- [112] W. C. Young and R. G. Budynas, *Roark's formulas for stress and strain*, vol. 7. McGraw-Hill New York, 2002.
- [113] K. N. Bhat, "Silicon micromachined pressure sensors," *J. Indian Inst. Sci.*, vol. 87, no. 1, pp. 115–131, 2007.
- [114] N. G. Nilsson, "An accurate approximation of the generalized einstein relation for degenerate semiconductors," *Phys. status solidi*, vol. 19, no. 1, pp. K75–K78, 1973.
- [115] O. N. Tufte, P. W. Chapman, and D. Long, "Silicon diffused-element piezoresistive diaphragms," *J. Appl. Phys.*, vol. 33, pp. 3322–3327, 1962.
- [116] S. Chen, M. Zhu, B. Ma, and W. Yuan, "Design and optimization of a micro piezoresistive pressure sensor," pp. 351–356, 2008.

